DISSERTATION

SYNTHESIS AND CHARACTERIZATION OF IRON AND COPPER CHALCOGENIDE NANOMATERIALS FOR PHOTOVOLTAIC APPLICATIONS

Submitted by

Sarah J. Fredrick

Department of Chemistry

In partial fulfillment of the requirements

For the Degree of Doctor of Philosophy

Colorado State University

Fort Collins, Colorado

Fall 2014

Doctoral Committee:

Advisor: Amy Prieto

James Neilson
Anthony Rappé
Steven Strauss
John Williams

ABSTRACT

SYNTHESIS AND CHARACTERIZATION OF IRON AND COPPER CHALCOGENIDE NANOMATERIALS FOR PHOTOVOLTAIC APPLICATIONS

With our current looming energy and climate crises, it is vital that we find alternative forms of energy that have a lower carbon footprint. Solar technology is an excellent candidate for such purposes as the sun is an essentially unlimited source of renewable energy. However, the cost of solar cells is not economically competitive with fossil fuels. Alternatives to the traditional silicon solar modules could be a path toward reducing the cost of solar technology. The topic of this thesis is the synthesis and characterization of such alternatives. Iron and copper-based materials are earth abundant and potentially more cost-effective. Furthermore, processing these materials as nanocrystals, rather than bulk films, can reduce the energy input for fabricating solar absorber layers, and in turn, reduce overall system costs. Iron pyrite (FeS_2) and a related material, Fe_2GeS_4 are two materials with near ideal properties for solar absorption. While there has been a great deal interest in FeS_2, Fe_2GeS_4 is a novel system on which minimal research has been performed. Herein is described the synthesis and characterization of both of these iron chalcogenides with a particular focus on the challenging surface chemistry presented by these systems. Another system of increasingly widespread interest in recent years in the class of earth-abundant photovoltaic materials is Cu_2ZnSnS_4 (CZTS). A vast body of literature has been developed, but detailed characterization is lacking in much of the work, hindering our fundamental understanding of the properties. The final chapter of this thesis is a perspective work describing common characterization techniques for CZTS. It analyzes their usefulness in

determining the formation of the pure CZTS phase, in hopes of improving current understanding of the material.

TABLE OF CONTENTS

CHAPTER 1: INTRODUCTION TO THE USE OF EARTH-ABUNDANT NANOCRYSTALS FOR PHOTOVOLTAIC APPLICATIONS

Although there has been debate in recent years about the validity of man-made climate change (largely in political spheres), there is an immense amount of evidence supporting our role in changing the chemistry of the atmosphere. The dismal findings from a recent National Climate Assessment (NCA) report summarized the current state of carbon emissions, and came to the conclusion that the world is on a course to cause irreversible damage within a decade if drastic changes are not made.[1] Since the industrial revolution in the mid 1800's, carbon emissions have increased at alarming rates. This has resulted in unnatural increases in the atmospheric concentration of CO_2, and a concomitant increase in the global temperature (Figure 1.1).[3] Carbon dioxide is of major concern because of its contribution to the greenhouse gas effect, in which certain molecules in the atmosphere absorb solar radiation and reemit it as heat, causing an increase in the global temperature. While CO_2 is not the only greenhouse gas of concern – others include methane, nitrous oxide and fluorinated gases – it is representative of the overall problem. Scientists believe that this change in global temperature is responsible for a host of problems including pollution, extreme weather and changing climate trends, which can greatly affect human, plant and animal health due to their effects on air quality and water supplies, among others.[1] While small changes in behavior, like individuals and households using less electricity, can be helpful in reducing greenhouse gas emissions and conserving natural resources, large scale changes must be made in order to reverse this enormous problem.[1,4] One effective route to reduce our contributions to greenhouse gases is to produce energy with a lower carbon footprint. This means switching from power plants that use traditional fossil fuels and emit

large amounts of greenhouse gases to renewable sources of energy such as wind and solar power.

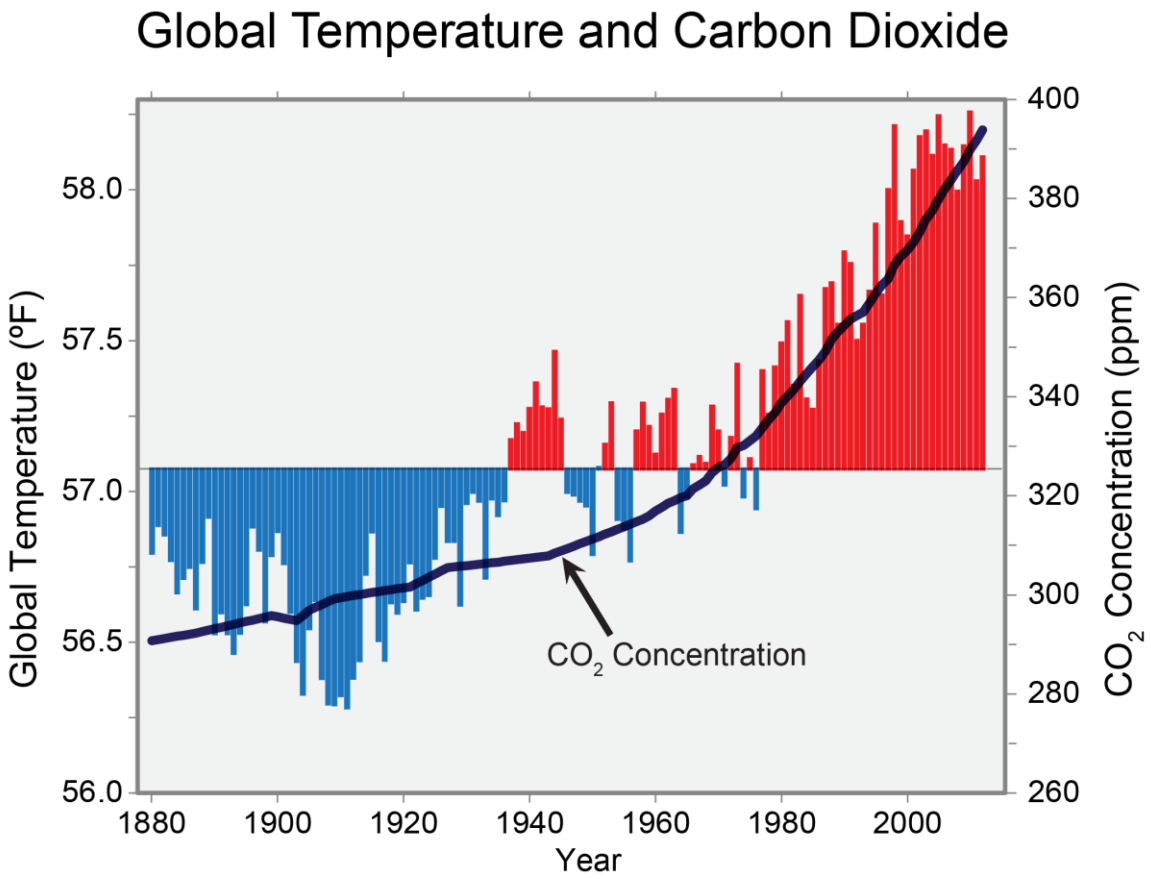

Figure 1.1: The average global temperature and CO_2 concentration are presented. The horizontal line in the middle of the graph is the long-term average temperature of the globe. Blue bars indicate average temperature readings in a year that is below the long term average and the red bars indicate average temperature readings above the long term average. The black line indicates the atmospheric CO_2 concentration. Figure obtained from nca2014.globalchange.gov, updated from Karl 2009.

Solar power is an essentially unlimited resource that has remained largely untapped. On average, 162,000 TW of energy from the sun irradiate the earth, while average worldwide human consumption is only 15 TW.[5] If only a fraction of the total energy from the sun can be harvested efficiently, all of our energy needs could be met. However, at this time, less than 0.5 % of total US power consumption is provided by solar photovoltaics.[6] The main reason

for this limited use of solar power cited by the US Department of Energy is the cost of solar PV as compared to other energy sources. The predicted levelized cost of electricity (LCOE) for power plants built in 2019 still estimates solar PV sources being 35 % more expensive than traditional coal sources.[7] With this cost differential, it is vital that research on solar technology is working to drive down the cost of solar technology, making it economically competitive with carbon-based fuels and ultimately more prevalent in our energy infrastructure.

The largest single cost in manufacturing and maintaining crystalline silicon solar panels (the current market standard) is the materials cost, comprising 55 % of total expenses.[8] Therefore, an effective route to reduce the cost of solar cells is to reduce the cost of the materials. Crystalline silicon is a good candidate for solar cells because it is highly abundant and affordable in the naturally occurring form of SiO_2. However, the drawbacks of silicon are its indirect band gap, requiring a thick layer of the material (~ 500 μm) in order to absorb sufficient solar radiation, and the large amount of energy required to convert SiO_2 to crystalline silicon.[9,10] For these reasons, finding alternative materials that are cheaper to process is an important step toward developing cost-competitive solar energy technology. These alternatives, ideally, should have the following criteria: i) a direct band gap and high absorption coefficient, ii) earth-abundant constituent elements, and iii) the raw materials with low extraction costs. Solar PV materials with direct band gaps, now called thin film or 2nd generation PV materials, have been widely researched as alternatives to silicon. These typically require the use of less than 1 μm of the absorber layer.[11] Some of the first materials used in this category were CdTe and $Cu(In,Ga)(S,Se)_2$ (CIGS). The photophysical properties of these materials are ideal for solar photoconversion, but rare, expensive elements like In, Ga and Te limit their large-scale potential.[12,13]

Much recent work on thin film PV has been focused on identifying and synthesizing materials that follow the aforementioned criteria. In 2009, Wadia and coworkers identified promising candidates based upon the annual electricity potential of the material and the extraction cost.[13] The best materials of the 23 analyzed in this report included CuO, Zn_3P_2 and the focus of much of this dissertation, FeS_2. Recent work by others have included slightly different criteria, but with similar goals, and have identified many new iron and copper-based materials, some of which have never been reported for use in solar technology.[14-16] These reports help guide synthetic chemists in choosing the right materials for solar applications. In the work presented in the following chapters of this thesis, three materials will be highlighted: FeS_2, Fe_2GeS_4 and Cu_2ZnSnS_4 (CZTS). All three materials have near ideal properties (i.e. band gap and absorption coefficient) for solar photoconversion and are comprised of earth-abundant elements, meeting the criteria put forth previously.

In addition to selecting the appropriate materials for solar cells, the overall costs can be reduced by avoiding high energy processing steps. In traditional solar cell processing, high temperatures (above 900 °C) and extreme (either high or low) pressures are required to make single crystals or thin films of the absorber layers.[9,17] Scaling of these methods is historically difficult and can limit solar cell production. One method used to make absorber materials at lower temperatures is to make them as colloidal nanocrystals.[18,19] This moves away from high temperature, vacuum-based processes and towards low-temperature (~300 °C) solution routes. It also allows for a greater variety of substrate choices and the potential for "roll-to-roll" printing of absorbers, greatly simplifying the production of solar cells and making them amenable to large-scale industrial processes.[19,20]

Colloidal nanocrystals can be synthesized by a variety of methods including coprecipitation, sol-gel, microwave and hydrothermal syntheses and extensive reviews have been written on the subject.[21-23] A commonly used method, and the focus of this dissertation, is coprecipitation by a surfactant-controlled growth process.[23] In this synthetic method, the precursors (metal salts and chalcogenide molecules) are dissolved in surfactant species that bind with the precursors to form reactive complexes referred to as "monomers." These monomer species serve as highly reactive precursor molecules, and when anion and cation monomers are introduced to a hot surfactant solution at appropriate temperatures, a burst of nucleation occurs and these nucleation sites grow (by further addition of monomer from solution) into the final nanocrystals.[23] The surfactant molecules serve many important purposes. They form the reactive monomer species necessary for product formation,[24,25] they can serve to control the redox chemistry of the solution, as reducing or oxidizing surfactants may be used, they aid in controlling the size and shape of nanocrystals by binding to the surface of the nanocrystals during nanocrystal growth,[26,27] and they stabilize the reactive surfaces of nanocrystals by binding to the surface and allowing for long-term colloidal stability.[28] This stability is imperative for solar cell processing, as it relies on the product being dispersed in a volatile solution, which can be evaporated from the substrate, leaving only the solid state semiconductor behind.

Even though the solution processing of nanocrystals has the potential to reduce the cost of solar modules dramatically, there are also drawbacks.[29,30] For optimal PV performance, the charge carriers must be able to move freely throughout the film to be efficiently collected at the back contact. In an ideal solar cell, the material would be composed of one single crystal with no grain boundaries, thus minimizing the potential for carrier recombination. In a nanocrystal film, the opposite of this ideal scenario is the case. Each nanocrystal creates a

grain boundary where it comes into contact with another nanocrystal. Furthermore, the native capping ligands inherent from the synthetic method are composed of insulating hydrocarbon chains, which makes electronic coupling between nanocrystals unlikely if these ligands are present. Various strategies of exchanging these ligands with small molecules to decrease the distance between nanocrystals and enhance electronic communication have been demonstrated to improve efficiencies in nanocrystalline PV devices,[31-36] most recently surpassing 8.5 %.[37] Even with these recent advances, they lag far behind their bulk thin film counterparts, for which the record efficiency is now up to 21 %. [38] There is a great deal of room for improvement in the efficiency of nanocrystalline thin films, specifically for newer alternative materials that have had a shorter history of research.

The topic of this thesis is the synthesis and characterization of such earth-abundant alternatives to silicon PV absorbers in nanocrystalline form. The following chapters will describe research performed on FeS_2, Fe_2GeS_4 and CZTS nanocrystals for their ultimate use in solar cell devices. Specific focus for the iron-based chalcogenide absorbers is on the surface chemistry and modification of the nanocrystal surfaces. The CZTS section discusses thorough characterization of this material to identify potential impurity phases. The ultimate goal for all of these materials is a fundamental understanding of their structure and properties, leading to improvements in overall solar cell efficiencies.

CHAPTER 2: THE SYNTHESIS AND CHARACTERIZATION OF IRON DISULFIDE NANOCRYSTALS

The experimental content and manuscript writing of this thesis chapter were completed by Sarah J. Fredrick. Garret Wheeler assisted with synthetic work. Scientific insight and editing help were provided by Amy L. Prieto and Daniel Agocs.

2.1 Introduction:

Iron pyrite, or FeS_2, has a band gap of 0.95-1.03 eV and an absorption coefficient of $>10^5$ cm^{-1}.[39,40] With these properties, power conversion efficiencies could reach 20 % with a film thickness of just 100 nm.[41,42] In 2009, just before the work described herein was started, Wadia, et al. examined 23 promising photovoltaic materials in terms of their extraction cost, availability and electricity potential.[13] For the selected criteria, iron pyrite outperformed all other materials due to its natural abundance and useful PV properties. Iron and sulfur are two of the most abundant elements in the earth's crust, and the most mined,[43] making the cost of this material disproportionately cheaper than other solar cell candidates. If solar energy is to be a long-term, sustainable solution for our energy needs, selecting a material with nearly unlimited supply, like pyrite, is a wise choice.

Interest in pyrite as a solar cell material is not a recent development in materials science. Initial studies began in the 1980's and 90's with pioneering work by Ennaoui and Tributsch.[44-47] However, most early synthetic approaches utilizing solid state synthetic methods or natural pyrite produced sulfur deficient samples, and even in samples with a very small fraction of the sulfur atoms missing, the performance was dramatically decreased. The highest power conversion efficiency demonstrated in early work was a mere 3 %,[40] significantly below the predicted 20 % efficiency, and this poor result has yet to be improved upon. Interest in this system waned in the mid 90's after no significant advances were made. In recent years, studies

on pyrite have surged as renewable energy technology, in particular solar technology, has received much research interest.[48-53]

In early work performed on the material, bulk FeS_2 was synthesized by various high-energy techniques such solid state diffusion,[44] thermal evaporation,[46] flash evaporation,[54] sulfurization of iron oxides[47] and chemical vapor deposition.[55] These methods proved ineffective for the synthesis of FeS_2 that was impurity-free with the correct stoichiometry. There are two stable phases of FeS_2; pyrite, which has a cubic structure and marcasite, which is orthorhombic. Marcasite has a significantly lower band gap of 0.34 eV, therefore any marcasite impurities dramatically reduce the electronic properties of FeS_2. However, an even more challenging synthetic issue is controlling the sulfur content. The Fe-S system has several stable sulfur deficient crystalline phases: Fe_7S_8, Fe_3S_4, and FeS. It is possible to obtain a mixture of stoichiometries or pure FeS_2 that is slightly sulfur deficient, both of which hinder the desired semiconductor transport properties.

Theoretical work has been performed to identify why a small sulfur deficiency affects the solar properties so greatly.[56] It was found that sulfur vacancies lead to S^{2-} states rather than the characteristic S_2^{2-} in pyrite. These manifest as trapped states located in the band gap and even a small percentage of these states dramatically reduces transport properties.[56,57] A great deal of surface studies have been performed on pyrite to determine the identity of these sulfur states on various cleavage planes. The monosulfide (S^{2-}) species, as compared to the disulfide or persulfide (S_2^{2-}), can be identified via XPS and is observed in nearly all pyrite samples.[56-61] The synthetic challenge in making high quality pyrite is in the ability to control the sulfur content and reduce these defects. This goal has not yet been achieved via traditional synthesis of bulk pyrite, but nanoscale materials may provide a solution to this longstanding problem.

A great advantage to the synthesis of nanomaterials can be the enhanced control over phase, composition and stoichiometry. Unlike high temperature processes, solution-based syntheses allow access to kinetic phases in addition to thermodynamic ones. More importantly for the pyrite system, a solution synthesis allows for careful tuning of the solution chemistry to promote sulfur incorporation. Finally, if the small percentage of sulfur defects exist on the surface, as has been previously suggested,[62] nanocrystal surfaces can readily be chemically modified (e.g. ligand substitution or the synthesis of core/shell structures) to "heal" these defects. With these potential advantages, a route to synthesizing high quality, nanoscale pyrite may lead to better PV devices for eventual use in solar cells.

At the onset of this research project in early 2010, work on synthesizing pyrite via low temperature methods or on the nanoscale was limited. Most reports focused on electrodeposition and hydrothermal methods.[52,63-66] As is common with aqueous electrodeposition methods, they required an additional annealing step in sulfur vapor to obtain the correct stoichiometry.[63,67] Others used hydrothermal methods to obtain nanocrystals or nanorods of pyrite.[52,64,66,68] These methods generally produced large nanocrystals (~100 nm in diameter) and did not demonstrate control over size or morphology. They were also not tested for any photovoltaic performance, perhaps suggesting that they were not, in fact, suitable for this application. The research project described in this chapter sought to make nanocrystals of pyrite in solution and modify those nanocrystals for optimal PV properties. During the course of the project, an article was published on a similar synthesis of pyrite nanocrystals (to be discussed in greater detail later) thus the current work was not submitted for publication, however, the following synthetic method was adopted for the research performed in the following chapter of this thesis.

2.2 Experimental:

All synthesis steps were performed in a nitrogen glove box or on a nitrogen/argon schlenk line. Many particle washing steps were performed in open air for rapid screening of stoichiometry and/or particle morphology. Pertinent studies were performed with a complete air free work up in the nitrogen glove box to avoid oxidation prior to analysis. All solvents used (hexane, toluene, chloroform, ethanol, methanol, isopropyl alcohol) were ACS grade from Aldrich and used as-received for bench top analysis. If used in the glove box, they were first degassed by the freeze pump thaw method. The following were purchased from Aldrich and used as-received: $FeCl_2$ (98 %), $Fe(OAc)_2$ (95 %), sulfur powder (reagent grade, purified by sublimation), trioctylphosphine oxide (99 %), trioctylphosphine (97 %), and tributylphosphine (97 %). Octadecene (90 %) and dodecanethiol (98 %) were purchased from Aldrich and degassed by bubbling argon through the solution for several hours prior to use. Oleylamine (80-90 %) was purchased from Acros and degassed with Ar before use. 1,2 hexadecanediol (98%) was used as purchased from TCI.

X-ray diffraction data were obtained on a Scintag X-2 Advanced Diffraction system equipped with Cu Kα radiation (λ=1.54Å). Sample holders were either low or zero background Si slides purchased from MTI Corporation. TEM analysis was performed on a JEOL JEM 2000 at a working voltage of 160kV or on a JEOL 1400 at a working voltage of either 100kV or 120kV. Digital images were taken on an Ultrascan 895 camera. X-ray photoelectron spectroscopy (XPS) (Phi 6500) measurements were performed with a 5800 series Multi-Technique ESCA system and analyzed using Multipak and/or XPSPeak 9.0 software. All peaks were shifted to carbon at 284.8 eV.

2.3 Results/Discussion:

Initial work exploring the synthesis of colloidal pyrite nanocrystals involved the use of a variety of precursors and surfactants. The optimal synthesis, to be discussed in the rest of this chapter, utilizes $FeCl_2$, sulfur powder and oleylamine in a hot injection synthesis. In the process of optimizing reaction conditions, many parameters were manipulated that did not give ideal results. It has been demonstrated in other nanocrystalline systems that the identity of the transition metal precursor can affect reaction products.[69,70] Two iron precursors with differences in reactivity, $FeCl_2$ and $Fe(OAc)_2$, were tested in a variety of synthetic conditions. The results demonstrated that $Fe(OAc)_2$ was uncontrollably reactive as compared to $FeCl_2$. A wide range of sulfur deficient phases were produced with only small temperature changes when $Fe(OAc)_2$ was used, so it was abandoned as a precursor option. The identity of the chalcogenide precursor was also an important variable to consider. Precursor reactivity in chalcogenide systems is an area of extensive study, as the identity of the surfactant can change the reactivity dramatically.[71,72] Other sulfur precursors were tested (e.g. TOP-S and TBP-S versus OLA-S) and these precursors were so unreactive that no iron sulfides were produced at temperatures below 350 °C (the practical upper limit of these solvent systems). Dodecanethiol (DDT) was also tested as a sulfur precursor, but only produced sulfur deficient phases. Finally, the solvent/surfactant choice can greatly affect the nanocrystal size, shape and composition, so this variable was carefully screened to make optimal nanocrystals. Solvent systems involving amines, phosphines and non-coordinating solvents such as octadecene were mixed in varying ratios, but syntheses involving all oleylamine as the capping ligand and solvent produced the best results. The addition of octadecene to reduce the monomer concentration in solution produced pyrite under certain reaction conditions. However, this typically only slowed the nanocrystal growth process and did not improve

nanocrystal morphology. Varying the injection temperature of the reaction gave amorphous phases if lower than the injection temperature for pyrite and higher temperatures produced sulfur deficient phases. The following two synthetic methods produced phase pure pyrite nanocrystals with desirable morphologies.

In brief, 0.5 mmol of $FeCl_2$ was dissolved in either 10 mmol of TOPO at 140 °C or 1.5 mL of OLA at 110 °C and 1.5 mmol of sulfur powder was dissolved in 1.5 mL of OLA at room temperature. Then 2 mL of OLA was heated to the desired injection temperature and the $FeCl_2$ and sulfur powder were simultaneously injected into the hot oleylamine. The reaction flask immediately turned black, indicating the formation of an iron sulfide product. Each reaction was left at the injection temperature for up to 300 minutes to monitor changes in particle size and

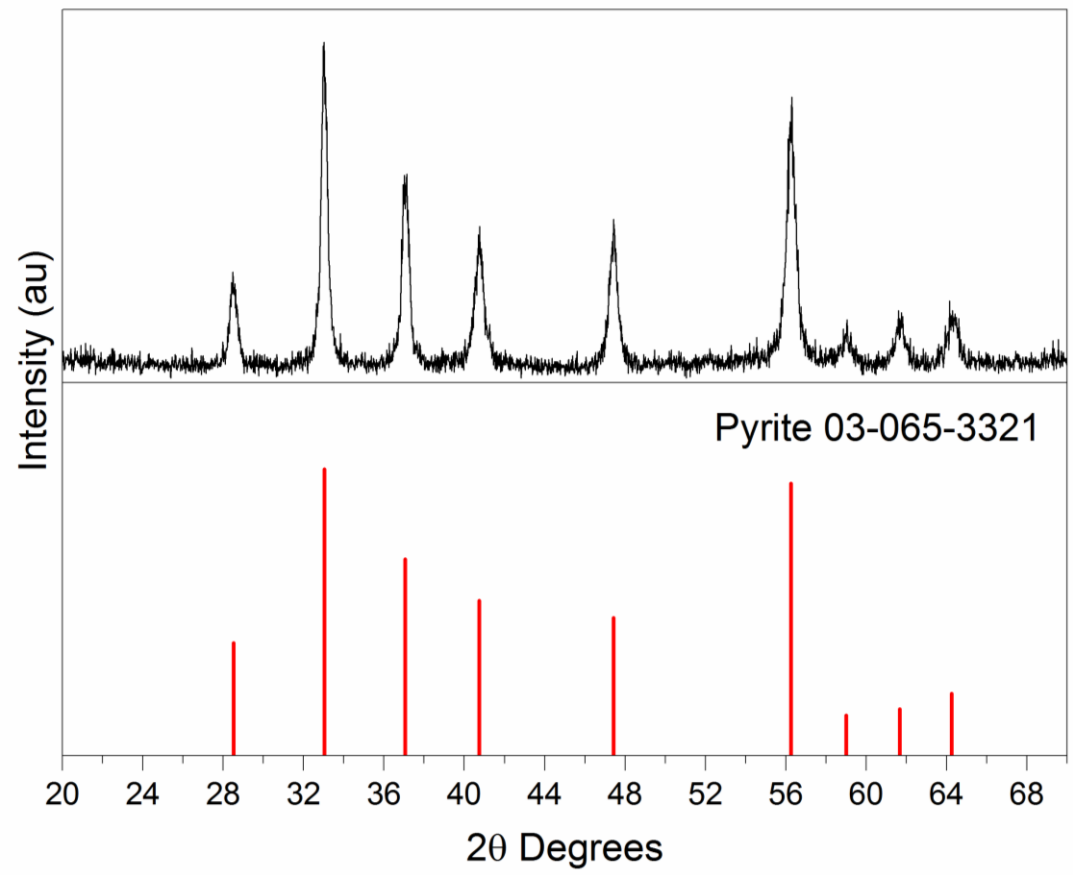

Figure 2.1: Representative x-ray powder diffraction pattern indicating the presence of pyrite with no other crystalline phases.

morphology.

Each reaction produced nanocrystalline pyrite at growth times as short as one minute as evidenced by X-ray powder diffraction and the crystallinity did not change observably over time (i.e. no new crystalline phases were formed and the peak broadening, indicative of crystallite size, did not change over time). Figure 2.1 shows a representative powder pattern obtained for TOPO and oleylamine syntheses. UV-Vis absorption (Figure 2.2) confirms that the nanocrystals absorb in the visible region as expected, but the onset of absorption is very gradual. In materials with clear and abrupt onsets of absorption, a Tauc plot can be used to estimate the band gap,[73] but this method proves unreliable in systems such as pyrite. Although many different growth times produce small (less than 100 nm), individual nanocrystals, none of the aliquots produce a stable colloidal suspension. All nanocrystals agglomerate and precipitate out of solution very rapidly. In addition to this being a problem

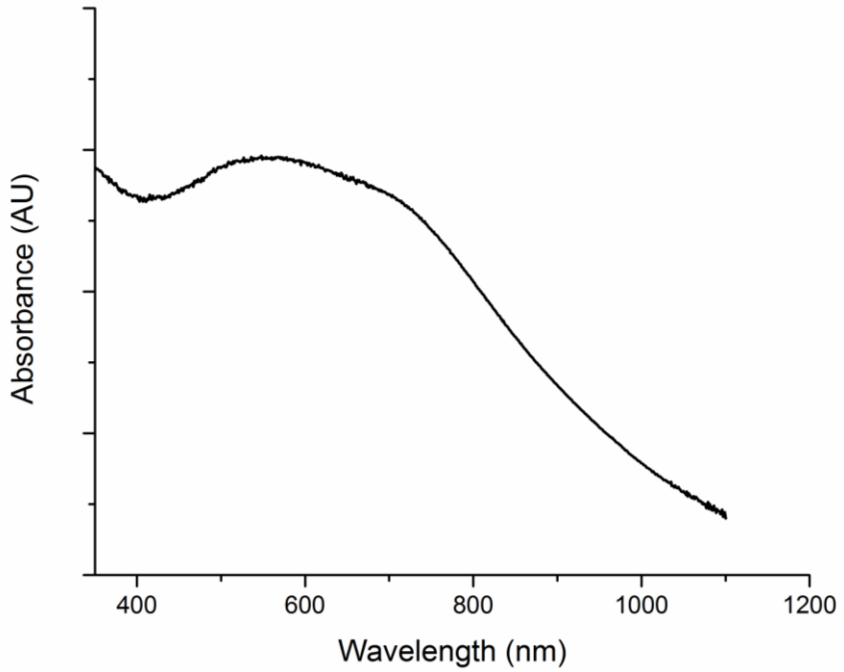

Figure 2.2: UV-vis absorption spectrum of pyrite nanocrystals in solution.

for rapid processing of nanocrystal inks into thin films, it is more importantly indicative of surface chemistry issues. It is likely a sign of poorly capped and highly reactive nanocrystal surfaces. This will be addressed in much greater detail in the following chapter.

The effect of growth time on nanocrystal morphology was monitored via transmission electron microscopy. It was found that in both reactions, individual nanocrystals were formed if the growth time was sufficiently long. However, in the case of using only oleylamine as a

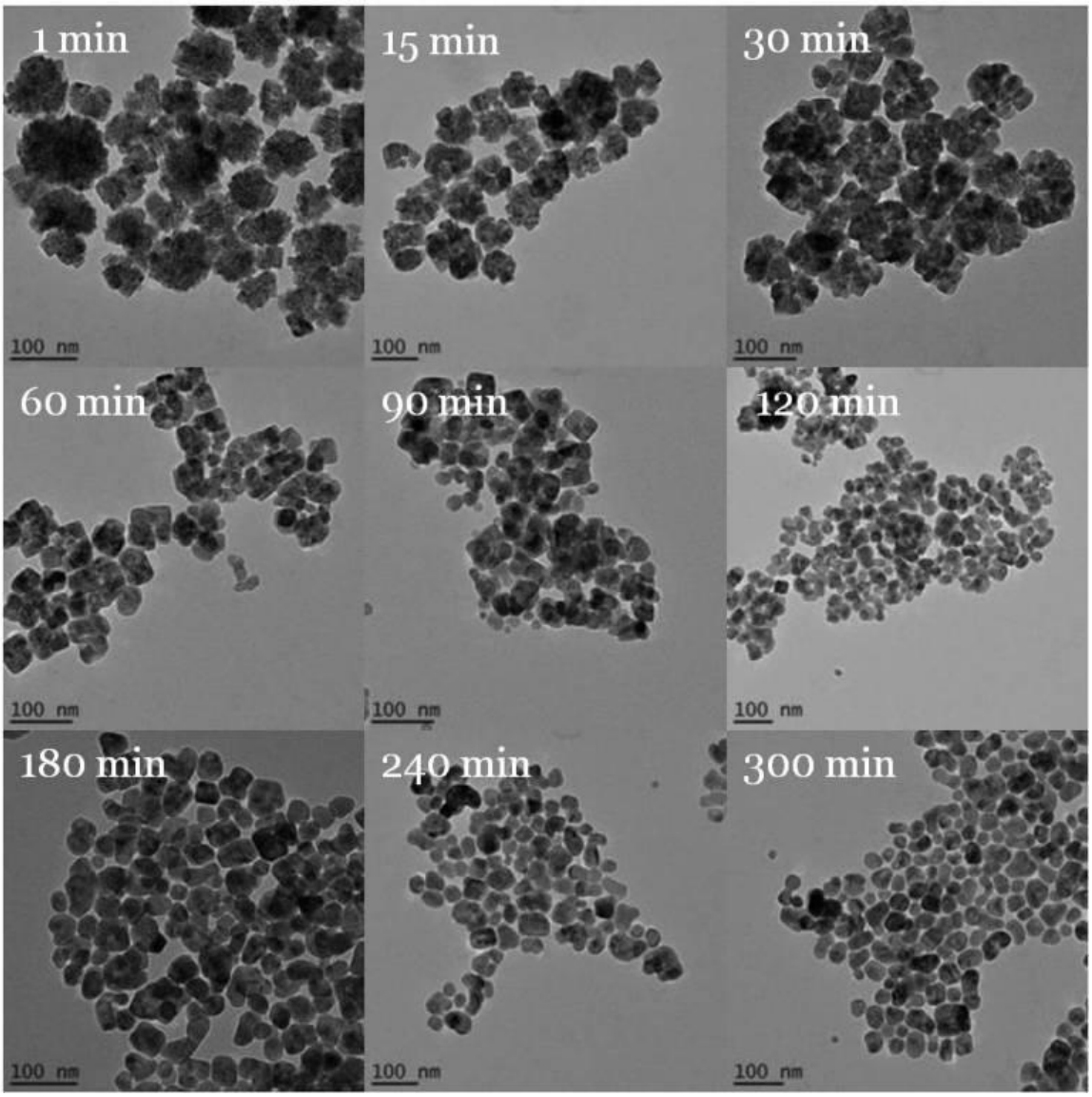

Figure 2.3: TEM images of particles formed at varied growth times for a reaction with oleylamine as the solvent.

solvent, individual particles form quite rapidly (within 15 minutes). Figure 2.3 shows TEM images of growth times from 1 minute to 300 minutes. Initially, the nanocrystals appear to be large agglomerates made up of small crystals, with seemingly straight edges. But within 15 minutes, these agglomerates appear to be individually defined nanocrystals significantly smaller than the original agglomerates. Over time, the particles grow larger and more monodisperse. In the reaction conditions in which TOPO was used as a surfactant, the nanocrystals were agglomerated for at least 90 minutes, versus the 15 minutes for the all OLA reaction, as can be seen in Figure 2.4. Additionally, the shapes of the nanocrystals, even at longer times, are more varied than in the all oleylamine case. Due to the fact that harsh surfactants, such as amines and phosphines, are known to etch nanocrystal surfaces over time, the shorter nanocrystal growth times are desired. In Figure 4, it does appear as though the nanocrystals can become etched over time. Rather than smoothed surfaces, as seen in Figure 3, these particles appear to be more irregular and even look pitted in spots. For these reasons, the reaction utilizing all oleylamine as the surfactant was chosen to be the best candidate for further analysis.

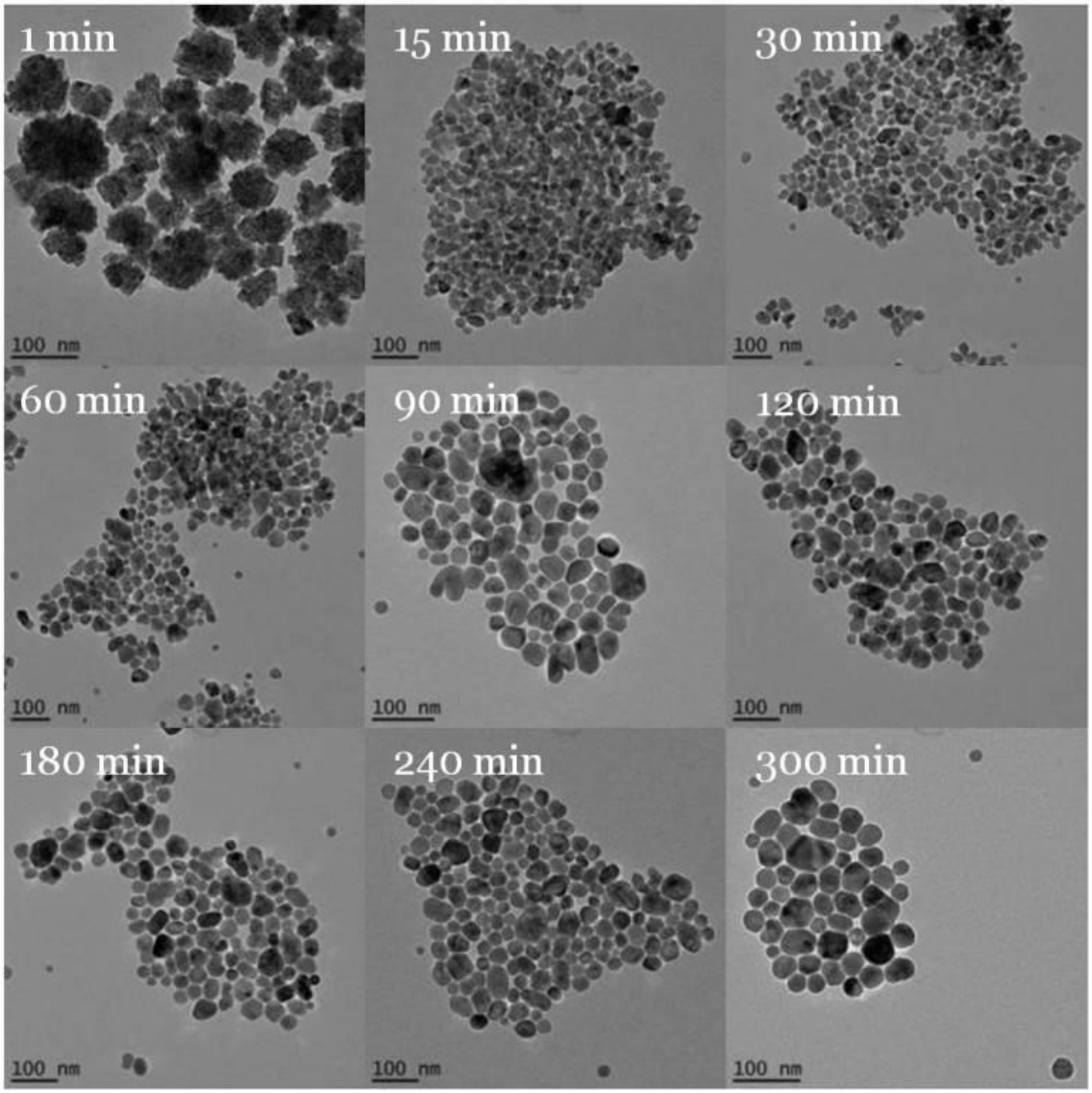

Figure 2.4: TEM images of particles formed at varied growth times for a reaction utilizing both TOPO and OLA.

The current and ongoing studies of this project focus not on continuing to manipulate the synthesis conditions, but rather seek to explore the properties of the synthesized materials. A large number of publications have been reported on the synthesis of pyrite nanocrystals in recent years. These have reported control over morphology and size,[74-78] and even detailed

unique nucleation and growth mechanisms for the solution phase synthesis of pyrite nanocrystals.[79] However, to our knowledge none of these reports have analyzed the transport properties in the nanocrystal films, nor have they analyzed the surface chemistry. In fact, the most complete report on the photophysical properties of pyrite demonstrated that none of the fabricated solar cell devices produced any photovoltage. The devices showed metallic behavior, rendering them useless for photovoltaics.[80] While synthetic developments can be

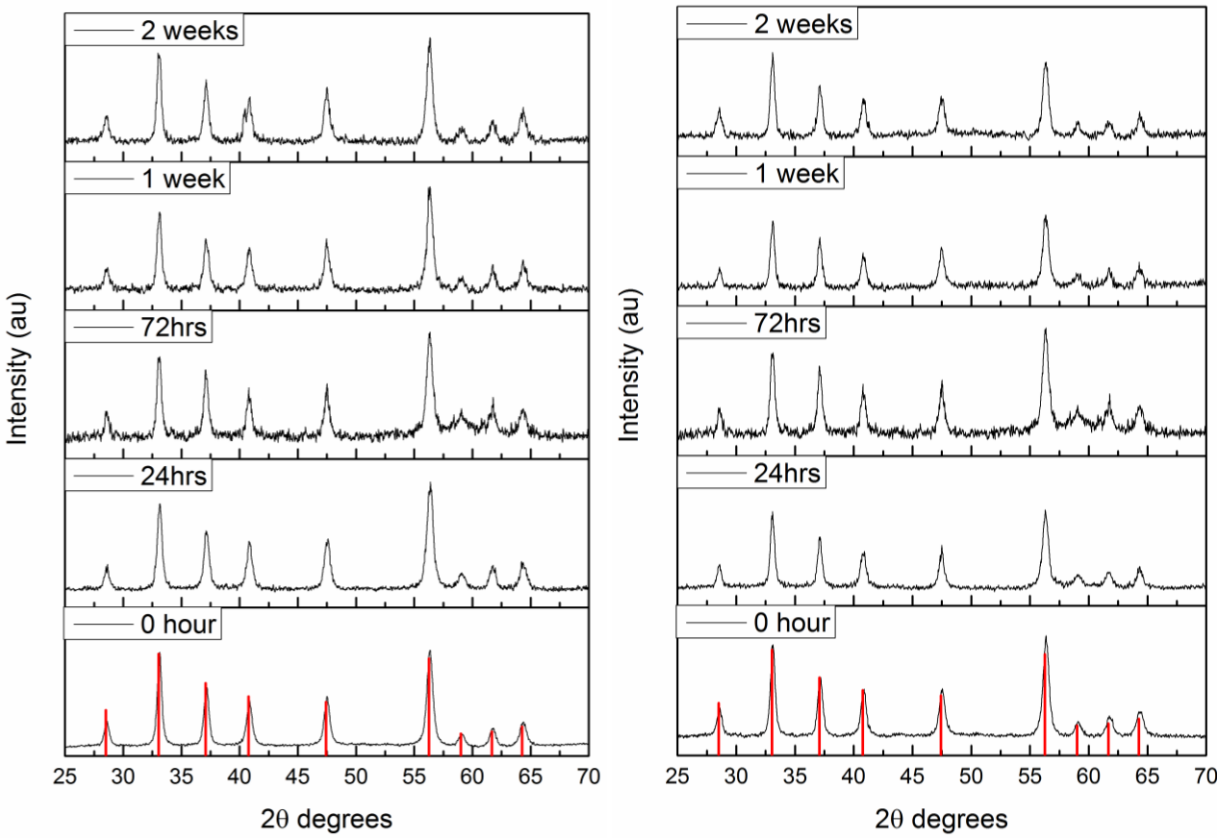

Figure 2.5: X-Ray diffraction patterns for a ten minute growth time (left) and four hour growth time (right). Each scan label indicates the amount of time the sample has been exposed to air.

useful in working toward improved device performance, it is imperative that we begin to understand issues that have historically created problems with the material. Some key problems such as surface chemistry and sulfur content have been minimally explored in pyrite nanocrystals, and very little has been done to relate these problems to photovoltaic performance.

The study reported herein seeks to explore differences in surface oxidation between particles from a long and short growth time. The study was done using both XRD and XPS. XRD can be used to determine if there are crystalline impurities that appear over time, however it does not give useful information if amorphous oxides form on the surface of pyrite. XPS gives detailed information about the binding environment of the elements in the nanocrystals, including oxidation state. It can also distinguish, for example, between an iron sulfide and an iron oxide binding environment. It is not contingent on the oxide layers being crystalline, so oxidation can be effectively monitored using this technique. Particles were synthesized with the parameters described for the reaction utilizing only oleylamine as the surfactant. Reaction growth times were either ten minutes or four hours. All work-up prior to characterization was performed without exposure to air. The dried precipitate from each reaction was used for XPS and XRD. Figure 2.5 shows XRD scans for the ten minute and four hour growth times starting at 0 hours (no exposure to air) up to two weeks. In the four hour growth time, no crystalline impurities are seen. However, in the ten minute growth time, a new peak at 40.7° is beginning to appear. The identity of this peak is not known, and identifying a phase based solely on one peak is difficult. These data suggest that the particles from the shorter growth time may undergo crystalline phase changes with long oxygen exposure times.

XPS was performed in conjunction with XRD to corroborate the apparent oxidation observed in the ten minute growth time particles. Literature reports on the surface chemistry of pyrite, including oxidation, are prevalent.[57,60,61,81,82] To our knowledge, there are currently no

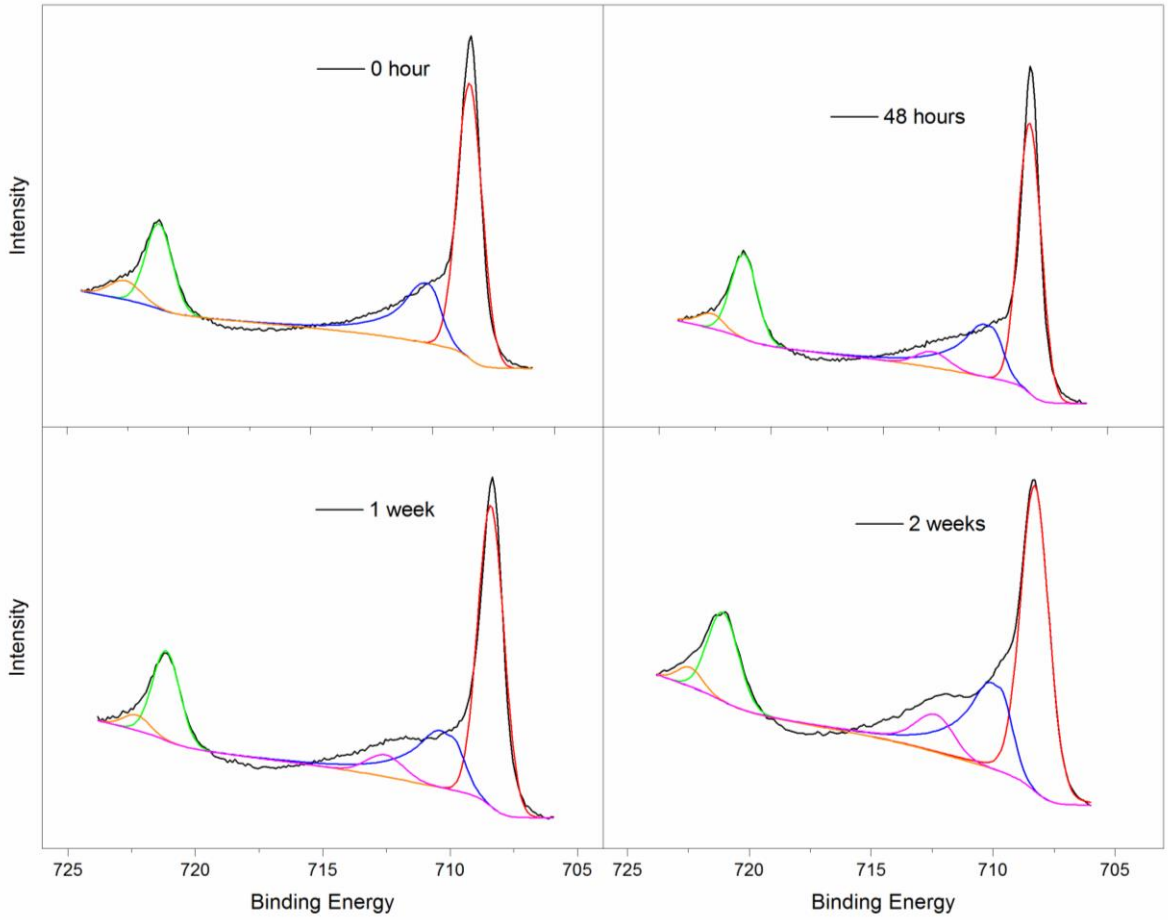

Figure 2.6: XPS spectra for the iron binding energies for the ten minute growth time for pyrite nanocrystals that have been exposed to air for different amounts of time. Characteristic Fe(II) sulfide peaks are in red (708.5 eV) and green (721.3 eV), while the blue trace is likely due to surface states. The magenta trace is a new iron state due to oxidation over time.

reports of high resolution XPS analysis of pyrite nanocrystals, past literature on bulk pyrite can inform the current work. The spectra were recorded initially with oxygen exposure only for transfer to the instrument (several seconds). The samples were then left in air for periods of 48 hours, one week and two weeks and XPS data was recorded at each of these times. Figures 2.6

and 2.7 show the iron XPS spectra for the ten minute (2.6) and four hour (2.7) growth times. Initially, both the ten minute and four hour samples look nearly identical via XPS and do not show any signs of oxidation. The red and green traces (708.5 and 721.3 eV

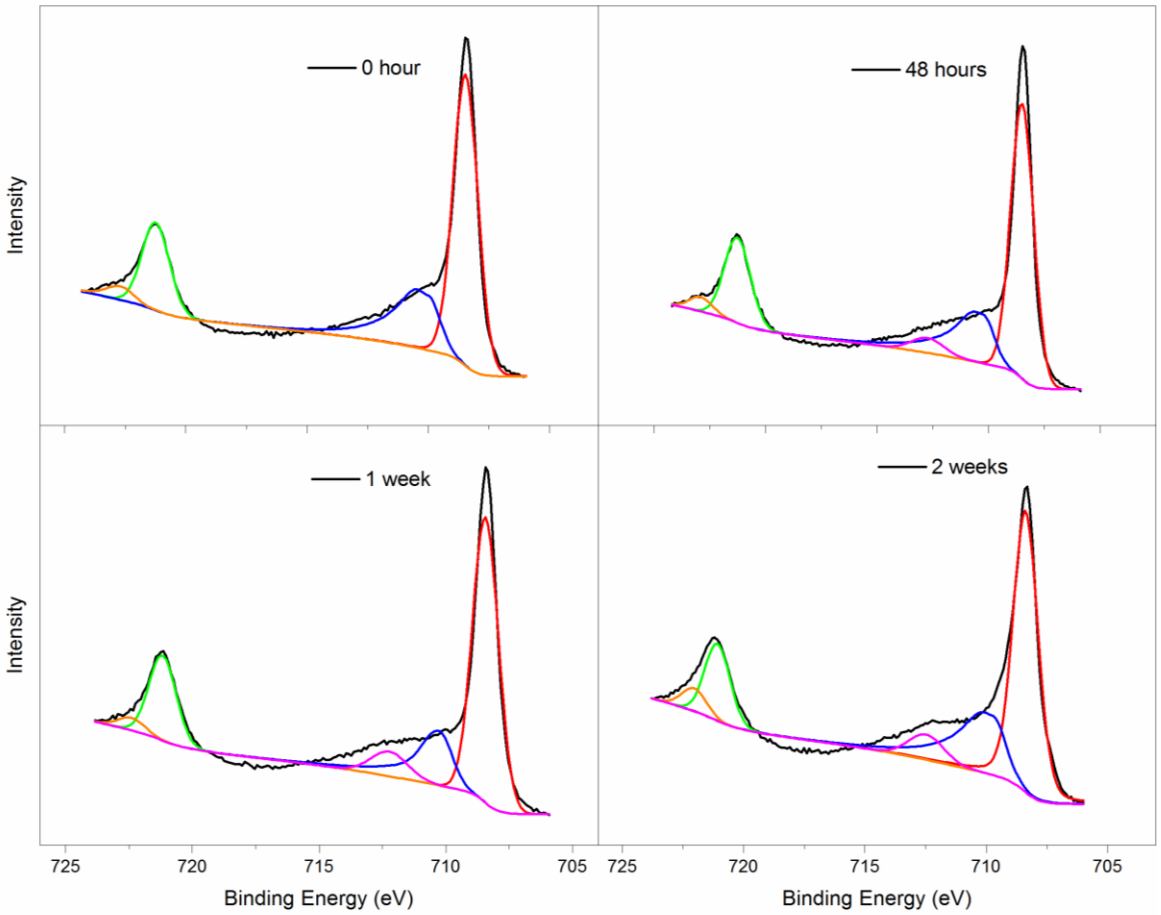

Figure 2.7: XPS spectra for the iron binding energies for the four hour growth time for pyrite nanocrystals that have been exposed to air for different amounts of time. Characteristic Fe(II) sulfide peaks are in red (708.5 eV) and green (721.3 eV), while the blue trace is likely due to surface states. The magenta trace is a new iron state due to oxidation over time.

respectively) are characteristic of Fe(II) states in pyrite.[81,82] The blue trace is also observed frequently and is attributed to iron multiplet states, surface states (such as $Fe\text{-}S^{2-}$ instead of $Fe\text{-}S_2^{2-}$ on the surface), or adsorbed oxygen.[60,83,84] Interestingly, this peak, which is likely due to surface states, is of roughly the same magnitude in both samples. With the apparent change

in crystal size and shape, it is presumed that the number of surface states compared to Fe(II) would decrease as the particle size is increased, but this change is not observed via XPS. Over time, in both samples, a new peak at approximately 712 eV emerges. This is likely an iron(III) oxide state, as would be consistent with literature reports.[81,85] There is no difference within the error of the fitting between the ratios of the oxide peaks and typical iron sulfide peaks when the ten minute and four hour samples are compared. So although the ten minute growth time sample shows indications of crystalline changes via XRD, the XPS data for both samples look nearly identical. It appears as though both samples undergo similar oxidation changes.

2.4 Conclusion:

This chapter has demonstrated the successful synthesis of phase pure pyrite nanoparticles by multiple synthetic routes utilizing both amine and phosphines surfactants. It also shows control over particle morphology over time with individual, defined particles at longer growth times. However, even at long growth times, long-term nanoparticle suspension has not been achieved. Both XRD and XPS studies show that these pyrite samples oxidize over time, which is not unexpected, although this is the first time it has been confirmed via high resolution XPS. The following chapter will address the issues of suspension and surface chemistry in detail and solutions to improve surface chemistry will be presented.

CHAPTER 3: TUNING THE SURFACE CHEMISTRY OF PYRITE NANOCRYSTALS THROUGH SYNTHESIZING CORE/SHELL STRUCTURES: A ROUTE TO ENHANCE PHOTOVOLTAIC PERFORMANCE

The synthesis, characterization and manuscript preparation for this thesis chapter were performed by Sarah J. Fredrick. Daniel Agocs graciously contributed to the work by performing Rietveld analysis, in addition to useful conversation and editing assistance. Amy L. Prieto contributed ideas, discussion and editing help.

3.1 Introduction:

Research on iron pyrite, FeS_2, has received renewed interest in the last 5 years, largely due to its promising photovoltaic properties and cheap, earth-abundant constituents. In fact, since 2009, when an influential perspective paper by Wadia and coworkers[13] identified pyrite as the most promising PV material in terms of cost and potential, 483 papers have been published on the material (according to a SciFinder search in which both "pyrite" and "FeS_2" were included in the search and patents were excluded). Yet, even with renewed interest and many excellent scientific findings, the highest reported efficiency for a pyrite solar cell is a dismal 3 % (as compared to the 20 % predicted efficiency), achieved in 1993.[40] The poor efficiency was attributed to a low photovoltage (only 1/5 of the predicted value). Much recent work has sought to explain this problem and many theories have been put forth. Early ideas were largely focused on sulfur deficiencies in the samples.[56,86] Sulfur deficiencies create deep trapped states in the band structure, and thus hinder photovoltaic performance.[56] Additionally, it was thought that these trapped states were largely at the surface of the material, and thus the surface chemistry ultimately changed the band structure of the material enough to decrease its performance

substantially.[62] Sulfur defects have also been calculated to be responsible for the rapid surface oxidation of pyrite.[58]

An area of renewed study in recent work is the detailed transport properties of pyrite studied through Hall measurements. A common observation related to the transport properties is their low room-temperature resistivity (~ 1 Ωcm or lower).[47,48,87,88] This is a result of a high carrier concentration (10^{20} cm^{-3}) and low mobilities. Recent work has proposed several theories explaining this phenomenon including an intergranular hopping mechanism,[51] the presence of amorphous iron sulfide phases in the films,[14] and a hole-rich inversion layer at the surface.[89] While many theories have been proposed attempting to identify the problem, none have yet achieved the goal of improving on the low resistivity values to ultimately enhance PV performance.

The focus of this thesis chapter is tuning the surface chemistry of pyrite nanocrystals in a robust fashion that will thus improve on the reported transport properties. Nanocrystals are an optimal system for probing surface problems due to their high surface-to-volume ratio. With a disproportionately large number of surface states as compared to the bulk, any modifications to the surface chemistry should have a noticeable effect on the properties. Additionally, there have been many reports on the synthesis of pyrite nanocrystals, including reports claiming to exercise some control over size and/or morphology,[74,75,77-79,90,91] but most lack any analysis of the surface chemistry and related transport properties of the nanocrystals for PV applications. In one exception, Steinhagen and coworkers made photovoltaic devices utilizing pyrite nanocrystals as an absorber layer in a variety of architectures. None of the devices exhibited a PV response, and the conductivity of the nanocrystal films was characteristically high.[80] There is a need for work

in the field of pyrite nanocrystals in which the surface chemistry is linked to properties, and ultimately the PV properties are improved for the system.

There are a variety of routes to tuning the surface chemistry of nanocrystals. Much recent work within the nanocrystal community has been focused on replacing the bulky organic ligands inherently present on the surface due to the synthetic method with much smaller inorganic molecules that will improve electronic communication by decreasing the distance between nanocrystals and increasing film conductivity.[31,33-36,92] These approaches have been applied to achieve record efficiencies of over 8 % for nanocrystalline Pb-chalcogenide PV devices.[37] Another surface modification that is widely utilized in LED applications, among others, involves adding a layer of a different solid state inorganic material to the surface of the nanocrystal, creating a core/shell architecture. Although there has been research on many core/shell compounds, the material with the longest and most thorough research history is CdSe with various shell materials.[93] A common shell material is ZnS, due to its wide band gap and facile synthesis. In LED and biological applications, it is advantageous to have a wide gap material as the shell because it traps charge carriers thus increasing recombination rates and overall luminescent efficiency. Although recombination is not desired for PV applications, a similar approach may be beneficial for use in pyrite systems because of the potential to carefully tune the surface chemistry.

Pyrite nanocrystals have traditionally suffered from a lack of suspension in solution, suggesting poor surface passivation, even when different ligand systems are used.[75,78,94] We, too, have observed this experimentally in our work synthesizing pyrite, indicating that the pyrite-ligand interactions are very weak, resulting in agglomeration and lack of solution stability. For this reason, ligand exchanges are not an effective route to achieving robust surface treatments on

pyrite. Described in the current chapter is a novel surface treatment on pyrite nanocrystals intended to reduce surface defects (typically sulfur vacancies) and result in an enhancement of photovoltaic properties. We present a method for synthesizing pyrite nanocrystals with a thin layer of zinc sulfide on the surface. The pyrite phase is confirmed by X-ray diffraction and the surface treatment is analyzed using X-ray photoelectron spectroscopy. Finally, preliminary transport measurements are made to probe whether the surface treatment had any effect on the electronic properties of the material.

3.2 Experimental:

Materials and Methods: All synthesis and purification steps were performed on an Ar Schlenk line or in a N_2 glove box with appropriate air free techniques. The following were purchased from Sigma Aldrich and used as-received: $FeCl_2$ (98 %), sulfur (reagent grade, purified by sublimation), diethylzinc solution (1M in hexanes). Oleylamine (OLA, 80 – 90 %) was purchased from Acros Organics and sparged with Ar or N_2 for at least 2 hours prior to use. Some batches of OLA were received with visible white flocculants in the normally light yellow liquid. If this was observed, the OLA was mildly heated (~ 60 °C) under vacuum for 1 hour prior to degassing with Ar. Octadecene (90 %, Aldrich) was sparged with Ar for 2 hours prior to use. ACS grade chloroform, acetone and isopropanol (Fisher Scientific) were degassed by the freeze-pump-thaw method before use in the glove box. Dimethylsulfoxide (DMSO, 99.9 %) was purchased from Fisher and degassed with Ar for at least 2 hours prior to use. Ammonium thiocyanate (Acros, 99+ % extra pure) was recrystallized in isopropanol and dried under vacuum prior to use.

Synthesis of FeS_2/ZnS: 126 mg (1 mmol) of $FeCl_2$ and 3 mL of OLA were added to a 25 mL flask equipped with a thermocouple and stir bar while 96 mg (3 mmol) of sulfur and 3 mL of

OLA were added to a scintillation vial and 4 mL of OLA was added to a 100 mL round bottom flask equipped with a thermocouple, condenser and stir bar. The clean OLA was heated at a rate of 500 °C/hr to 120 °C under vacuum, then cycled several times between vacuum and Ar before heating to 260 °C under Ar. The OLA remained light yellow for the duration of the heating. The $FeCl_2$ flask was heated at the same rate to 110 °C under vacuum and left until injection. The $FeCl_2$ solution was dark brown in color. The S/OLA was sonicated to dissolve all solids and left at room temperature until injection. Once the OLA flask reached 260 °C, the $FeCl_2$ and sulfur solutions were injected simultaneously using two 5 mL gas-tight syringes. The solution turned black immediately. This was left for 15 minutes at 260 °C and then the temperature was lowered to 220 °C for injection of the shell precursors. *Note: bare pyrite was made by quenching the reaction at this point by injecting the product into a mixture of isopropanol and chloroform. The particles were purified by the same procedure as the core/shell particles without further modification.*

Due to the fact that the observed bare pyrite nanocrystals are not uniform in size or shape, only a rough estimation was performed to determine the amount of zinc precursor required to create a shell thickness of three monolayers of zinc sulfide. At 220 °C, a solution of 0.25 mL of diethylzinc, 0.6 mL of OLA and 6 mL of ODE was added over a period of 45 minutes via syringe pump. Once the addition was complete, the temperature was lowered to 180 °C and left overnight (for 8 – 12 hours) to ensure complete formation of the shell. The resultant product was injected into a mixture of chloroform and isopropanol (4 mL each) and transferred to the glove box for purification.

The solid was precipitated by centrifugation and then resuspended in chloroform (typically a total of 16 mL of solution). This was centrifuged for 5 minutes to remove

agglomerates and the remaining suspended product was used for further characterization. The suspension was black in color and remained stable for weeks in an air-free environment. Unmodified pyrite particles all precipitated upon centrifugation (this difference was an initial indication of successful surface modification of the core/shell particles) so no suspended particles could be used for characterization. Rapid screening for phase purity via low-resolution XRD was done using the precipitated solid for both samples, not the suspended product. All other characterization (including high resolution XRD) was performed on the suspended core/shell particles and precipitated unmodified particles.

Characterization: Low resolution XRD was performed using samples drop cast onto zero background SiO_2 diffraction plates purchased from MTI Corporation. X-ray diffraction was performed on a Scintag X-2 Advanced Diffraction system equipped with Cu Kα radiation (λ = 1.54 Å). Transmission electron microscopy samples were prepared by diluting a small amount of suspended nanocrystals with hexane and sonicating for about 30 seconds. Then the TEM grid (formvar/carbon obtained from Ted Pella) was dipped into the nanocrystal solution three times and the excess solvent was wicked away after each dip. TEM analysis was performed on a JEOL JEM 1400 at a working voltage of 100 kV. Samples for high resolution synchrotron powder XRD were prepared by precipitating suspended core/shell particles using acetone and centrifugation (or using already precipitated, unmodified particles). The samples were then dried under vacuum and ground with a mortar and pestle to ensure they were a fine powder. They were then loaded into quartz capillaries and sealed with epoxy before loading into the Kapton tubes and sample bases for beam line 11-BM at the Advanced Photon Source at Argonne National Laboratory. Data were collected using beamline 11-BM using an average wavelength of 0.41385 Å. Discrete detectors covering an angular range from -6 to 16 º 2θ were scanned over a 34º 2θ

range, with data points collected every 0.001º 2θ and scan speed of 0.01º/s. The data were analyzed via the GSAS/EXPGUI program (Larson, A.C.; von Dreele, R.B. Report No. LAUR 86-748. Los Alamos National Laboratory. 1994.). X-ray photoelectron spectroscopy samples were prepared by precipitating suspended nanocrystals using acetone and centrifugation, then drying them under vacuum. The unmodified pyrite particles were just dried under vacuum after purification. A small amount of solid was placed on carbon tape on the XPS sample holder. The samples were kept air free except for the several seconds required for transfer to the sample chamber on the instrument. XPS spectra were obtained using a Physical Electronics ESCA 5800 system with monochromatic Al Kα (E = 1486.6 eV) x-ray source. High resolution scans were performed with a pass energy of 23.5 eV and a step size of 0.10 eV/step. Data analysis was performed using Multipak software version 9.3.03. All spectra were shifted to account for charging, using carbon as a reference at 284.80 eV. Film thicknesses were estimated using a ZeScope Optical Profilometer by measuring the height at the edge of a film at multiple locations. Transport properties on nanocrystal films were measured on an Ecopia HMS-3000 Hall Measurement System. Conductive silver paste (Ted Pella) was used to make ohmic contact on ~1 cm^2 films.

Thin Film Fabrication: Thin films of unmodified pyrite were not fabricated due to the lack of suspension and persistent agglomeration. These experimental observations led us to believe that the nanocrystals were poorly capped and would not serve for ligand exchanges or making films. In several previous attempts to utilize pyrite nanocrystals in thin films, in the few cases where films could be made (they tended to be very thick and had cracks throughout), the pyrite readily peeled off of the glass substrate, making measurements on these films impossible.

Thus, there is no direct experimental comparison in electronic properties between bare and core/shell nanocrystalline films.

In order to fabricate useful films of the core/shell nanocrystals, a ligand exchange had to be performed to remove the insulating OLA ligands. Many unsuccessful attempts were made to perform a ligand exchange. These typically included layer-by-layer dip coating with a variety of ligands and solvents,[95,96] and also biphasic ligand exchanges as previously demonstrated by the Talapin group and others.[32,34] The layer-by-layer method would only allow for one layer of nanocrystals to adhere to the glass surface, and the OLA ligands were not removed. These thin films were highly insulating, and thus were not analyzed for electronic properties.

Adapted from a preparation by Fafarman and coworkers,[33] a crude ligand exchange was performed on pyrite nanocrystals to replace the native OLA ligands with ammonium thiocyanate (NH_4SCN) by the following procedure. A small amount, 100 mg, of recrystallized NH_4SCN was dissolved in 10 mL of acetone. This solution was added to the suspension from one reaction of core/shell particles (16 mL of particles in chloroform). This was sonicated for 10 minutes, then centrifuged to precipitate the solid. The supernatant was discarded and 10 mL of acetone was added to the product to rinse off excess ligand and it was again centrifuged to precipitate the product. Finally, 6 mL of DMSO was added to the solid and it was sonicated for 2 minutes. The dispersion was stable for several hours, but precipitated readily after that time frame. This dispersion was used immediately to fabricate thin films.

Glass pieces measuring ½ inch by 1 inch were prepared by sonicating for 10 minutes in each of the following solutions in this order: isopropanol, deionized water with dish soap, isopropanol and milipore water. The glass pieces were dried individually under vigorous nitrogen flow immediately prior to use. It was found that spin coating did not produce films thick

enough to use for transport measurements. Therefore, samples were drop cast directly from the DMSO solution onto glass pieces on a hot plate at 80 °C and the DMSO was allowed to evaporate. The films were screened for conductivity using a multimeter, and those that were conductive were shaped into 1 cm^2 areas for Hall probe testing (see supporting information Figure S3.1 for a photo). The films were not completely conformal and showed some cracks in spots. Film thickness was measured using an optical profilometer, and the thickness was on the order of 0.5 to 1 μm.

3.3 Results/Discussion:

The synthesis of pyrite nanocrystals has suffered from some experimental difficulties, especially in terms of nanocrystal suspension. Some reports have claimed that specific ligands can be used to form a relatively stable colloid, but even in these reports, the nanocrystals tend to precipitate easily with normal purification procedures.[75,94] Experimentally, we have observed similar problems in a variety of pyrite syntheses. We have never observed nanocrystal suspension for a sustained period of time, regardless of capping ligand or synthetic protocol (injection temperature, growth time, precursors, etc.). In fact, even when nanocrystals were sonicated with an excess of a capping ligand (e.g. oleylamine), the dispersion only lasted several minutes before the particles began to precipitate. The first indication of successful surface modification with zinc sulfide was the long-term (up to several weeks or months) suspension of nanocrystals. After purification, a dark suspension of core/shell nanocrystals remained in chloroform, whereas any unmodified pyrite nanocrystals purified by the same procedure always precipitated during centrifugation. Particles of pyrite and corresponding core/shell particles were characterized side-by-side to quantify differences between the products.

As a starting point for characterization, low resolution X-ray diffraction was performed to check for phase purity. Under some reaction conditions (e.g. different zinc precursors or surfactants/solvents) extra peaks were present in the diffraction pattern. These peaks typically were identified as zinc sulfide, but sometimes were unidentifiable. Many peaks from ZnS can overlap with pyrite, making the analysis of ZnS phases difficult by low-resolution XRD. In most literature reports for the synthesis of CdSe/ZnS core/shell particles, TOP is used as a solvent for the diethylzinc. In the case of pyrite, TOP was found to leech sulfur out of the pyrite nanocrystals resulting in a mixture of FeS_2 and sulfur deficient phases (usually FeS). Under the reaction conditions described in the experimental section, cubic iron pyrite is the only crystalline phase present for both FeS_2 and FeS_2/ZnS samples. To obtain more detailed information about the crystal structure of these particles, high energy X-ray diffraction was performed using the Advanced Photon Source at Argonne National Laboratory.

Rietveld analysis confirms the presence of a crystalline pyrite phase in both samples. Of further interest, all peaks in both samples can be indexed to pyrite reflections. Though ZnS can exhibit Bragg peaks in similar locations to pyrite, the pyrite fit accounts well for all peak intensities (Figure 3.1), suggesting the absence of a crystalline ZnS phase. The

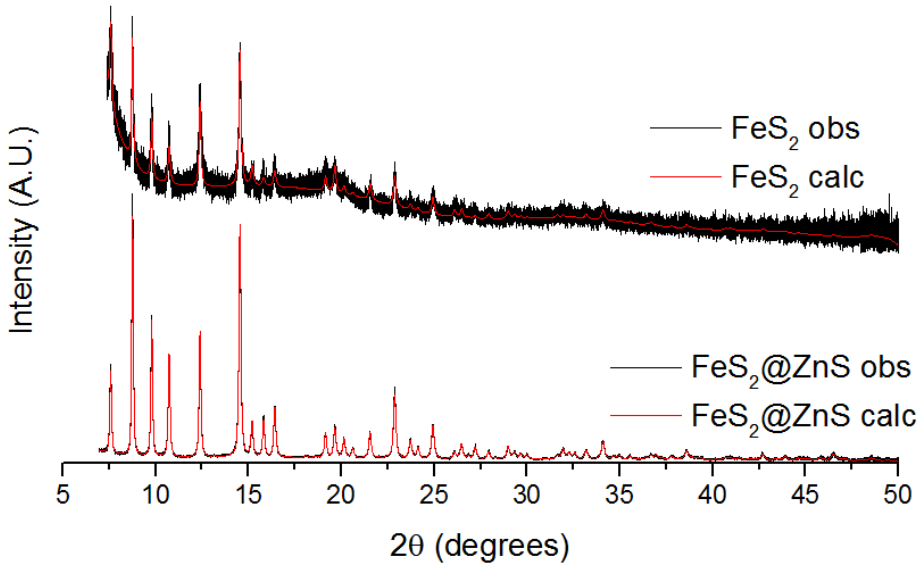

Figure 3.1: Rietveld fits of phase-pure pyrite (top) and FeS_2/ZnS core/shell particles (bottom). Both samples are composed of only phase pure pyrite. The core/shell sample has no crystalline ZnS phase present. Scherrer analysis indicates a crystallite size of 32nm for pyrite and 113nm for FeS_2/ZnS.

presence of the ZnS was confirmed by XPS, which, when combined with XRD analysis, indicates a possible amorphous ZnS shell. Of significant interest also are the occupancies obtained by the Rietveld refinement. For the pure pyrite sample, analysis yields an occupancy of ~0.83 for sulfur, whereas in the core/shell sample, the sulfur occupancy is found to be 1.01. The values for the unmodified pyrite sample match well with previous research on pyrite, and theoretical studies on sulfur vacancies at the surface. The difference in the occupancy values also suggests that the sulfur deficiency is not present in the core/shell sample. These findings support that the ZnS shell may prevent the formation of sulfur-

deficient surface states, an advance that has not been previously reported for pyrite nanocrystals. Further, Scherrer analysis of the peak broadening of each sample reveals a crystallite size of 32nm for pure pyrite and 113nm for the FeS_2/ZnS particles. This large size difference is most likely due to the extended period of growth necessary in the core/shell particle synthesis, but does not directly correlate with the particle sizes obtained through transmission electron microscopy.

Transmission electron microscopy was used to probe the morphology of the nanocrystals and determine if there was any difference between unmodified and core/shell nanocrystals. The morphology of the nanocrystals in both samples is somewhat irregular, ranging in size from about 20 nm to 75 nm (Figure 3.2). Although there do not appear to be significant differences

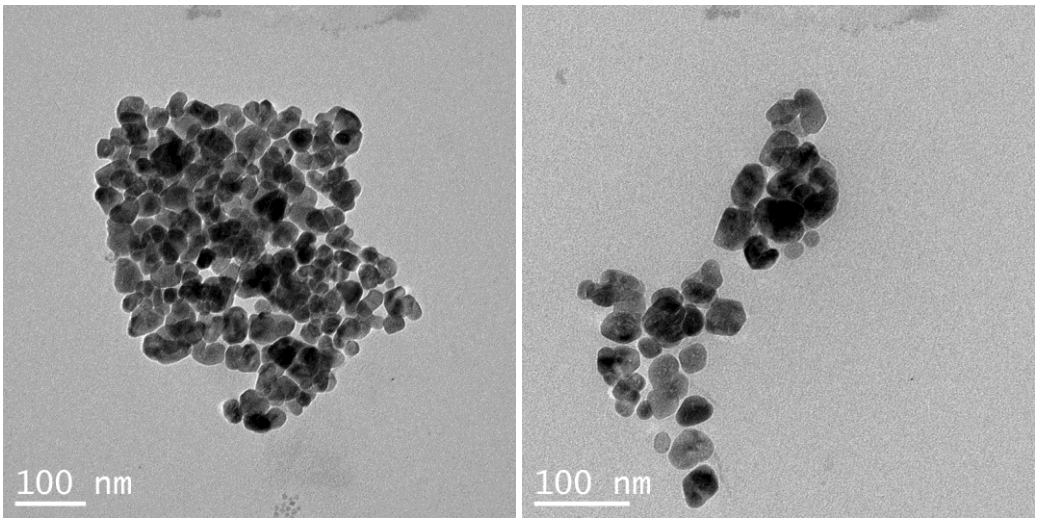

Figure 3.2: Low resolution TEM micrographs of a) bare pyrite nanocrystals and b) core/shell samples.

in the nanocrystal size or morphology between the two samples, there was some difference in the agglomeration of nanocrystals on the TEM grid. Generally, the unmodified pyrite only appears in large agglomerates, while the core/shell samples tend to have more individual particles with spaces in between them, and the grouping of particles together is much smaller than the agglomerations. We acknowledge that the ordering of nanocrystals on a TEM grid

cannot be directly correlated to solution behavior, but we believe this suggests greater agglomeration in the pyrite samples, while the core/shell samples do not tend to form these large agglomerates. This theory is supported by the fact that the core/shell particles form a stable dispersion, while the unmodified pyrite particles do not.

X-ray photoelectron spectroscopy is an excellent tool for probing the surface properties of a material. Many studies have been performed on bulk pyrite to identify surface states, and more specifically to monitor the oxidation of pyrite.[57,59-61] To our knowledge, there are no reports of high resolution XPS data on pyrite nanocrystals with proper fitting to determine binding environments for both iron and sulfur. We have performed XPS on both unmodified and core/shell nanocrystals and determined subtle differences in their surface composition. One important point of note is that the core/shell particles show a strong signal from zinc (supporting information figure S3.2). Additionally, the signal-to-noise ratio for the iron spectrum in the core/shell sample is significantly weaker than that of the bare nanocrystals. Although the S/N cannot be used as quantitative evidence since these were two different samples and many variables can affect the S/N, the authors note that in repeat experiments performed on these materials, the core/shell samples consistently showed a strong signal for zinc, and a weaker iron signal as compared to the bare particles. This suggests that zinc comprises the surface layer of the particles (roughly 1 – 2 nm in thickness) and the iron is beneath the zinc. The quantitative data analysis on iron binding environments corroborates this theory more concretely.

The iron spectrum for the bare nanocrystals is consistent with previous reports on bulk pyrite (Figure 3.3 top). The red (706.9 eV) and green (719.1 eV) peaks correspond to the $p_{3/2}$ and $p_{1/2}$ peaks for Fe^{+2}. [59,60,97,98] We will refer to these as the "bulk" Fe^{+2} states to distinguish

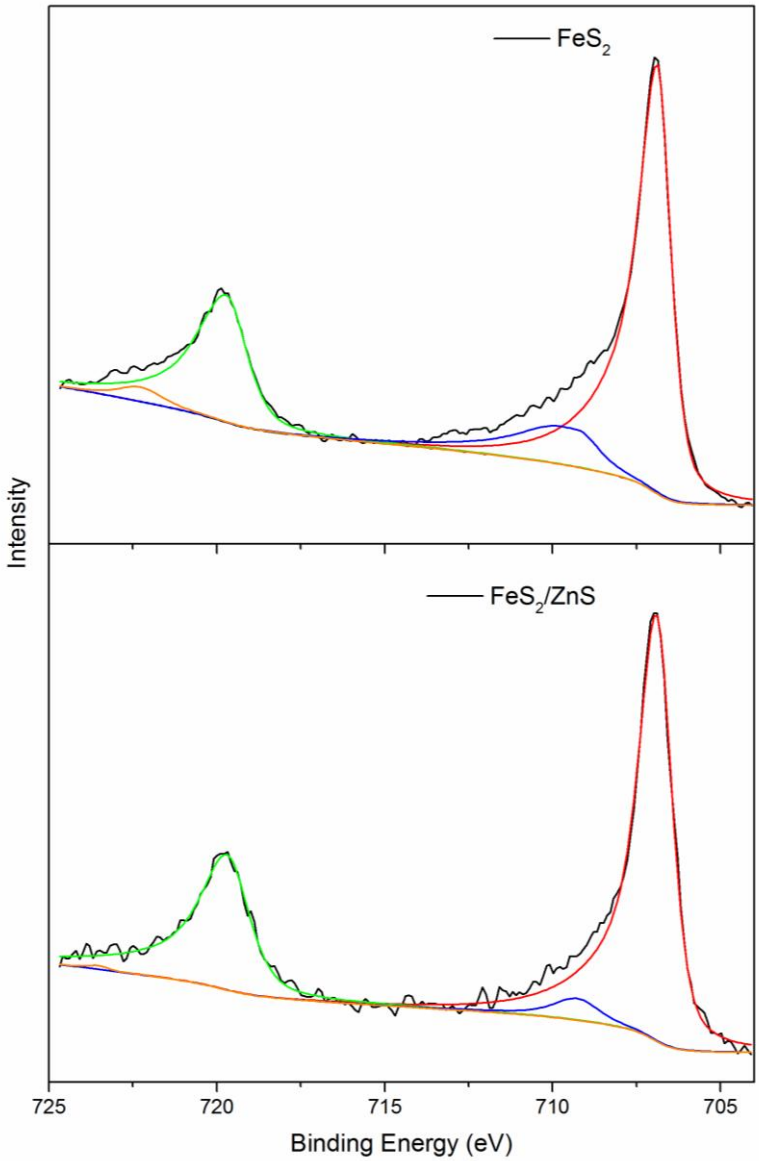

Figure 3.3: X-ray photoelectron spectra for bare (top) and core/shell (bottom) pyrite samples for the iron 2p region. The black traces are the raw data while colored traces are the fitted peaks.

them from the surface states, but this terminology should not be taken to suggest that these samples are bulk pyrite. The distinction is only made to distinguish the surface states from

interior states in the pyrite samples. The blue and orange shoulders on these peaks (709.3 and 721.5 eV respectively) have been attributed to iron multiplet peaks, or more likely in this case, iron surface states.[60] Iron is octahedrally coordinated in the FeS_2 crystal system, and surface states missing a sulfur atom have only five nearest neighbors. This is a problem that can have serious implications for the band structure of the material, including the creation of trapped states in the band gap that can hinder material performance.[86] It is not surprising that there is a significant contribution from surface states (blue and orange peaks) due to the large surface-to-volume ratio of the as-made nanocrystals. The iron spectrum for the core/shell particles is similar to the untreated nanocrystals with some intriguing differences (Figure 3.3 bottom). The Fe^{+2} "bulk" states are identical to those seen in the unmodified pyrite particles. However, the surface states have been reduced significantly. To attempt to compare the two samples, the ratios of the peak areas were calculated for the $p_{3/2}$ peaks (the red and blue). The area of the red "bulk" binding environment divided by the area of the blue "surface" binding environment gave an estimate of the bulk-to-surface Fe^{+2} in each sample. For the untreated pyrite, the ratio of "bulk" to "surface" states is 5:1, and for the core/shell sample, the ratio is 16:1. This significant reduction in surface states suggests less iron on the surface of the core/shell particles, which we suggest has been replaced by zinc.

The sulfur XPS data further supports the proposed core/shell structure. In Figure 4 (top) a typical spectrum for bare pyrite nanoparticles shows binding environments for the persulfide (S_2^{2-}) at 162.31 and 163.52 eV (red and green) and a small peak attributed to polysulfides at the surface at 167.76 eV (orange).[57] The core/shell sample is significantly more complex. There are two different binding environments for sulfur, one of which corresponds to the persulfide seen in the bare pyrite sample (again, red and green peaks). The lower energy binding environment

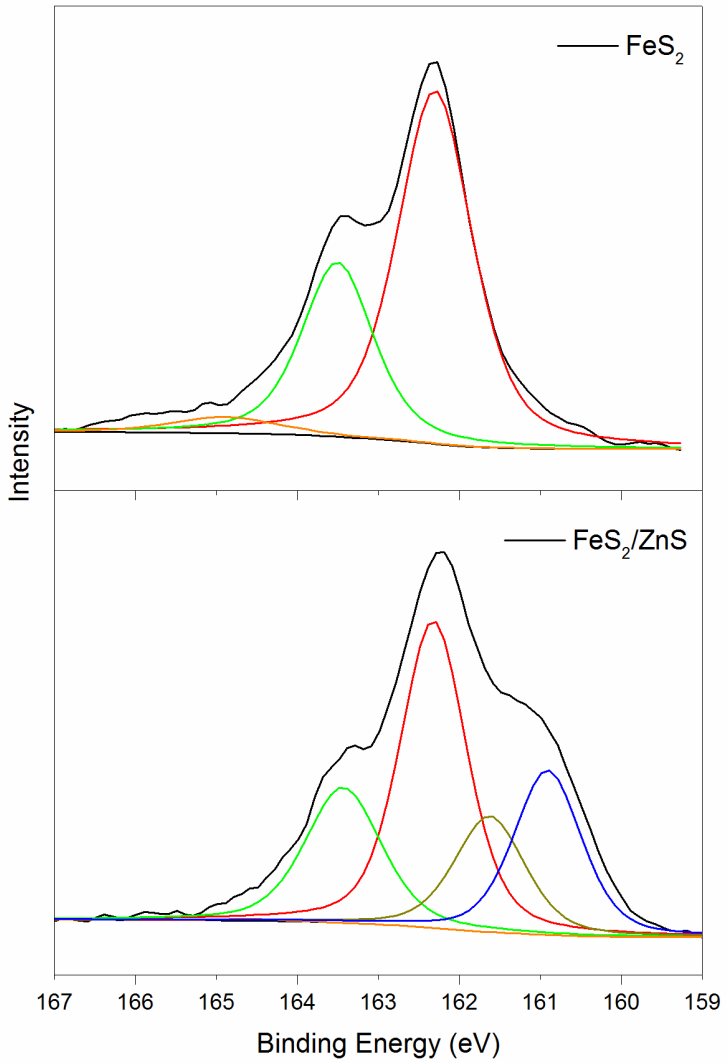

Figure 3.4: X-ray photoelectron spectra for bare (top) and core/shell (bottom) pyrite samples for the sulfur 2p region. The black traces are the raw data while colored traces are the fitted peaks.

seen at 161.62 and 160.91 eV (dark yellow and blue) corresponds to a monosulfide S^{2-}, which is present in zinc sulfide.[57] There is no sign of the surface polysulfides found in pyrite. It is possible that there is a very small amount of an intermediate sulfur binding environment as the persulfide gradually changes to the monosulfide, but a reasonable fit with a third binding environment of low intensity was not obtained. There are two clear binding environments for sulfur, suggesting the presence of both iron sulfide and zinc sulfide. This could merely be indicative of zinc sulfide particles forming in addition to the iron sulfide already present, but the Rietvelt refinement shows no sign of a crystalline zinc sulfide, which, in addition to the iron XPS data, supports the theory that a very thin surface layer of zinc sulfide is present.

Although this core/shell structure of pyrite is an exciting development in the field of pyrite research on its own, it is important to probe whether or not this modification improves the currently dismal state of pyrite nanocrystal performance in devices. It would be ideal to draw a comparison between the bare and core/shell pyrite, but we were never able to successfully make films of pyrite. This is unsurprising considering the lack of suspension in the unmodified sample, which makes ligand exchanges and film fabrication difficult. Previous reports on bulk and nanocrystalline pyrite will be used as a comparison for the transport properties reported herein. The major problem observed with pyrite nanocrystal films to date has been their exceptionally high conductivity. Films have typically been reported as having metallic conductivity, rendering them useless for photovoltaic applications.[47,48,87,88] Since it has been suggested that these transport properties in pyrite may be due to a hole-rich surface layer,[89] a thin coating with an n-type material like zinc sulfide may be an excellent candidate for returning pyrite properties to the predicted semiconducting nature of the material.

Preliminary Hall measurements were performed on films of the core/shell samples to determine if the surface treatment enhanced PV properties. A crude ligand exchange was performed using a report from Fafarman et al[33] to replace the oleylamine ligands with thiocyanate molecules (see experimental section for details). Films were drop cast onto clean glass and dried at 80 °C. The film thickness ranged from 500 nm to 1 μm. The films were not completely conformal, and some cracks were observed, but the conductivity of the material was high enough to perform room temperature Hall measurements on several films. The carrier concentrations reported were all on the order of 10^{16} cm^{-3}. This is a very promising result when compared with the bulk pyrite samples reported previously, where the carrier concentrations were on the order of 10^{19} and 10^{20} cm^{-3}.[14,48,87] The low mobilities (ranging from 1 to 0.3 cm^2/Vs) are not abnormal for nanocrystal films, especially when the ligand exchange was presumably only partial and has not been optimized. Finally, the room temperature resistivity of the films ranged from 100 - 300 Ωcm. These values are significantly higher than that of conventional reports of pyrite films, which are typically around 1 Ωcm or lower.[14,48,51] These measurements suggest vast improvements in the transport properties of the material, which may lead to improvements in overall efficiencies in photovoltaic devices.

3.4 Conclusion:

This chapter reports a synthetic advance in the field of pyrite nanocrystals. Pyrite nanocrystals were successfully coated with a thin layer of zinc sulfide, but without the formation of new zinc sulfide particles. The crystalline phase of the particles was confirmed using synchrotron X-ray diffraction and the surface chemistry was analyzed via XPS. The XPS data demonstrated a reduction in iron surface states and the presence of two different sulfur binding environments on the core/shell particles, indicating a surface layer of ZnS. Finally, the

transport properties were measured using a Hall probe and the conductivity of the pyrite films was significantly lower than literature reports, indicating the surface treatments may have even enhanced photovoltaic properties. This is the first report to our knowledge of a core/shell morphology for pyrite nanocrystals, and the first report of improved transport properties in nanocrystal films.

Acknowledgements:

Use of the Advanced Photon Source at Argonne National Laboratory was supported by the U. S. Department of Energy, Office of Science, Office of Basic Energy Sciences, under Contract No. DE-AC02-06CH11357.

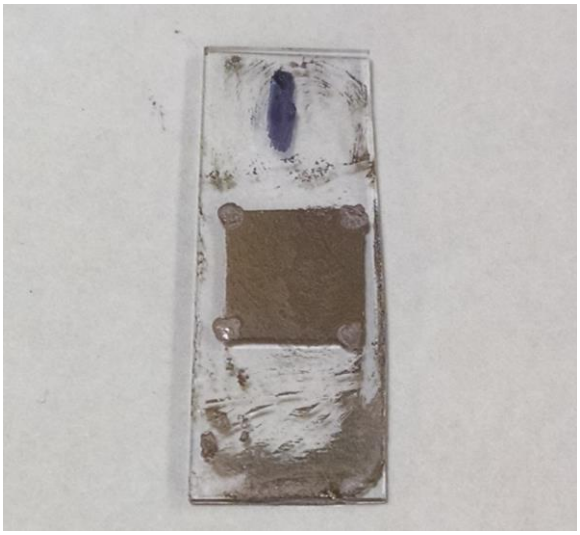

Figure S3.1: A photograph of a core/shell nanocrystal film used for Hall measurements.

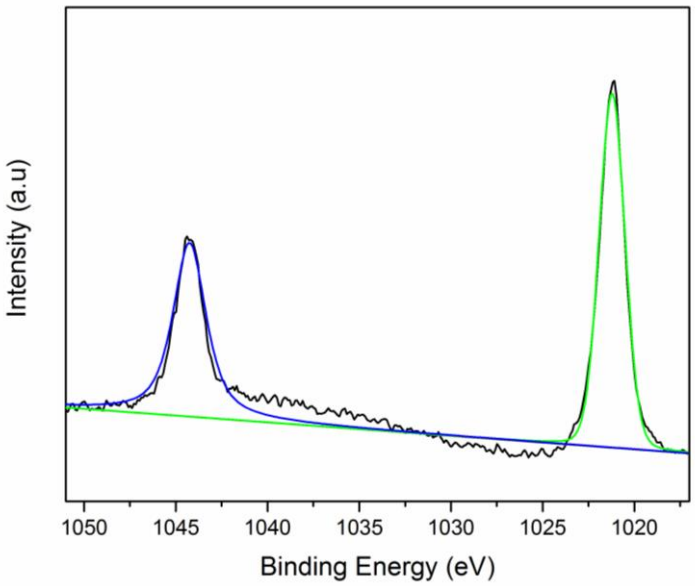

Figure S3.2: The zinc binding energy for core/shell samples demonstrating the presence of zinc on the surface of the nanocrystals.

CHAPTER 4: SOLUTION SYNTHESIS AND REACTIVITY OF COLLOIDAL FE_2GES_4: A POTENTIAL CANDIDATE FOR EARTH-ABUNDANT, NANOSTRUCTURED PHOTOVOLTAICS

The following thesis chapter was published as a communication in the *Journal of the American Chemical Society* **2013**, *135* (49) 18256-18259 and can be found online at http://pubs.acs.org/doi/abs/10.1021/ja408333y. All experimental work and manuscript preparation were completed by Sarah J. Fredrick with intellectual contributions and editing help from Amy L. Prieto.

In the race to find alternatives to carbon-based fuels, thin film solar cells composed of cheap, earth-abundant absorber materials are attractive for their potential to be economically competitive. One material receiving renewed interest is pyrite, FeS_2, because of its abundance and low cost, in addition to its large absorption coefficient (~10^5 cm^{-1}) and useful band gap (~0.9 eV).[13,45] In spite of such potential, the photovoltaic performance has been quite poor regardless of synthetic methods or measurements. In fact, the highest reported power conversion efficiency of 3 % (compared to the theoretical efficiency of 20 %), reported in 1993, has been attributed to very low photovoltages.[40] Various theories have been proposed seeking to explain the disparity between theoretically predicted performance and the experimentally measured properties including bulk and surface defects,[48,56,62,99] sulfur deficiencies,[86] small cores of metallic iron,[100] and domains of amorphous iron sulfide impurity phases with very small band gaps.[101] Although robust syntheses of pyrite nanostructures and thin films have been demonstrated, details of the photovoltaic properties are largely absent from the literature.[48,100,102-107]

Of the various proposed hypotheses for the poor performance, Yu et al. suggest that the primary hindrance to optimal PV properties for pyrite is the presence of sulfur deficient phases

that are more thermodynamically stable than stoichiometric FeS_2.[101] They propose an alternative class of iron chalcogenide photovoltaic materials: Fe_2MS_4 (M = Ge, Si), that could have the same attractive properties as pyrite, but with significantly better phase stability with respect to the decomposition into binary phases. These compounds are predicted to have high absorption coefficients ($>10^5$ cm^{-1}) and band gaps that are larger than that of pyrite (1.40 eV and 1.55 eV for the Ge and Si compounds respectively), ideal for solar absorption. These compounds have been well characterized structurally as well as magnetically, but we have no knowledge of reports of either of these materials being used in solar cells or synthesized as nanoparticles.

Nanocrystalline solar cell materials are of interest due to the advantage of low temperature processing and the potential to reduce the cost of fabrication.[19] Recent reports have demonstrated nanocrystalline solar cells reaching efficiencies up to 7 %,[108] demonstrating the great potential for commercial use. This is especially impressive considering some of the challenges associated with nanocrystalline PV devices (e.g. a large increase in the number of grain boundaries as compared to bulk systems and the insulating capping ligands present from the synthetic method, both negatively affecting transport properties). The first step for the incorporation of nanocrystals of new materials into PV devices is a well-developed synthesis of the nanocrystal building blocks. Herein we report a solution synthesis of colloidal Fe_2GeS_4 nanocrystals for potential use in solar cells, with particular attention paid to the stability of these particles in air.

Single crystal samples of Fe_2GeS_4 have been made by conventional solid-state methods, and have been structurally characterized.[2,109,110] This compound adopts an olivine structure with space group *Pnma* and exhibits interesting magnetic transitions as a function of temperature. To our knowledge, a solution synthesis has never been reported. Additionally, the optical and

photophysical properties have only been discussed in the aforementioned theory paper by Yu and coworkers, but have not been demonstrated experimentally.

Colloidal nanostructures of Fe_2GeS_4 were synthesized by the following method. Approximately 63 mg of $FeCl_2$, 220 mg GeI_4, 2.0 g of hexadecylamine (HDA) and 2.0 mL of octadecene (ODE) were heated to 320 °C. During the heating process, a solution containing 1.0 mL of hexamethyldisilazane (HMDS), 0.45 mL of hexamethyldisilathiane ($(TMS)_2S$), and 1.0 mL of ODE were injected into the solution at 120 °C. The reaction was left at 320 °C for 24 hours (see supporting information for experimental details and analysis of the effect of reaction growth time on phase purity and particle size).

The product was washed several times using a combination of acetone and hexanes to remove unreacted starting material. The final product was suspended in either hexanes or toluene. The colloidal suspension is a light brown color and is stable, as determined by the observation that the nanocrystals stay suspended in solution and do not precipitate out for weeks if stored in a nonpolar solvent in an oxygen-free environment.

The reaction conditions were chosen based upon empirical evidence and previous literature reports on similar materials. Hexadecylamine was used because of its relatively high purity (98 % versus the 70 % purity of oleylamine which is typically used in high temperature nanoparticle syntheses)[111] and high boiling point (330 °C). Germanium (IV) iodide was chosen as the Ge precursor because of its higher temperature stability as compared to germanium (IV) chloride. When reactions were performed with $GeCl_4$, the product was black, not the brown color indicative of the desired product, and a large amount of white residue (presumably unreacted $GeCl_4$) was present inside the condenser column, likely because of the volatility of the precursor at these reaction temperatures.

The reaction temperature of 320 °C was found to be critical. An example of the product formed from a reaction at a lower temperature (250 °C) is shown in Figure S4.1. None of the desired product is made at this temperature. There are several crystalline peaks that cannot be identified and do not appear to match any obvious phases (e.g. iron and germanium sulfides). Hexamethyldisilazane has been used in a variety of germanium chalcogenide syntheses, including some ternary compounds[112,113] and although its mechanism is not known, it is an important reactant in these syntheses. Reactions without HMDS produced a mixture of the desired product, GeS and FeS (Figure S4.2). We do not yet understand how the HMDS prevents the formation of impurity phases. It was also found that the $(TMS)_2S$ precursor was vital to obtaining the ternary compound. When sulfur powder was used as the sulfur source, the only phases detected via x-ray diffraction are iron sulfides, regardless of reaction temperature or time. An excess of Ge is also required to obtain a phase-pure product. The stoichiometric ratio of 2:1:8 of Fe:Ge:S was attempted with many reaction conditions and always produced a mixture of Fe_2GeS_4 and FeS. However, when a 2:1.5:8 ratio was used, the desired product was formed (see Figures S4.3 and S4.4 for details). X-ray diffraction data of aliquots at various reaction times shows that the desired product begins to form after only one hour at a temperature of 320 °C. However, the nanocrystals do not suspend at these short times. Additionally there is an extra peak at shorter times hours that is likely an iron sulfide phase. This phase is not present after 24 hours. A long reaction time gives a phase-pure colloidal suspension in which the particles do not precipitate out over time. Nanocrystals are stable up to 200°C, as evidenced by XRD showing no new peaks arise post-heating (Figure S4.5); however, peaks at higher 2Θ are not as well-resolved and may be an indication of some decomposition. All of the following data is for a reaction growth time of 24 hours. X-

ray powder diffraction data (Figure 4.1) shows only the presence of Fe_2GeS_4 with no additional peaks that would indicate the presence of impurity phases. TEM analysis was performed to determine particle size and morphology (Figure 4.2). The product is composed of plate-like structures of varying size and shape. Nanocrystal size was determined by measuring > 100 particle diameters and calculating an average and standard deviation. Particles that were

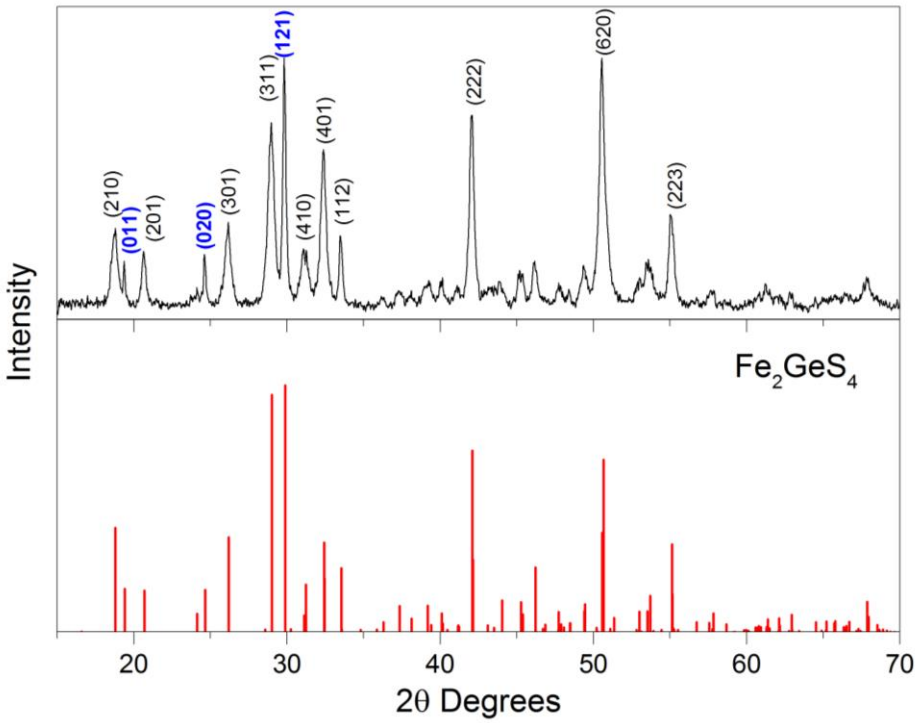

Figure 4.1: Powder x-ray diffraction of the Fe_2GeS_4 nanocrystals (top). Diffraction pattern simulated using Crystal Maker software (bottom). The original crystal structure data was obtained from reference 21.[1] Well-resolved peaks are labeled with (hkl) values and particularly narrow peaks are in blue.

oblong in shape were measured on both the long and short side and those two were averaged to obtain a single particle diameter. A size distribution of 75.9 ± 30.9 nm was determined. A high resolution TEM image showing the degree of crystallinity of the particles with corresponding FFT matched to Fe_2GeS_4 can be found in Figure S6. Further synthetic work will involve developing a better control over the size dispersion of the particles.

Due to the plate-like appearance of the nanocrystals, a more detailed analysis of the x-ray diffraction data was performed to identify planes of preferential growth. The full width at half maximum (FWHM) was measured for well-resolved peaks (all peaks labeled with hkl values in Figure 4.1) and three peaks were found to be significantly more narrow as compared to the

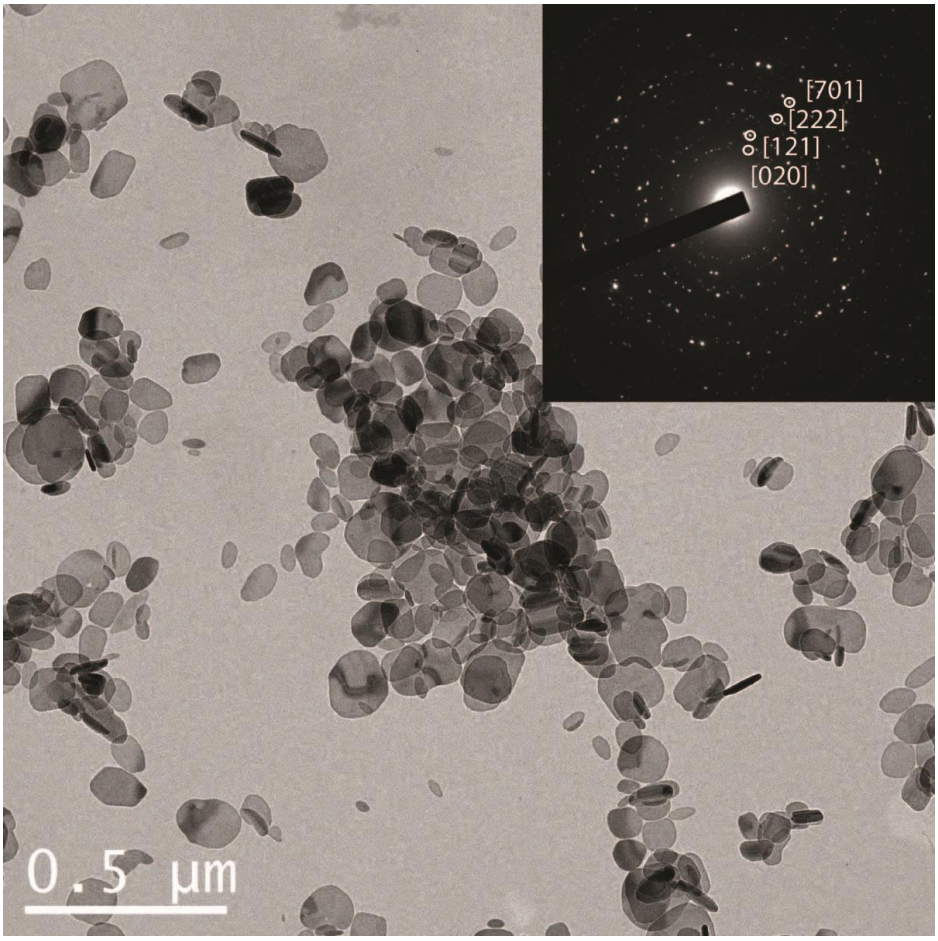

Figure 4.2. Low resolution TEM image of Fe_2GeS_4 nanocrystals after a 24 hour growth time. Inset: Selected area electron diffraction with four representative spots indexed.

rest. These three peaks represent the (011), (020) and (121) planes and are labeled in blue for clarity. The authors propose that these planes may be the growth directions in plane with the plates. There was not, however, a clear candidate for the orthogonal plane (as indicated by a significantly broader peak). The authors propose that the rapid growth in these three planes

may be due to the fact that they contain only Fe and S atoms. Experimentally, we noticed that the reactivity of germanium with sulfur was relatively low compared to that of iron with sulfur (as evidenced by the need for an excess of germanium and the preference for iron sulfide phases to form under different reaction conditions). It may be possible that planes containing germanium have slower growth rates, leading to the interesting geometry of the nanocrystals. Selected area electron diffraction was performed in hopes of further corroborating evidence of crystal growth planes. One would expect to see none of the peaks that were identified as particularly narrow in the XRD pattern if all of the nanocrystals were lying flat, in plane with the TEM grid. However, it was found that this was not useful due to the varied orientation of the nanocrystals on the TEM grids. As can be seen in Figure 4.2, the majority of the nanocrystals are lying flat, as plates, with the broad side in line with the TEM grid. However, some plates seem to be oriented completely perpendicular to the grid (see Figure S4.7 for an additional example).

One of the advantages of using nanocrystals to make solar cells is the potential for fabrication on the bench top via processes such as dip and drop casting. Thus, air stability is a desired property, although not a requirement. Due to the lack of current research on the material, there are no reports of the air-stability of Fe_2GeS_4. We performed x-ray photoelectron spectroscopy experiments to determine the initial bonding environments of Fe, Ge and S and also to monitor potential changes over time. Four identical experiments were performed: one initial sample was analyzed with as little oxygen exposure as possible (details in supplemental information). The same sample was left in air for two hours, 12 hours and 24 hours and analyzed after each time to monitor changes upon exposure to air. The results were quite dramatic.

It is well established in the literature that the Fe XPS can be convoluted by the presence of multiple oxidation states, local bonding environments, and surface states.[114-116] In particular, different iron species, especially Fe(III) and various iron oxides that can arise upon exposure to air, will overlap. Furthermore, the high percentage of surface states present in these high surface

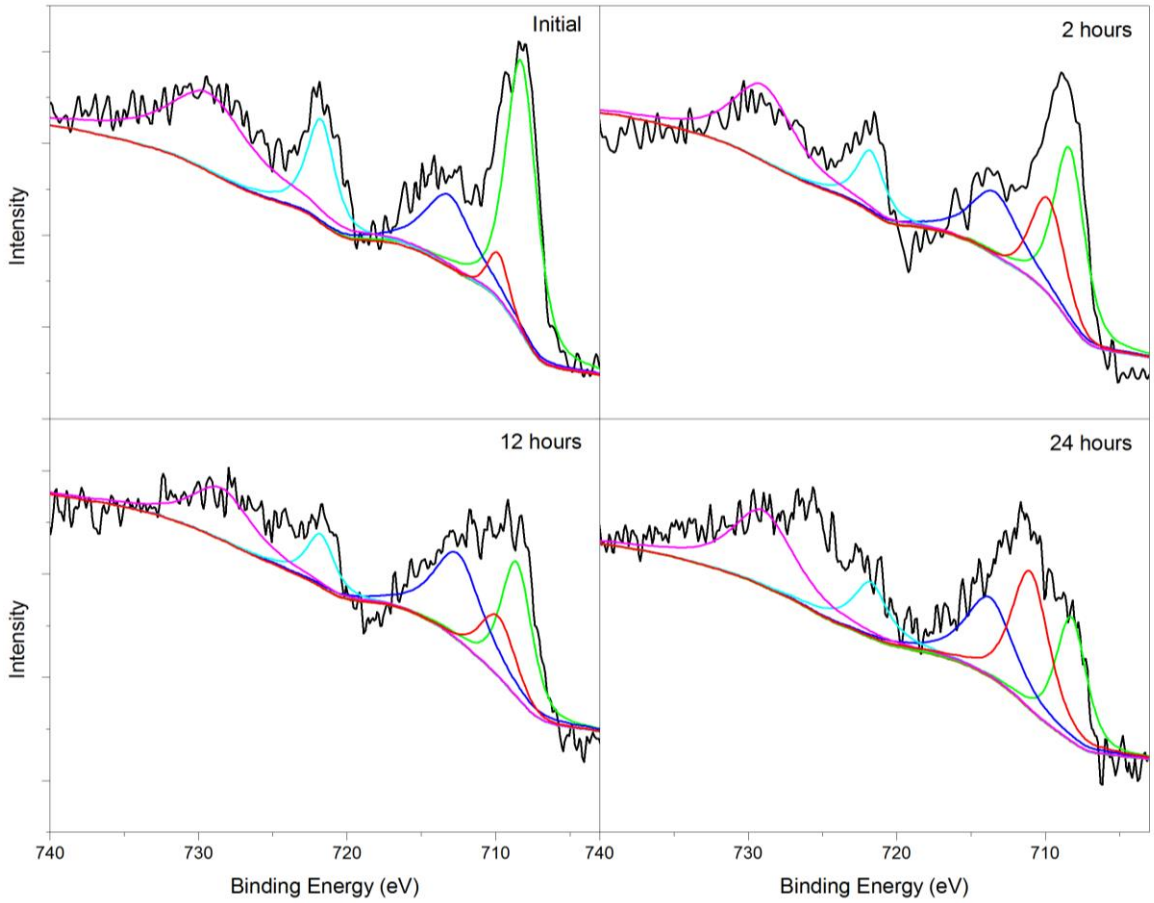

Figure 4.3. X-ray photoelectron spectroscopy of the Fe 2p energy range for four different times of air exposure: (clockwise from top left) initial, 2 hours, 12 hours and 24 hours. Black traces are raw data and colored traces are fitted peaks.

area materials will add an additional degree of complexity. The authors do not seek to definitively identify all of the species present in the Fe_2GeS_4 samples, but rather to identify general trends that may be indications of inherent properties and stability. Figure 4.3 shows the Fe 2p XPS spectra for all air exposure times. The black traces are the raw data, while the colored traces are the fits. A typical Fe(II) sulfide spectrum with no Fe(III), surface states, or

multiplet impurities would only contain the green (708.3 eV) and light blue (721.8 eV) peaks.[97,98] It is clear that even in the initial scan, a variety of Fe binding environments are present. We suspect that this is due to rapid oxidation in the several seconds of air exposure during transfer to the XPS chamber rather than an inherent mixture of Fe binding environments (which would not be expected from the structure). What becomes clear over time is the continued oxidation from Fe(II) to Fe(III) occurs in air (dark blue and magenta), resulting in an increase in the area under the curve for Fe(III) as compared to the Fe(II). The red trace is another species that increases over time. This fit is assigned to FeO which is consistent with the literature.[85,98] Although these data are not definitive in species identification, it is apparent that the Fe species change significantly upon exposure to air.

The Ge XPS spectra provided a much more straightforward picture of the chemical changes occurring in the sample (Figure 4.4). Initially, the Ge exists almost entirely in a binding energy range that is typical for germanium (IV) sulfide (reported to be 30.4 eV)[117] shown with the red fit. The data exhibit a small shoulder, indicating the presence of a higher energy binding environment (green trace), more typical of Ge(IV) oxide (32.4 eV).[117] This progression continues and after only 12 hours, there is more GeO_2 than GeS_2 (supporting information Table 4.1). The changes in the sulfur binding environment are minimal and are likely attributed to small amounts of polysulfides forming (Figure S4.8),[118] which is consistent

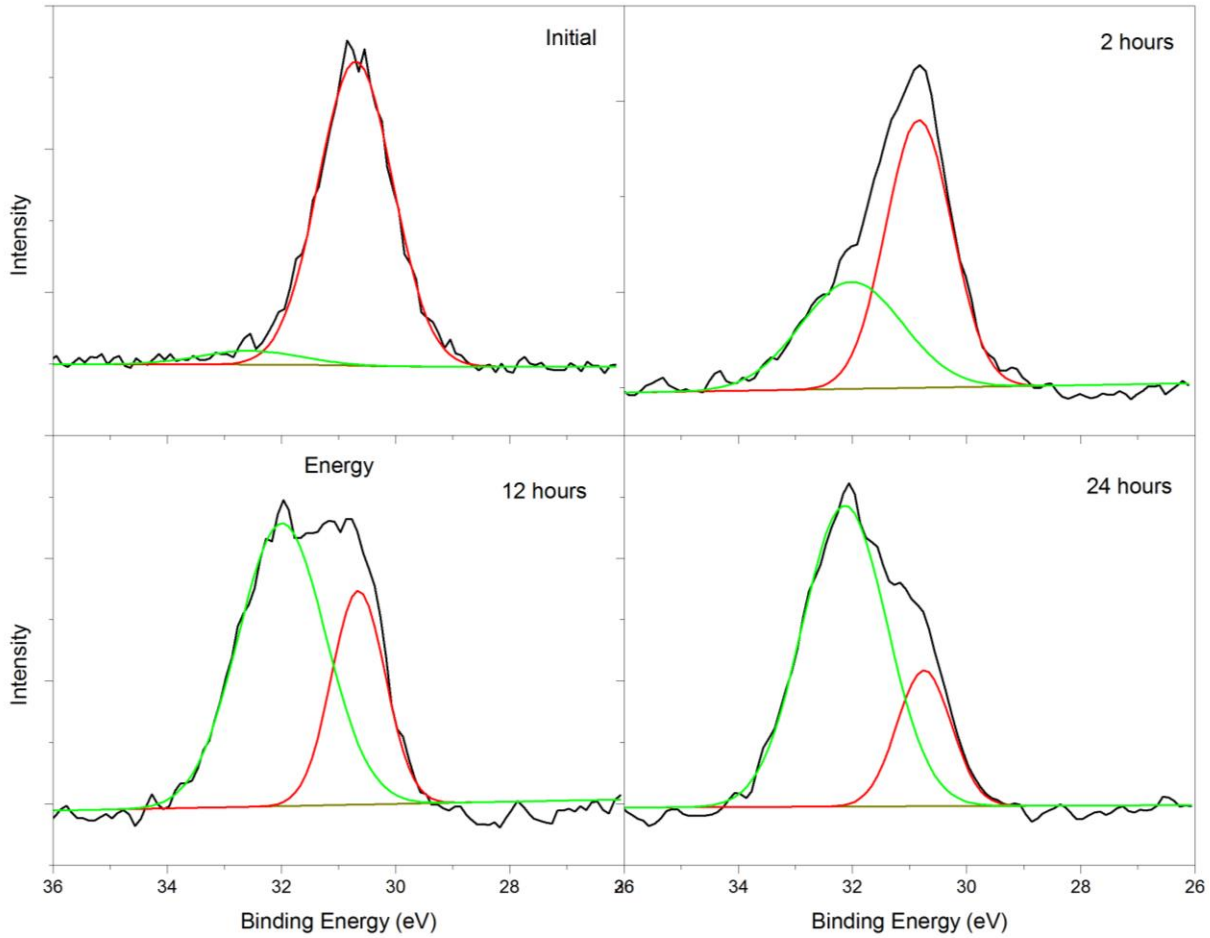

Figure 4.4. X-ray photoelectron spectroscopy data of the Ge 3d energy range for four different times of air exposure: (clockwise from top left) initial, 2 hours, 12 hours and 24 hours. Black traces are raw data and colored traces are fitted peaks.

with the general oxidation that is present in air. Although these changes are rapid and apparent in XPS, the oxides that form are amorphous and do not appear in the diffraction pattern.

High resolution TEM images have corroborated the data indicating an amorphous oxide layer forms upon exposure to air. Figure S4.9 shows a high resolution image of a particle with what appears to be a layer of amorphous material at the surface. Lattice fringes can be seen in the crystalline interior, however, they are not present in the outer layer, which is about 10 nm thick.

In order to determine the potential for future use in photovoltaics, UV-Vis spectroscopy and photoelectrochemical tests were performed on the nanocrystals. The UV-Vis spectrum exhibits a gradual onset of absorption (Figure S4.10), so we are not able to estimate a band gap. This could be due to the challenges often associated with the electronic transitions present for octahedral Fe(II), the presence of amorphous phases on the surface (particularly amorphous iron oxides, which exhibit similar broad absorption), or the presence of a range of other surface states. However, it is clear that the material does absorb in the visible region.

Thin films of the nanoparticles were made so that photoelectrochemistry could be used to characterize basic electronic properties. Photocurrent was measured in a three electrode photoelectrochemical cell (see supplemental information for details). This preliminary data shows that the photocurrent is generated at modest potentials under illumination with green light, and that the photocurrent is p-type, as expected (Figures S4.11 and S4.12). The current density is small, and it should be noted that the film thickness and ligand capping were not optimized, and although these samples were tested in a solution that had been thoroughly degassed with nitrogen, we cannot be sure that surface oxidation did not impede good transport within the films. Further optimization of the PEC setup including rigorous air-free

measurements and improved thin film fabrication are required for enhanced performance.

In an effort to demonstrate the potential for future surface modification to enhance properties and slow oxidation, a ligand exchange was performed to cap the surface with S^{2-} ligands[34] to ensure proper sulfide termination. We found a complete ligand exchange occurred, removing all HDA capping ligands as evidenced by changes in the IR spectrum (Figure S4.13). Furthermore, preliminary XPS data suggests that this simple ligand exchange slows the oxidation of the germanium species (Figure S4.14 and Table 4.1). There are a variety of other capping agents for nanocrystals that have been reported in recent literature.[96,108,119,120] Future work utilizing these capping agents is an advantageous route for mitigating the surface oxidation problems and enhancing PV properties. Studies are currently underway to explore surface treatments for Fe_2GeS_4 nanocrystals.

We have shown that phase pure Fe_2GeS_4 colliodal nanostructures can be synthesized from solution. The resulting nanostructures appear to be plate-like and remain suspended in solution for extended periods of time. They are highly air sensitive materials that will oxidize readily in air, however preliminary data suggest this oxidation can be slowed with surface treatments. The particles are p-type and readily produce photocurrent, indicating their potential for future use in solar cells. This is the first known report of Fe_2GeS_4 as a nanostructure and also the first report of photocurrent for this material.

Supporting Information: Solution Synthesis and Reactivity of Colloidal Fe_2GeS_4: A potential Candidate for Earth Abundant Nanostructured Photovoltaics

Materials and Methods: Iron (II) chloride ($FeCl_2$, 98 %), germanium (IV) iodide (GeI_4, 99.99 %), hexadecylamine (HDA, 98 %), hexamethyldisilazane (HMDS, for GC derivitization), hexamethyldisilathiane ($(TMS)_2S$, synthesis grade) were all used as received from Sigma Aldrich. Na_2S (anh) was used as-received from Alfa Aesar. 1-octadecene (90 % Aldrich) and formamide (ACS grade, 99.5 %, Fisher) were degassed by bubbling Ar gas through a solution for several hours. Hexane, toluene and acetone (technical grade) were degassed and used in a nitrogen glove box. All synthesis was performed on an Ar Schlenk line using appropriate air-free techniques. Washing and work up was performed in a nitrogen glove box.

X-ray diffraction was performed on a Scintag X-2 Advanced Diffraction system equipped with Cu Kα radiation (λ = 1.54 Å). The solid samples were drop cast from hexane onto a zero background SiO_2 sample holder. Rather than using a powder pattern from the ICSD to confirm the phase purity, a powder pattern was simulated using the Crystal Diffract program (ICSD database patterns only contained information up to 60° 2Θ). The atomic positions for the crystal structure put into Crystal Maker were obtained from reference 1 (Vincent, 1976).[2] TEM grids were prepared by dipping grids into a dilute suspension of the final product in hexane. Low resolution TEM analysis and selected area electron diffraction were performed on a JEOL JEM 1400 at a working voltage of 100 kV. High resolution images were obtained at the HRTEM facility at the University of Wyoming on a FEI Tecnai G2 F20 at a working voltage of 200 kV. UV-Vis spectra were obtained on an Agilent 8453UIV-VIS ChemStation spectrophotometer on a solution of suspended particles in hexane. Analysis was performed utilizing an air-free quartz

cuvette. XPS was performed on dry a powder adhered to carbon tape. The sample was stored in an air free container for transport to the XPS instrument and only exposed to air for several seconds for introduction into the sample chamber. XPS spectra were obtained using a Physical Electronics ESCA 5800 system with monochromatic Al Kα (E = 1486.6 eV) x-ray source. High resolution scans were performed with a pass energy of 23.5 eV and a step size of 0.10 eV/step. Data analysis was performed using Multipak software version 9.3.03. All spectra were shifted to account for charging, using inorganic carbon as a reference at 284.80 eV. Iterated Shirley backgrounds were used for all fits. FTIR spectroscopy was performed on a Thermo Scientific Nicolet 380 FTIR spectrometer using KBr plates. Nitrogen gas was used to purge the system during analysis.

Synthesis: The following were loaded in a N_2 glovebox into a 50 mL 3-neck round bottom flask equipped with a condenser and thermocouple: 63 mg (0.5 mmol) of $FeCl_2$, 220 mg of GeI_4 (0.38 mmol), 2 g of HDA and 2 mL of ODE. A scintillation vial was loaded with 0.45 mL of $(TMS)_2S$, 1mL of HMDS and 1 mL of ODE. The round bottom flask was heated to 320 ℃ at a rate of 500 ℃ per hour. At around 100 ℃, the flask was alternated between vacuum and Ar to remove water. At 120 ℃, the $(TMS)_2S$ /HMDS/ODE was injected and the solution immediately turned black. As the solution continued to heat, it turned from black to brown. Although the heating mantle was set to 320 ℃, it took about an hour and a half for the flask to maintain that temperature. The first portion of the reaction only reaches roughly 310 ℃. A white vapor can be seen above the brown solution for a large portion of the reaction time. After a given time, aliquots were taken and quenched by injecting into toluene. The product was washed by precipitating with acetone, followed by centrifugation and subsequent resuspension in toluene or hexane. This was repeated a total of three times. The final

product was centrifuged in either toluene or hexane to precipitate large agglomerates and the colloidal nanocrystals remained suspended in solution.

In order to study when the desired phase forms, a time study was performed by taking aliquots at various points in the reaction. The initial aliquot (top, S1) was taken immediately after injecting the HMDS/$(TMS)_2S$ solution at 120 °C. The second aliquot was taken once the solution reached 310 °C, at which point the timer was started to monitor reaction time for the following aliquots. These first two aliquots do not correspond to the final Fe_2GeS_4 product that is seen in all following aliquots. However, after just one hour at the appropriate reaction temperature, the desired product has begun forming. The first two aliquots have been searched exhaustively in the ICSD to identify the crystalline phases present at these times, but no matches have been identified. The long growth time was necessary to obtain particles that suspend for extended periods of time, even though the crystalline phase is present at much shorter growth times. There is, however, an extra peak present in the patterns for times shorter than 24 hours. After 18 hours this impurity peak (located at 43.5°, consistent with FeS) disappears. No appreciable difference was detected in the particle size distribution at different growth times. Even at short times, large plates are present (S4). Particle size estimates were not performed for shorter growth times because the particles tended to agglomerate and clump in the TEM images, making distinguishing individual particles difficult. This problem was not encountered in the 24 hour aliquot.

Supplemental Figures:

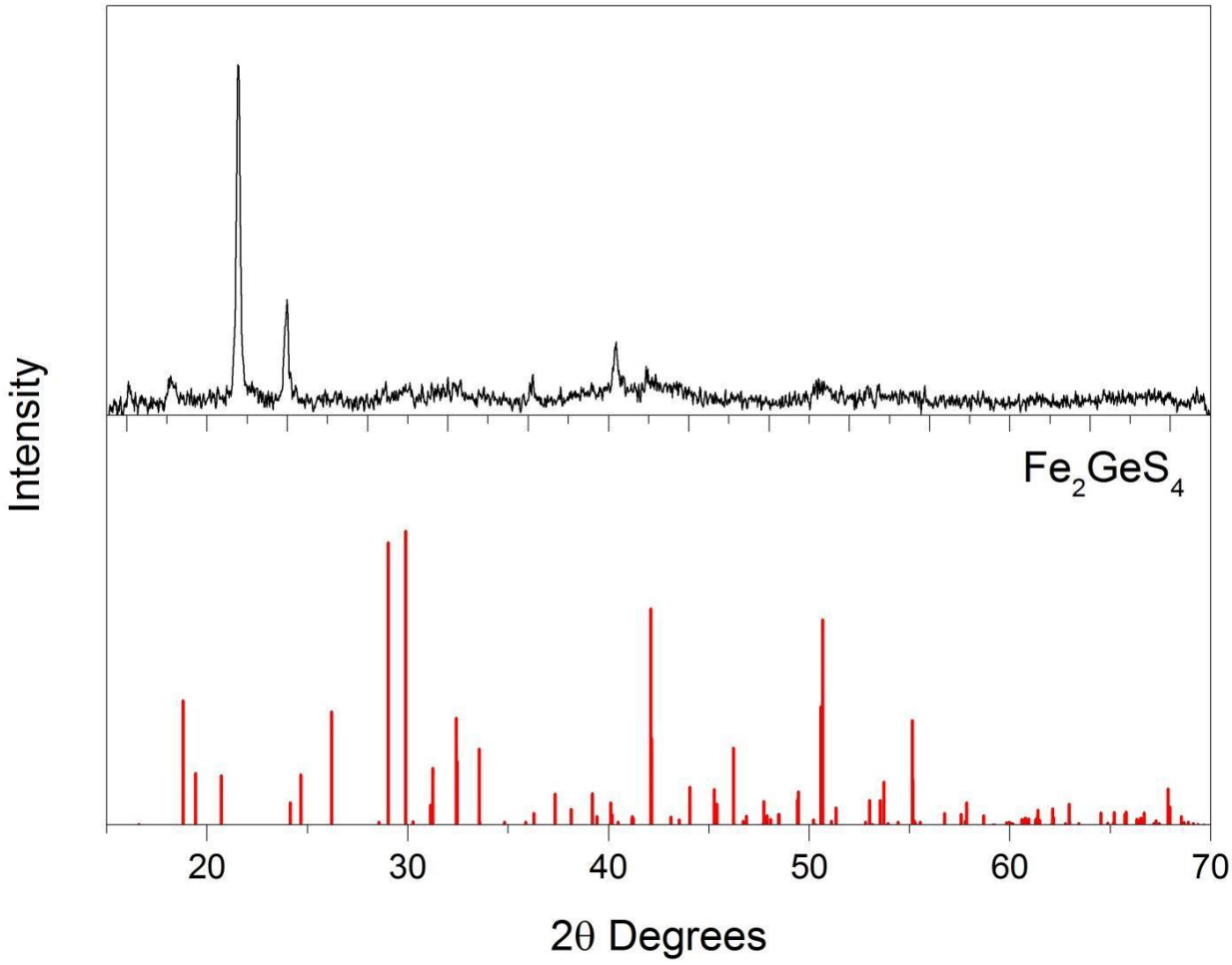

Figure S4.1: X-ray powder diffraction of a reaction performed at a growth temperature of 250 °C (top). The red pattern (bottom) is Fe_2GeS_4 as simulated by Crystal Maker. None of the desired product is formed at this temperature and the product formed has not been positively identified to match any known compounds in the ICSD.

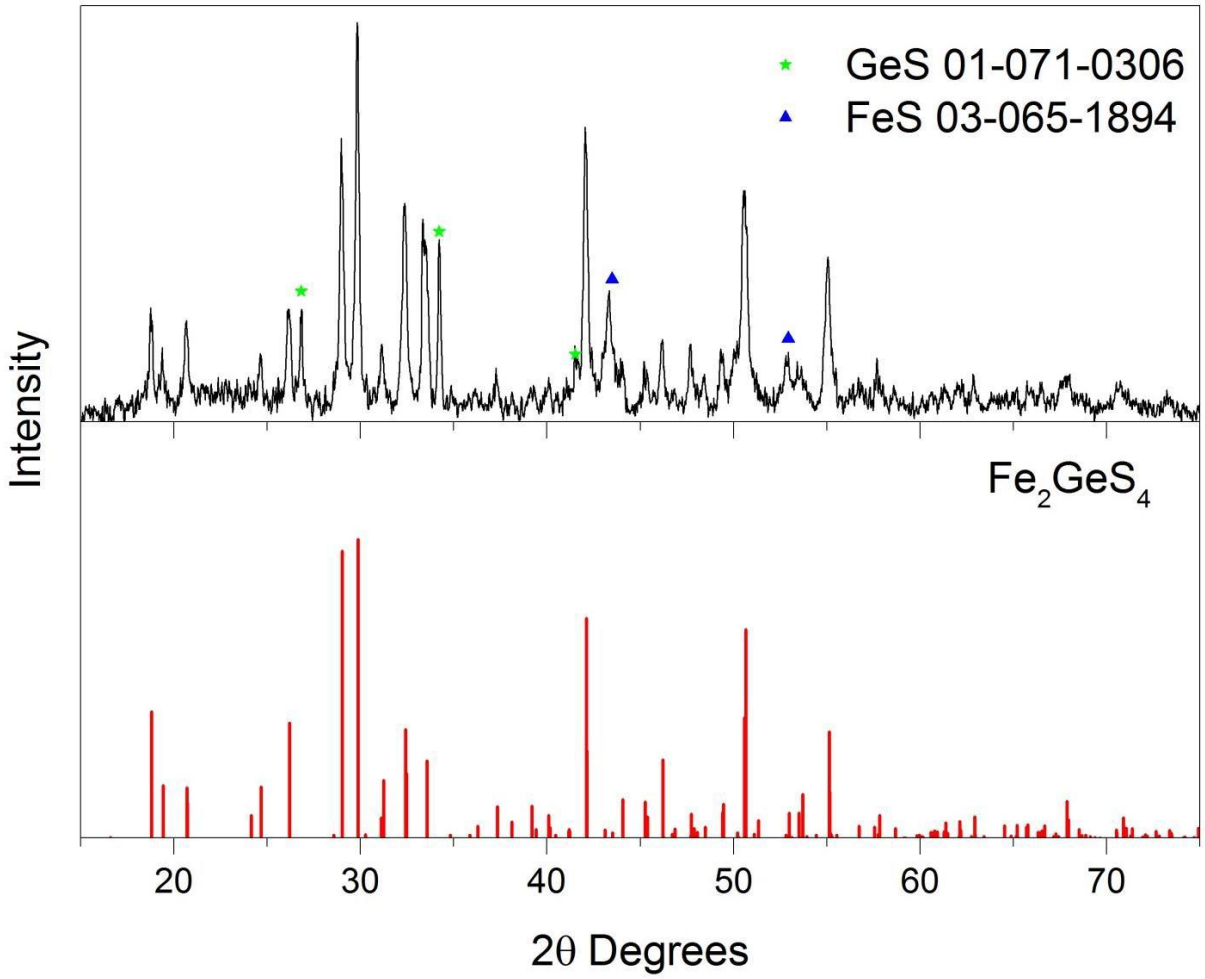

Figure S4.2: X-ray diffraction pattern of Fe_2GeS_4 synthesized without HMDS. The black trace is the raw scan (top). The red pattern is Fe_2GeS_4 as simulated by Crystal Maker. The peaks unique to GeS are marked with a green star (top) and FeS peaks are marked with a blue triangle (top).

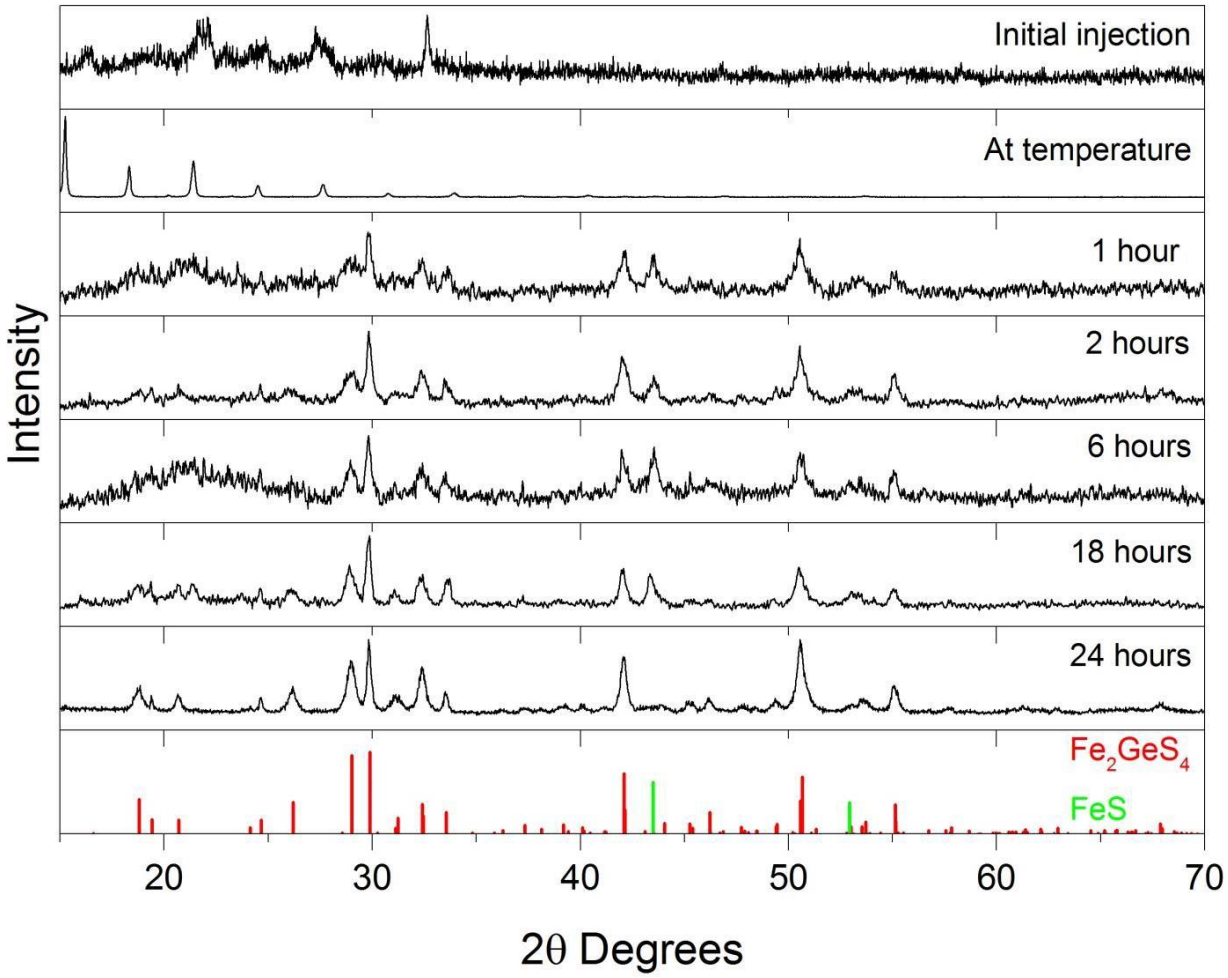

Figure S4.3: X-ray powder diffraction of aliquots at various reaction times. Red pattern (bottom) is Fe_2GeS_4 as simulated by Crystal Maker software. The green peaks are attributed to FeS (PDF 03- 065-1894). For clarity, the full pattern of FeS is not included, only peaks that do not overlap with Fe_2GeS_4 and therefore distinguish this impurity phase. Corresponding TEM images are shown in Figure S4.4.

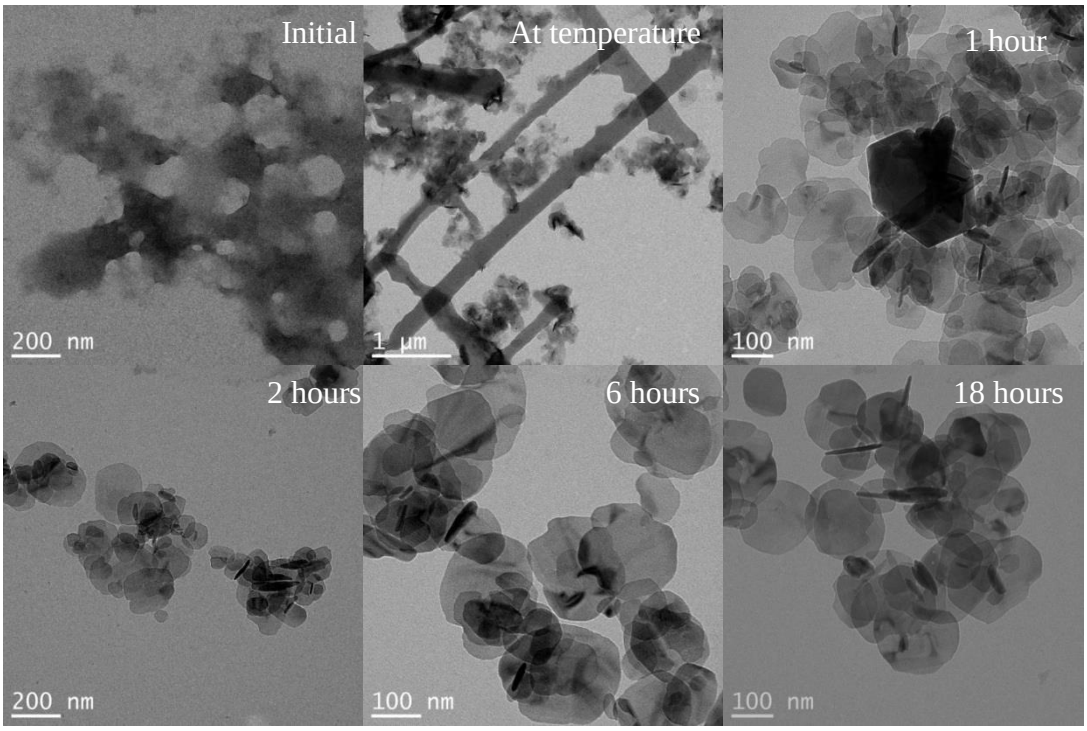

Figure S4.4: TEM images corresponding to the various growth times in Figure S4.1.

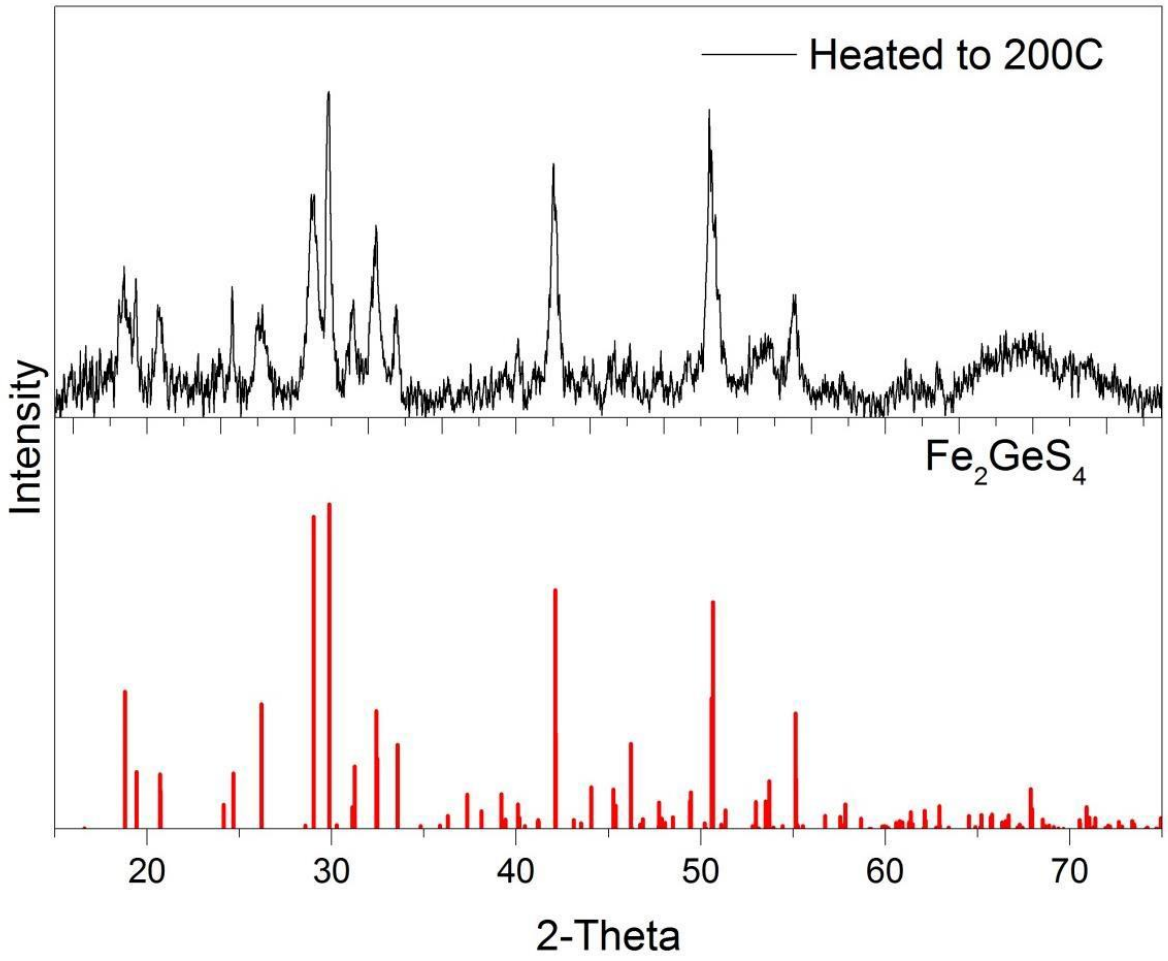

Figure S4.5: XRD pattern of a sample heated to 200 °C in a nitrogen atmosphere with excess sulfur present. No extra peaks arise with a heat treatment indicating the stability of the material under mild heating conditions.

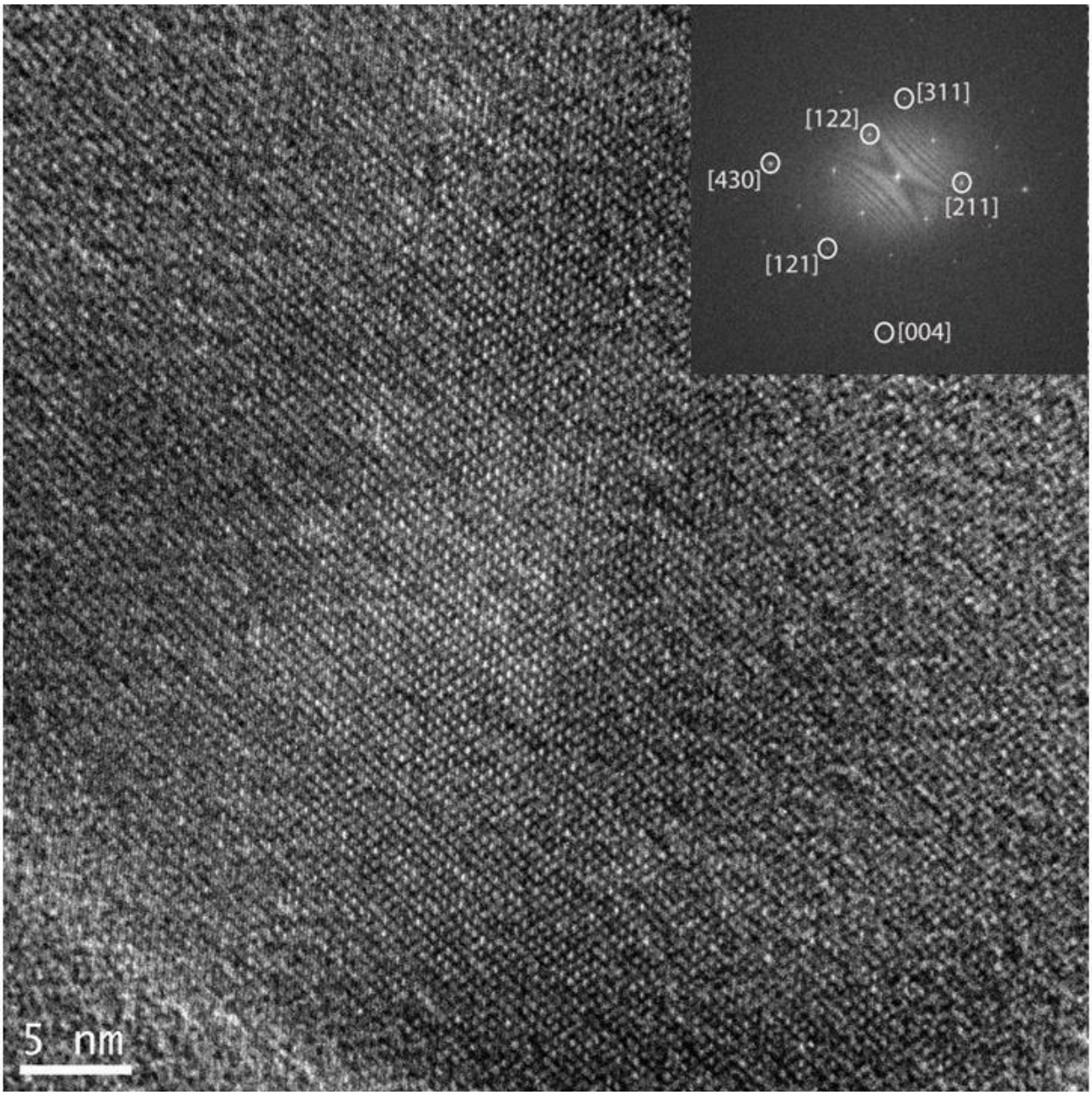

Figure S4.6: HRES TEM image of a Fe_2GeS_4 nanocrystal showing the crystallinity of the particle. Inset: corresponding FFT image with spots indexed to relevant crystal planes.

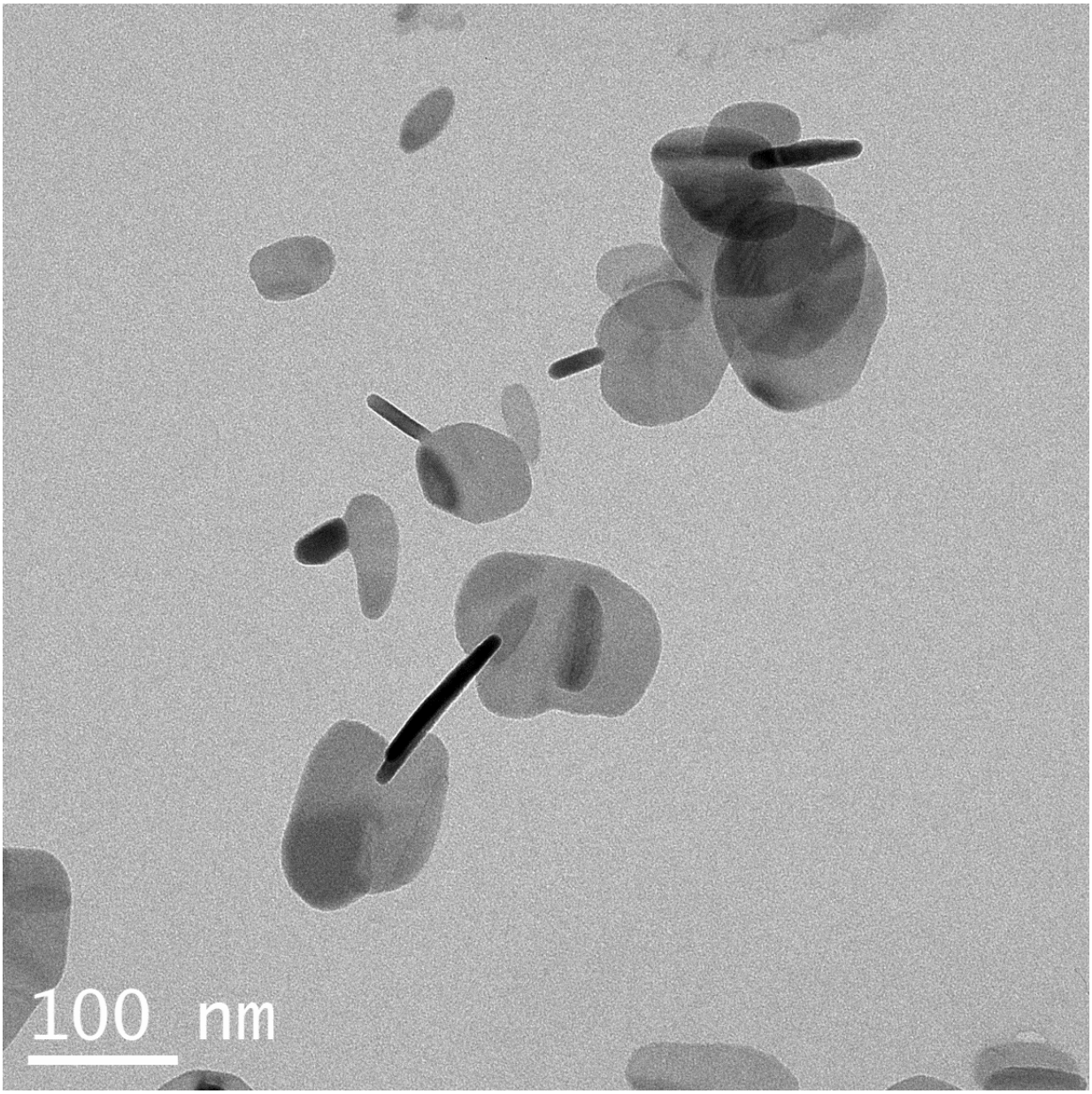

Figure S4.7: Low resolution TEM showing the two orientations of nanocrystals; one laying flat on the TEM grid and one perpendicular to the grid (seen as long, thin rod-like shapes rather than plates).

	GeS_2 Pre-treatment	GeO_2 Pre-treatment	GeS_2 Post-treatment	GeO_2 Post-treatment
Initial	94 %	6 %	97 %	3 %
2 hours	62 %	38 %	76 %	24 %
12 hours	32 %	68 %	54 %	46 %
24 hours	23 %	77 %	49 %	51 %

Table 4.1: Percentages of the oxide versus sulfide species in the germanium XPS spectra. Percentages were determined from peak areas of the GeS_2 species and GeO_2 species for the nanocrystals before (pre-treatment) and after (post treatment) a ligand exchange to S^{2-}.

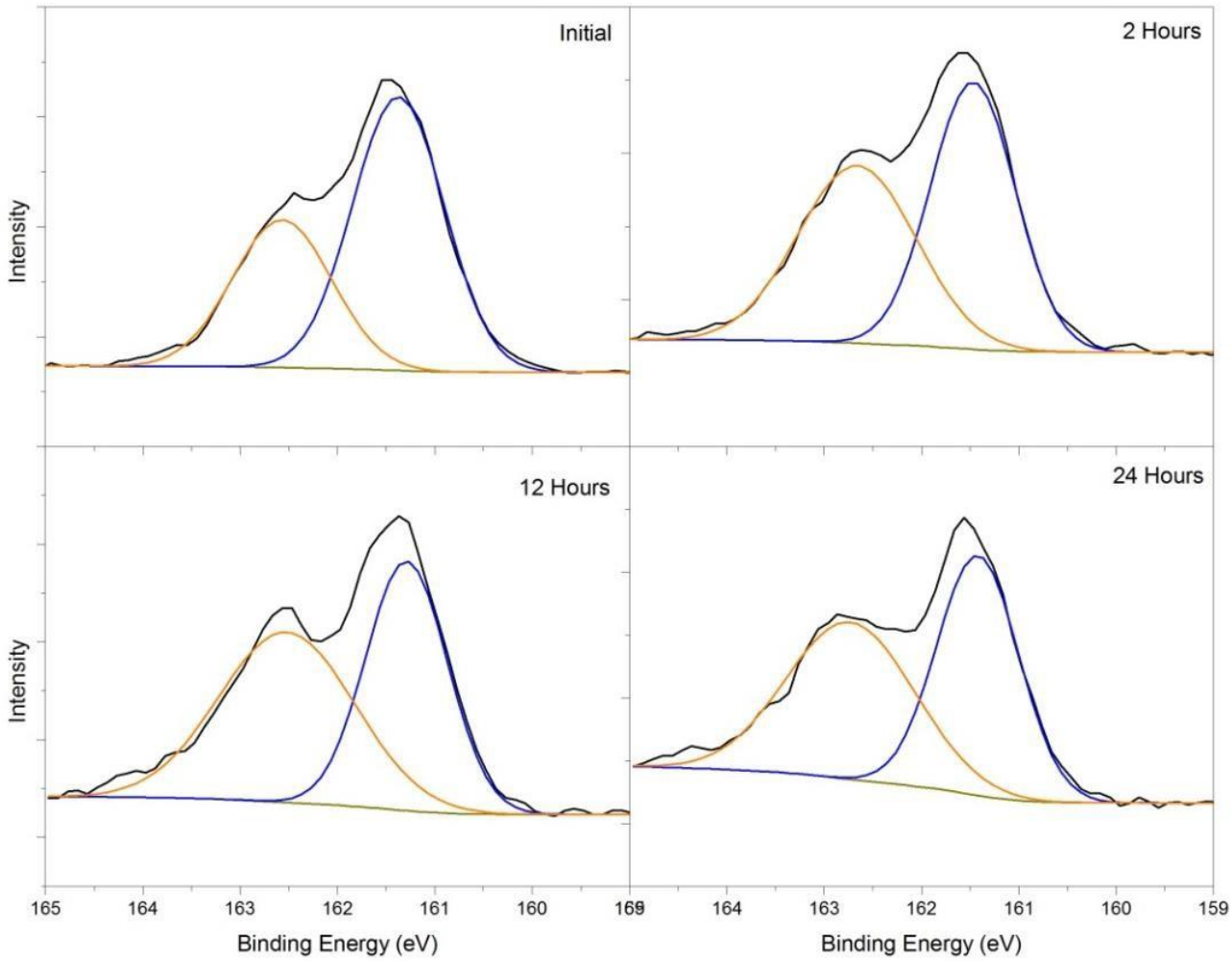

Figure S4.8: XPS spectra of the sulfur 2p energy range. The energy range is typical of an S^{2-} binding environment and shows minimal changes. The slight change in the ratio of the $p_{1/2}$ (orange) and $p_{3/2}$ (blue) peak areas is likely indicative of the formation of polysulfides.[5]

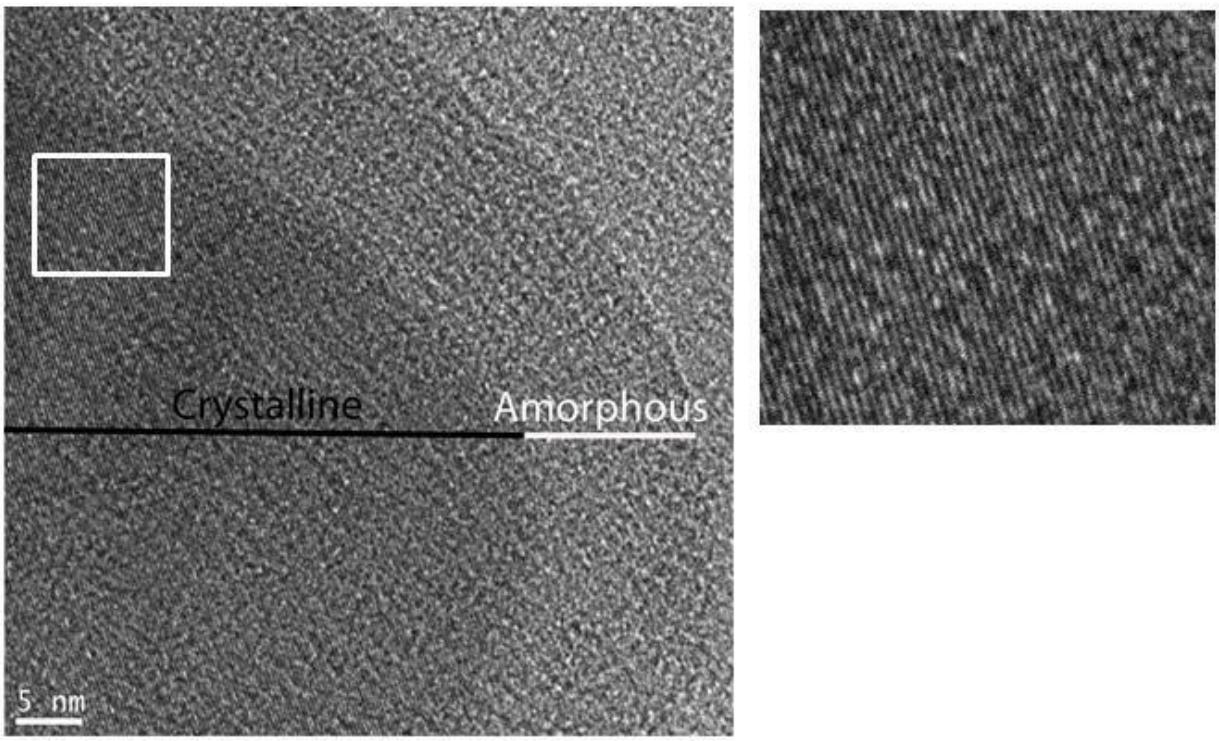

Figure S4.9: High resolution TEM micrograph showing an amorphous layer coating a nanocrystal. For clarity, a black line has been drawn to indicate the crystalline region and a white line is indicative of the amorphous region. The white box is drawn to indicate the portion of the figure that was magnified to show lattice fringes (right).

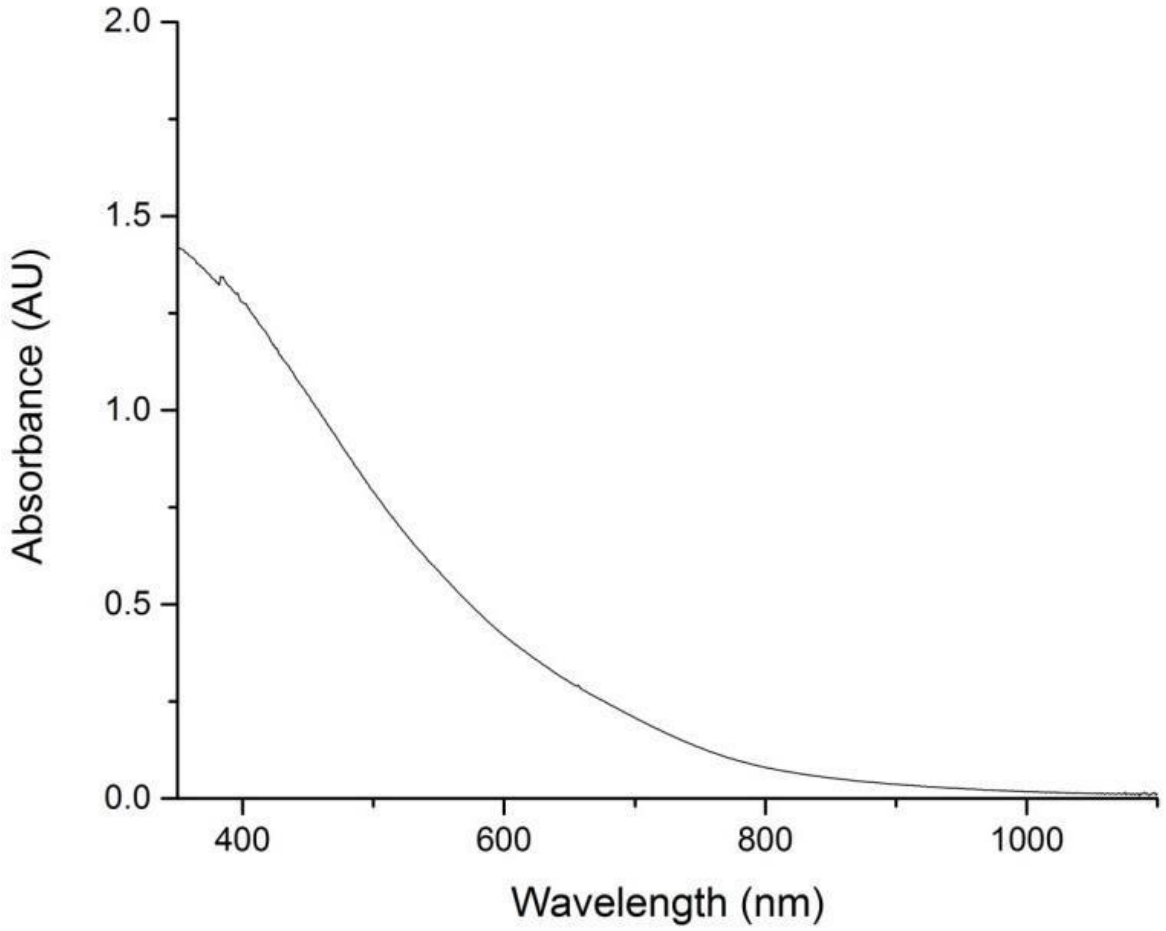

Figure S4.10: UV-Vis spectrum of suspended Fe_2GeS_4 nanocrystals. UV-Vis analysis on a suspension of nanocrystals did not show a clear onset of absorption. Neither a direct nor indirect band gap estimate was performed due to the gradual onset of absorption. The authors believe this could be due to a number of issues including the complications often associated with low lying Fe(II) electronic transitions, surface states present on these particles, and/or defects. Studies are underway to determine the nature of the defects and improve the optical properties.

Photoelectrochemical Data: In order to test the potential for its use in solar cells, a thin film of the Fe_2GeS_4 was prepared on FTO-coated glass. The layer-by-layer dip casting method was used.[96] The FTO-coated glass was dipped into solution of nanocrystals suspended in hexane and then into a solution of 5mg/mL of Na_2S in formamide. This solution has been demonstrated previously in the literature for solution ligand exchanges to remove the long chain, insulating ligands present on the surface of the particles as a result of the reaction conditions.[34] The thin

film was fabricated in a nitrogen glove box due to the high air sensitivity of the material. All photoelectrochemical materials were prepared before removing the film from the glovebox for PEC testing.

Photoelectrochemical tests were performed using a setup previously described.[95] In brief, an aqueous solution of $Eu(NO_3)_3$/KCl was thoroughly degassed with nitrogen. The reference and counter electrodes, Ag/AgCl and a Pt basket, respectively, were connected while the Fe_2GeS_4 film was still in the glove box. Immediately upon removal from the glovebox, the thin film was placed in solution as the working electrode. A ~ 17 mW green laser (532 nm) was used to produce photocurrent.

The photocurrent is small, but undeniably present in both a linear sweet from 0 to -0.5 V (figure S4.11) and also when the potential was held at -300 mV for several hundred seconds (figure S4.12). The film demonstrates p-type character as expected. The small photocurrent is not surprising considering the air sensitivity of the material and lack of optimization of the thin films (e.g. thickness, ligand exchange, annealing). Future studies are underway to probe photocurrent under an oxygen-free environment and determine optimal thin film fabrication.

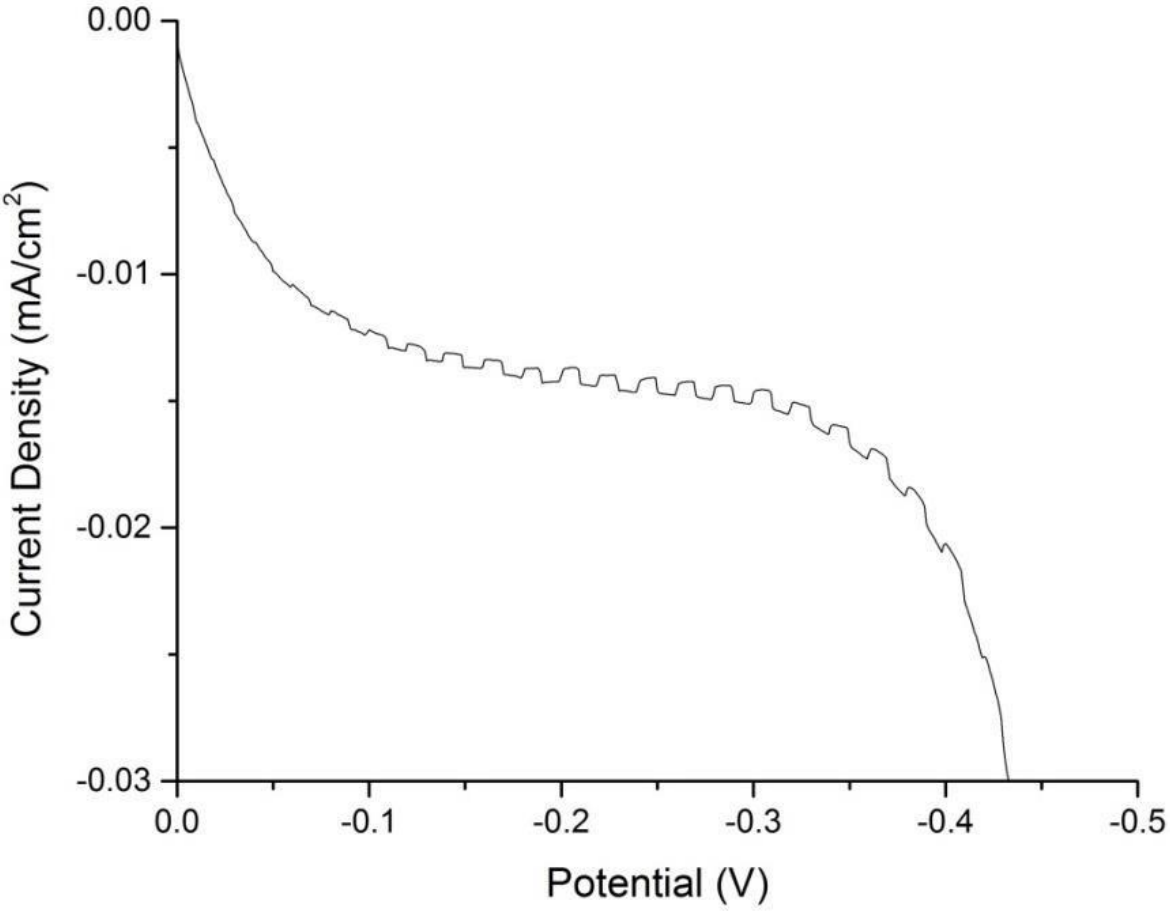

Figure S4.11: Photocurrent response in a linear sweep from 0 V to -0.5 V vs. Ag/AgCl.

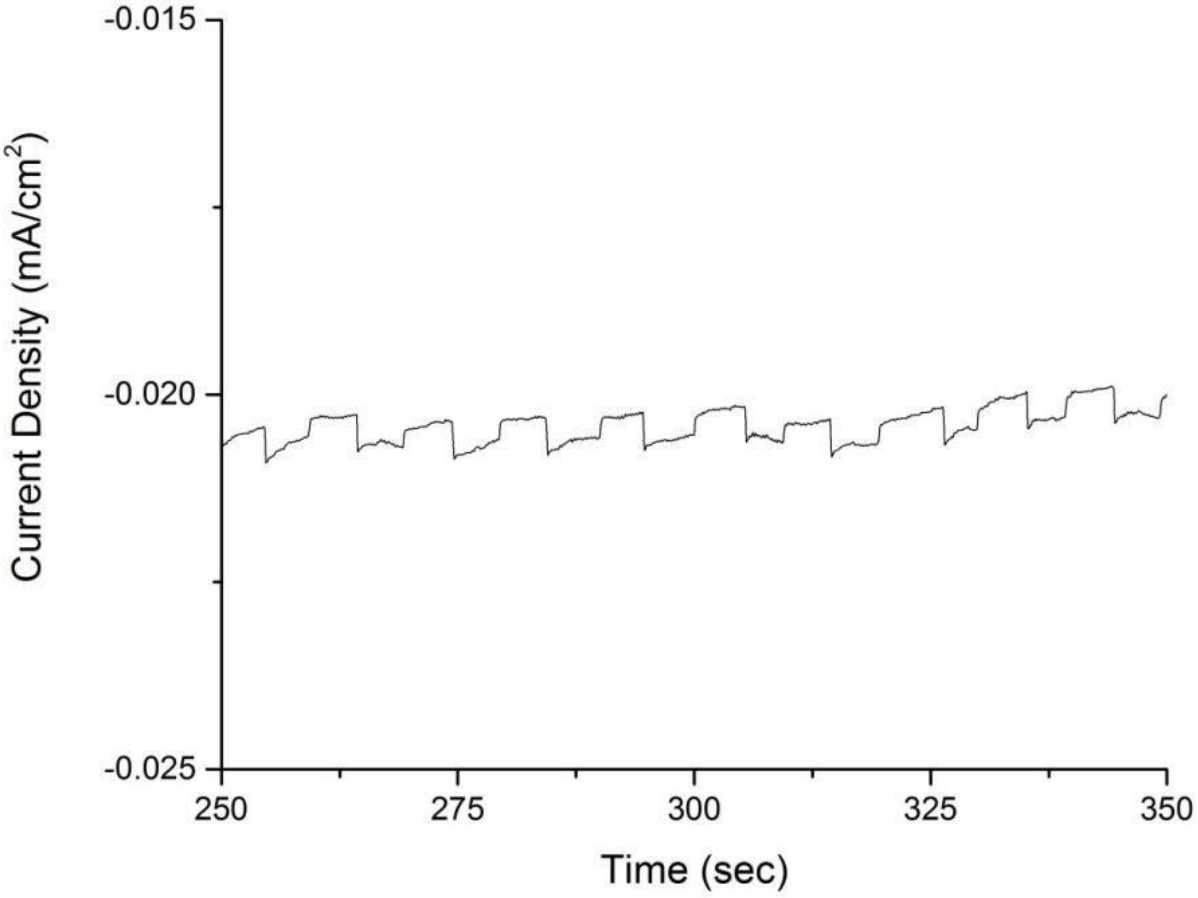

Figure S4.12: Photocurrent response in a chronoamperometry experiment where the potential was held at -300 mV vs Ag/AgCl.

Solution Ligand Exchange: Following a protocol by Nag *et al*,[34] a solution ligand exchange was performed to remove the HDA ligands and replace them with S^{-2} anions. All ligand exchange steps were performed in a nitrogen glove box with degassed and dried solvents. 25 mg of Na_2S was dissolved in 5 mL of formamide. 2 mL of this solution was placed in a vial and 2 mL of Fe_2GeS_4 nanocrystals suspended in hexane was added. The brown layer of nanocrystals was visible on top, while the Na_2S/formamide solution was completely clear on the bottom. This was stirred for a time and after ~ 30 minutes, the bottom layer had become brown as the nanocrystals migrated into the formamide solution while the top layer became clear. A small amount of nanocrystals seemed to precipitate out of the hexane solution and sit at the bottom of this layer, but not migrate completely into the formamide layer. The formamide layer was recovered for IR analysis.

A small amount of the Fe_2GeS_4 nanocrystals capped with Na_2S was dropped onto KBr plates for FTIR analysis. These plates were dried in a vacuum oven at 80 °C overnight to remove the formamide. Clean KBr plates were run as a background. Then the dried plates were analyzed. Finally, the nanocrystals in hexane capped with the native ligands were dropped onto clean KBr plates and analyzed. Analysis in Figure S8 shows evidence of a complete ligand exchange.

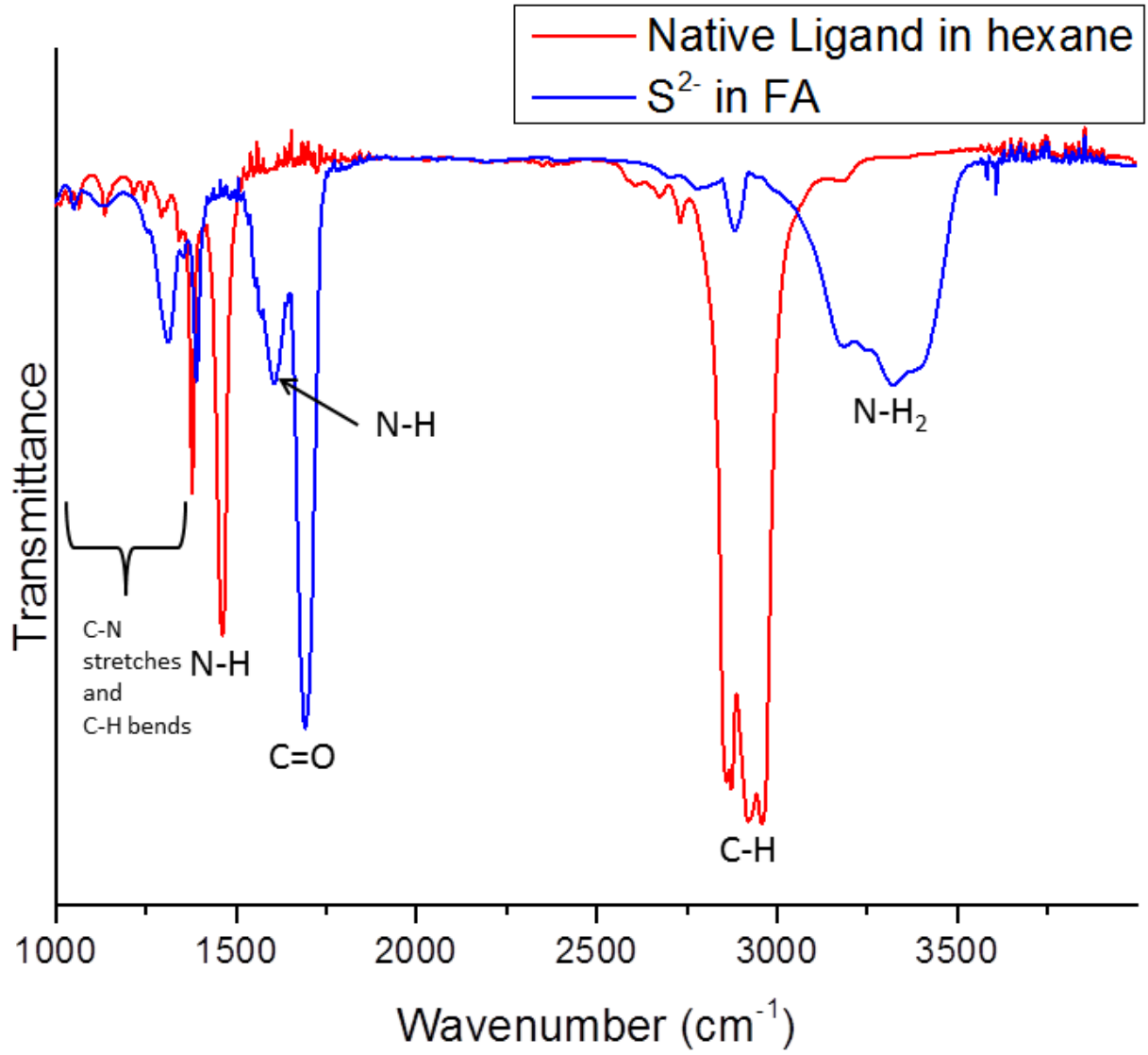

Figure S4.13: IR spectra of Fe_2GeS_4 nanocrystals with native HDA ligands (red) and after a ligand exchange (blue). All peaks post-ligand exchange can be identified as residual formamide. The large hydrocarbon stretch (3000 – 2800 cm^{-1}) has disappeared after the ligand exchange, leaving only a small peak in that region due to the C-H bond in formamide. This is indicative of a complete ligand exchange.

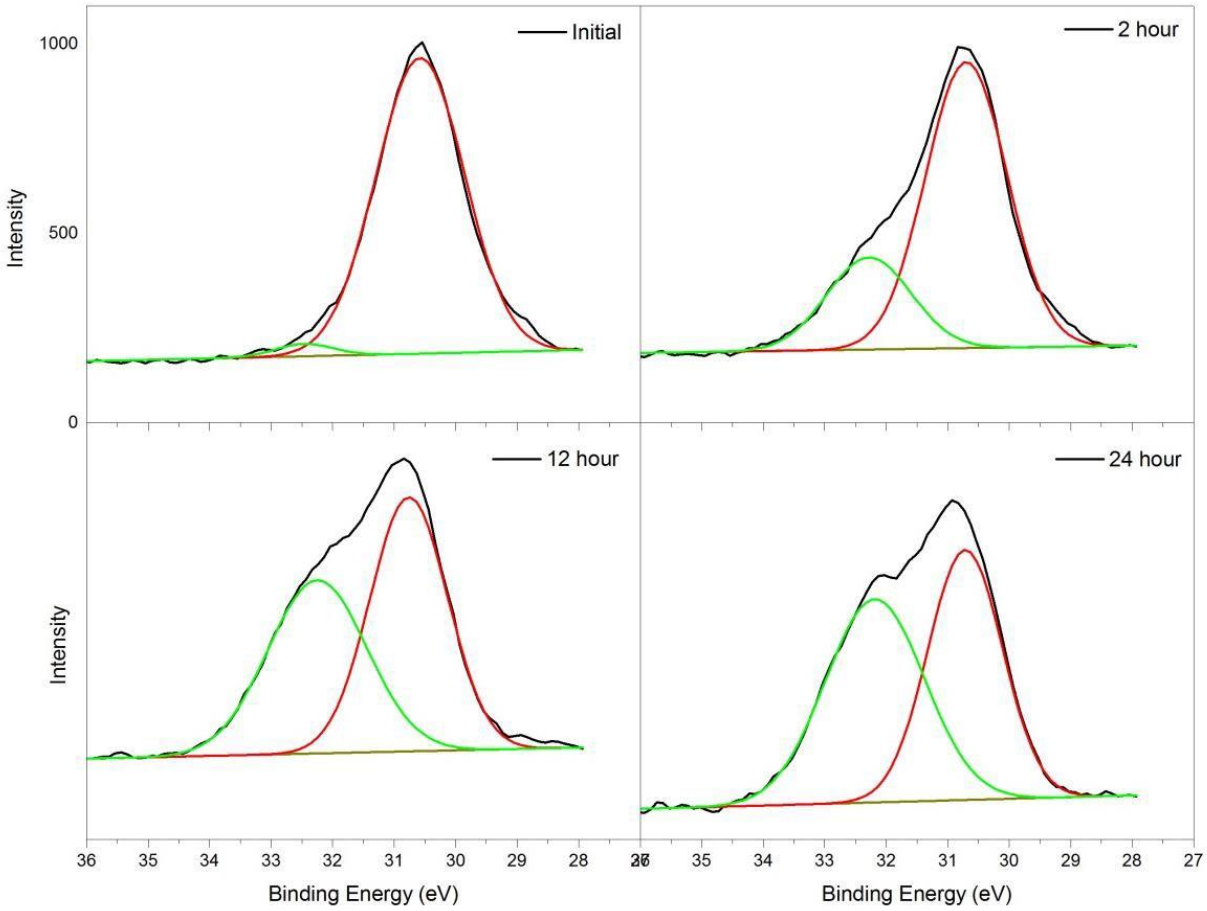

Figure S4.14: Germanium XPS spectra post-ligand exchange with sulfide. The black trace is the raw data. The red trace is the peak corresponding to the GeS_2 binding environment and green trace is for the GeO_2 binding environment.

CHAPTER 5: THE TOOLBOX FOR CHARACTERIZING KESTERITE NANOCRYSTALS AND POTENTIAL IMPURITY PHASES

The following chapter is the result of hard work from a variety of individuals working to solve a complex problem over many years. Initial work on the synthesis and characterization of CZTS nanocrystals was pioneered by Shannon C. Riha. Experimental work including synthesis and characterization of CZTS and reaction components was performed by Sarah J. Fredrick, Garrett Wheeler, Laura M. Wally, and Patrick Riening. Daniel Agocs assisted with literature research and manuscript preparation, specifically for the section discussion Raman spectroscopy. Sarah J. Fredrick prepared the manuscript. Laura M. Wally, Daniel Agocs and Amy L. Prieto assisted in manuscript editing.

5.1 Introduction:

Although the sun provides 160,000 TW of harvestable energy,[5] the amount of energy harvested by solar technologies is strikingly low. Solar energy accounted for less than 2 % of the non-hydroelectric renewable energy consumed in the United States in 2013, while renewables overall made up only 13 % of total US energy consumption.[121] The major reason for solar power's low contribution to the overall energy economy is the high upfront cost for the solar panels themselves; therefore a main goal of solar research is to drive the cost of photovoltaic technologies down.

Silicon solar cells still comprise ~80% of the total solar market in the United States.[6] Although silicon has many advantages like its earth abundance and the long history of research, development and manufacturing, it is not an optimal solar material. Its indirect band gap requires that a thick film (on the order of several hundred microns) be used in order to absorb the majority of incoming radiation.[9] Second generation thin film solar cells provide a reasonable alternative to

silicon because of their direct band gaps and high absorption coefficients, allowing for thinner absorber layers and ultimately less material usage.[11] Thin film materials like CdTe, and $Cu(In,Ga)(S,Se)_2$ have already achieved reasonable efficiencies (both now at 21 %),[38] but are limited due to the scarcity and high cost of tellurium, indium and gallium.[122] Additionally, the toxicity of cadmium is a concern,[123] so finding alternatives with non-toxic, abundant elements is key for long-term, large-scale use. One promising alternative that as emerged in recent years is Cu_2ZnSnS_4 (CZTS), because of its non-toxic, earth abundant constituents. Additionally, it has optimal properties with a band gap ranging from 1.0 to 1.5 eV, depending on the chalcogenide content,[124] and a high absorption coefficient of 1×10^4 cm^{-1} making it an excellent solar cell candidate.[122,125,126] Although research on CZTS is relatively new compared to materials like CdTe and CIGS, laboratory efficiencies have already reached an impressive 12 %, with the record efficiency improving on a regular basis.[127] With such promise, it's not surprising that research on CZTS has exploded in the last decade.

One area of CZTS research that has garnered much attention in recent years is that of nanocrystal synthesis. Nanocrystal inks have been established as a promising alternative to the traditional high temperature vacuum depositions of thin film solar cells.[19] These colloidal solutions have the advantage of room temperature processing to make films via drop or dip – casting, ink-jet printing, spray painting and various other methods. The combination of a low-temperature synthesis of nanocrystals and ambient processing could dramatically reduce the overall cost of solar cells, and thus bring cost-competitive solar technology closer to a market reality. These factors have encouraged a large number of publications related to CZTS nanocrystals in the past several years. In fact, since 2009 when the first reports of the synthesis of CZTS nanocrystals were published, the number of publications on the subject has increased steadily and rapidly, as demonstrated in detail in Figure 5.1. In 2009, only a

handful of publications on the topic were reported, but by 2013, the number of publications reached almost 150 in just one year.

In the summer of 2009, there were three reports published in *The Journal of the American Chemical Society* on the synthesis of CZTS nanocrystals.[95,128,129] These first syntheses of CZTS nanocrystals were slightly different, but all appeared to have made stoichiometric CZTS

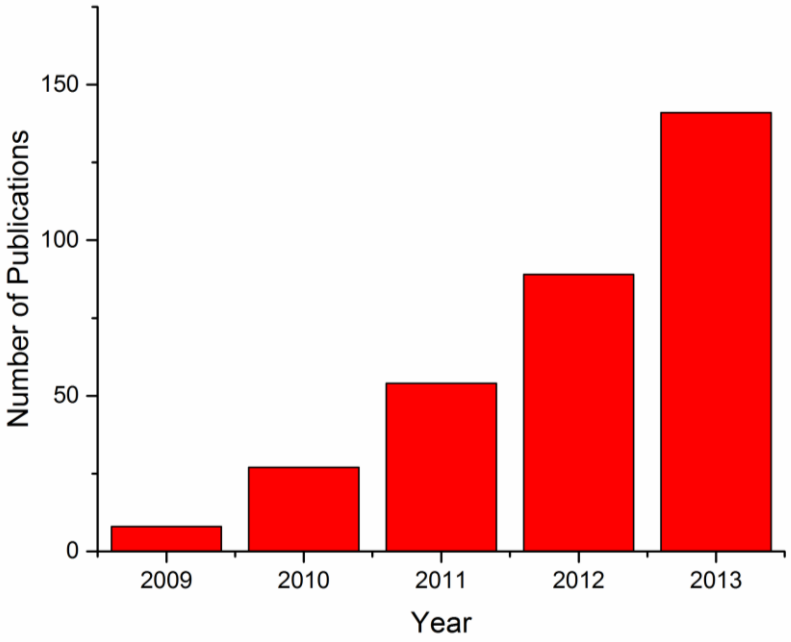

Figure 5.1: The number of results in a SciFinder search using the terms "CZTS" or "kesterite" and "nano" for each year from 2009 – 2013.

nanocrystals. Since then, there have been hundreds of reports on the synthesis and further utilization of CZTS nanocrystals for solar energy applications. Reports on bulk systems have studied the intricate details of the kesterite structure and the theoretically and experimentally determined possible defects in the crystal system.[130-137] Understanding these defects has been imperative for work on CZTS considering slightly off-stoichiometry materials (copper deficient and zinc rich)[95,138,139] are those have consistently achieved the highest efficiency devices.[127,140-142] Some have sought to examine the effects of a varied Cu/Zn ratio on electronic, optical and PV performance,[138,139] and this claim has even been debated in recent work.[143] In stoichiometric bulk

materials, neutron and high energy x-ray diffraction experiments have shown that the kesterite structure of CZTS is highly disordered, especially in terms of the Cu and Zn sites in the lattice.[144-146] This disorder is even more exaggerated in nanocrystal systems. There has been one report attempting to elucidate the nature of this disorder in CZTS nanocrystals. It was shown that the disorder is not localized within a unit cell (i.e. Cu_{Zn} and/or Zn_{Cu}), but extends over nanoscale domains, leading to regions of significant chemical inhomogeneities within a single nanocrystal. [manuscript under review] As work on CZTS progresses and our knowledge of the material expands, the structure is only becoming more complicated. Controlled doping with sodium has shown better performance than undoped materials.[147-150] Theoretical work has suggested that in addition to controlling the S:Se ratio to tune optical and electronic properties, a whole host of cations can be substituted into the lattice to design materials rationally for specific properties.[151]

In addition to disorder on the atomic level, CZTS has the potential to form many impurity phases in the synthesis. Because CZTS is a quaternary (or quinary when alloyed with Se) system, obtaining stoichiometric CZTS with no impurity phases can be challenging. Even in bulk systems, impurities can be present. This is largely due to the small composition allowed by the phase diagram where phase-pure CZTS exists.[152] It is thermodynamically favorable to have a mixture of phases under a variety of conditions. This has been observed experimentally in a many cases. A common impurity in films annealed in Se vapor is ZnSe, which tends to form at the back contact.[153-155] Other reports have shown that, similarly, ZnS (as well as $Cu_xSn_yS_z$ and SnS)[156] can be found in "pure" CZTS devices.[157,158] The amount of ZnS present in a film has been correlated to a decrease in PV performance, so identifying impurity phases and reducing their presence is an important task for those working on CZTS.[157,158] However, it is not at all straightforward to identify secondary phases such as ZnS. The aforementioned publications have

used techniques such as atom probe tomography,[155] cathode luminescence,[156] and XANES,[158] techniques not readily available in most laboratories.

Identifying impurity phases is exceedingly important when characterizing nanocrystals, which have a high degree of disorder. Since colloidal syntheses allow for kinetic control over which phases form, it is not always obvious which phase(s) should form under certain conditions. Great care must be taken to analyze nanocrystals thoroughly so that the composition of the nanocrystals is well-understood. With device performance continually increasing, it is vital that researchers are able to link composition with performance and controllably tune materials for optimal devices. Work towards making high efficiency nanocrystal PV devices has demonstrated that low temperature synthesis and device fabrication is possible, as these materials have reached impressive efficiencies above 8 %.[159]

Understanding specific defects and rationally controlling them in this complex material is imperative for future improvements in photovoltaic properties. This work seeks to examine the current state of the literature on CZTS nanocrystals and establish common practices for accurately characterizing the material. It does not seek to be an exhaustive review of CZTS literature, as several other reports have been published on this subject,[140,160-163] but rather focuses specifically on nanocrystal synthesis. The paper will first give an overview of the different types of nanocrystal syntheses that have been performed thus far. It will then give a detailed account of *commonly used* characterization techniques in order of their prevalence in literature on CZTS and analyze each technique for its role in determining nanocrystal purity. We will then present example cases from our own research of CZTS syntheses to demonstrate the need for thorough analysis. Finally, a future outlook will be given in an attempt to guide new work on CZTS and related materials.

5.2 Nanocrystal Synthesis Background:

CZTS: The three original kesterite CZTS syntheses were reported as *JACS* Communications that were all published in the summer of 2009. Guo and coworkers performed a hot injection of sulfur in oleylamine into a hot solution of metal acetylacetonates in oleylamine.[129] Riha and coworkers presented a dual hot injection of metal salts and sulfur, separately dissolved in oleylamine, into hot trioctylphosphine oxide.[164] Steinhagen and coworkers presented a simple arrested precipitation method in which metal salts and elemental sulfur were heated in oleylamine.[128] All three papers employed x-ray diffraction, EDS, TEM and UV-Vis to determine nanocrystal purity. Riha and coworkers additionally included XPS and DTA to support claims of phase purity. Oleylamine is a common thread in these three reactions and is used in many others. It is useful because of its ability to form reactive complexes with precursors, act as a capping ligand, aid in size and shape control, and to tune the electrochemistry of the solution due to its reducing nature.[69,165-170] Although these first three papers were short communications, some further study was performed on these CZTS syntheses in later publications. A more detailed study of the hot injection synthesis presented by Riha and coworkers experimentally demonstrated that varying the Cu:Zn ratio can produce higher efficiency materials. They also demonstrated dramatic improvements in efficiencies after a short annealing step at 350°C.[95] Additionally Guo *et al* showed that their original CZTS nanocrystals could be annealed in Se vapor to produce a 7.2 % efficient solar cell.[171] Since then, many adaptations on this synthesis have been presented and the work on CZTS has expanded dramatically. Some recent work will be highlighted herein, but it is not intended to be a complete list of CZTS syntheses. It only serves to give examples of recent developments.

New one pot heat-up methods have been demonstrated. A report by Li and coworkers shows a synthesis in oleylamine very similar to the original Steinhagen report, but with different

metal salts.[172] Chesman and coworkers demonstrate the use of a novel zinc precursor for these reaction types, zinc ethyl xanthate, in a heat up with oleylamine and dodecanethiol.[173] Since the reactivity of zinc has proven to be difficult in these reactions,[69] new precursors can be useful. Chesman and corworkers also demonstrated a heat-up reaction in which reacted carbon disulfide was added to OLA and DDT to create oleyldithiocarbamate and dodecyltrithiocarbonate as ligands and sulfur precursors.[174] They achieved gram scale products with purity proven with extensive characterization. Although there have been few other demonstrations of the hot injection to make pure CZTS, excluding those that also incorporate Se, in one report, Li and coworkers inject metal salts into sulfur, but use octadecylamine as opposed to oleylamine as the solvent in the solution.[175] Rather than a traditional hot injection in which metal or sulfur precursors (or both) are injected into a hot surfactant, oleylamine can be injected into a hot precursor solution to decompose precursors into CZTS as a final product.[176,177] Examples of hydrothermal syntheses have been reported, and can result in a wide variety of nanocrystal sizes and shapes.[178-180] Microwave-assisted syntheses have also been utilized in the formation of CZTS, however these samples had to be annealed in order to obtain crystalline CZTS.[181,182] Examples of quantum-confined CZTS nanocrystals with band gap tunability have been made by a hydrothermal method[179] and also using OLA to assist in the decomposition of diethyl dithiocarbamate complexes.[183] And recently, an aqueous synthesis of CZTS nanocrystals was demonstrated.[184] Nanowires are also of interest for solar cell applications and there have been reports of CZTS and CZTSe template nanowires, but no data demonstrating their photoresponse has been reported.[185-187]

CZTSe: After the initial interest in the synthesis of CZTS nanocrystals, CZTSe research quickly followed. There are discrepancies in the reported band gap of CZTSe,[188] but with the theoretical band gap of ~1.0 eV,[124] the promise of alloying or mixing CZTS and CZTSe to tune

the band gap has driven research on both compounds. There have been several examples of the synthesis of CZTSe by an arrested precipitation method[189] and hot injection.[190,191] Most reports regarding CZTSe, however, are working to incorporate an alloy of the sulfide and selenide.

*CZT(S,Se):*Efforts have been made toward achieving a mixed chalcogenide, alloying the sulfide and selenide to tune the band gap, and also perhaps the conductivity of the material.[192] This is not a trivial matter due to the difference in reactivity of sulfide and selenide precursors, which has been studied in binary systems such as Cd(S,Se)[71] and Pb(S,Se).[72] Riha and coworkers showed they could incorporate Se into the original CZTS structure using the same hot injection method,[164] but they had to use a reducing agent, sodium borohydride, to balance the reactivity of the sulfur and selenium.[192] Rath and coworkers present a detailed discussion of their own study of the precursors involved in their injection synthesis, also oleylamine-based. They find vastly different precursor kinetics when targeting the sulfide and selenide products.[69] Finally, Ou and coworkers show that using thiourea and selenium, rather than sulfur and selenium, is also a potential route to making the mixed chalcogenide phase.[193]

Wurtzite: Recent literature has demonstrated an interest in the metastable wurtzite phase of CZTS. Fan and coworkers demonstrated both theoretically and experimentally that the wurtzite phase may be advantageous to pursue because the mixed chalcogenide has a lower formation enthalpy than in the kesterite phase.[194] This could allow for easier tunability with respect to the chalcogenide content. The wurtzite structure is not, however, the focus of this paper, but references on the subject are included here. [194-203]

The vast number of recent synthesis methods for nanocrystals of the CZTS family of compounds demonstrates the excitement and promise of this material as a solar absorber. However, it is difficult to compare performance between different syntheses because the nanocrystals are not typically characterized in a thorough manner. There are few reports of full

solar cell devices being built from CZTS nanocrystals, but even more troubling is the lack of basic material characterization in current CZTS literature. It is a complex material and even determining the phase that one has synthesized is a non-trivial matter. As research continues to move forward in this field, it is important that the reports are detailed in their characterization and analysis so that progress may be made toward higher quality, more efficient materials.

5.3 Experimental/Results/Discussion:

In this section, the authors will explain and evaluate characterization techniques commonly used in the analysis of CZTS nanocrystals. Each technique will be evaluated for what information it can give about the material, and specific attention will be paid to how effective each technique is at determining if any impurity phases are present. Since, as previously stated, impurities can have dramatic effects on material properties and device performance, identifying these impurities is important. In order to present not just an explanation, but a useful example, the authors have synthesized CZTS, CTS and ZnS and will analyze all of these materials, in addition to a random mixture of the three, to demonstrate the difficulty of identifying differences between these related phases. A preparation from the Korgel group will be used as it has been widely reported in the literature since its initial publication.[128] A literature preparation for CTS and ZnS was also drawn from the CZTS literature in a report from Cao and coworkers, in which nanoparticles of these compositions were annealed to make CZTSSe films.[204] The ordering of the data is loosely based on the frequency of occurrence in CZTS literature (e.g. XRD will be presented first because it is the primary method of determining the phase of the product in CZTS syntheses). Conclusions will be drawn regarding the effectiveness of each technique in detecting potential impurities, in addition to highlighting the usefulness of each technique for giving valuable information about the material.

Materials and Methods: The following were purchased in the highest purity available from Sigma Aldrich and used without further purification: copper (II) acetylacetonate ($Cu(acac)_2$), copper (I) chloride (CuCl), zinc (II) acetate ($Zn(OAc)_2$), zinc chloride ($ZnCl_2$), tin(IV) chloride pentahydrate ($SnCl_4 \cdot 5H_2O$) tin (II) chloride dehydrate ($SnCl_2 \cdot 2H_2O$), sulfur powder (S), and trioctylphosphine oxide (TOPO). Oleylamine (70 %) was purchased from Sigma Aldrich and sparged with Ar prior to use. ACS grade hexanes, ACS grade toluene, ACS grade ethanol and technical grade methanol were purchased from Fisher and used as-received for nanocrystal purification. All syntheses were performed with air-free techniques in a nitrogen glovebox and an argon Schlenk line unless otherwise specified. Nanocrystal purification and characterization was done in air.

X-ray diffraction was performed on a Scintag X-2 Advanced Diffraction system equipped with Cu Kα radiation (λ = 1.54 Å) using solid samples drop cast from either hexane or ethanol onto a zero background SiO_2 sample holder. SEM imaging and EDS analysis was performed using a JEOL JSM 7000F FE-SEM equipped with an EDAX energy dispersive spectroscopy detector. Images were acquired with a working voltage of 15 kV and a working distance of 10 mm. Elemental composition data was obtained using Noran System Six (NSS) software. TEM images were obtained using a JEOL JEM-1400 TEM at a working voltage of 100 kV. UV-Vis spectra were obtained on an Agilent 8453 UV-Vis ChemStation spectrophotometer with dispersions of nanocrystals in hexanes. XPS was performed on dry powders prepared on carbon tape. XPS spectra were obtained using a Physical Electronics ESCA 5800 system with monochromatic Al Kα (E = 1486.6 eV) as the x-ray source. High resolution scans were performed with a pass energy of 23.5 eV and a step size of 0.10 eV/step. Data analysis was performed using Multipak software version 9.3.03. All spectra were shifted to account for charging, using inorganic carbon as a reference at 284.80 eV.

Synthesis of CZTS: CZTS was synthesized following a protocol by Steinhagen and coworkers.[128] In brief, 0.52 (2 mmol) of $Cu(acac)_2$, 0.29 g (1.6 mmol) of Zn(OAc)2, 0.18 g (0.8 mmol) of $SnCl_2 \bullet 2H_2O$, 0.13 g (4.0 mmol) and 40 mL of OLA were added to a 100 mL 3-neck round bottom flask equipped with a stir bar and thermocouple. The solution was degassed at room temperature under vacuum for 2 hours. The reaction mixture was then purged with Ar (or N_2) at 110 °C by bubbling the gas through the solution. It was then heated to 280 °C and left for one hour. The solution was cooled naturally to room temperature. The solid was isolated by precipitation with ethanol and centrifugation and the supernatant was discarded. The product was dispersed in hexanes and then precipitated again with ethanol. This process was repeated a total of three times. The final dispersion in hexane was centrifuged to remove agglomerates and the suspended particles were stored for further analysis.

Synthesis of CTS: Copper tin sulfide (CTS) was made following a protocol by Cao and coworkers. [204] The following were mixed in a 50 mL round bottom flask equipped with a thermocouple and stir bar: 0.19 g CuCl, 0.351 g $SnCl_4 \bullet 5H_2O$, 7.5 mL of OLA, and 2.320 g of TOPO. A scintillation vial was loaded with 0.096 g of S and 1.5 mL of OLA and sealed with a rubber septum. The S/OLA solution was sonicated at ~80 °C to dissolve all solids. The round bottom flask was heated under vacuum to 130 °C and left for one hour. It was then switched to Ar pressure and heated to 260 °C and the sulfur solution was rapidly injected. This was left for three minutes, then the heating mantel was removed and the solution allowed to cool to room temperature. The product was purified by the same method used for CZTS.

Synthesis of ZnS: Zinc sulfide was synthesized from the same literature reference as CTS. [204] The following were mixed in a 50 mL round bottom flask equipped with a thermocouple and stir bar: 0.273 g of $ZnCl_2$, 2.327 g of TOPO and 7 mL of OLA. Then 0.077 g of sulfur and 1.5

mL of OLA were mixed in a scintillation vial and sonicated to dissolve all solids. The round bottom flask was heated to 170 °C under vacuum and left for 30 minutes. The flask was then switched to Ar pressure and the sulfur was injected. This was heated to 320 °C and left for one hour. The heating mantel was then removed and the solution was allowed to cool to room temperature. Because of potential oxidation concerns, these particles were purified in a nitrogen glove box by the same procedure as for that of CZTS and CTS. The solid was stored in the glove box for further analysis. *X-Ray Diffraction*: X-ray diffraction (XRD) is the most commonly used technique for identifying crystalline phases in the CZTS system. It is a powerful and non-destructive technique for solid state samples, and it is an important first step to determining phase purity in CZTS samples. This material forms in a tetragonal crystal system. It can exist as either stannite or kesterite,[144] and recently many have shown that the metastable wurtzite phase can also be synthesized in nanocrystalline form.[172,194-197,199,200] The focus of this paper will be the kesterite system due to its prevalence in the current literature, especially for use as a photovoltaic material. The kesterite structure of CZTS has diffraction peaks of (112) at 28.53°, (200) at 32.99°, (211) at 37.97°, (220) at 47.33°, (312) at 56.18°, (224) at 58.97° and (332) at 76.44°(PDF 00-075-4122).[205] These also closely correspond to the same peaks for both tetragonal copper tin sulfide (PDF 01-089-2877) and cubic zinc sulfide (PDF 03-065-0309).[205] And although copper sulfide can exist in many phases, most of which would be able to be distinguished via XRD, there is one phase, digenite, that has good overlap with the CZTS pattern (PDF 01-076-6653).[205] There have been many reports on the synthesis of copper sulfide nanostructures of many phases,[206] (see paper by Lotifpour, *et al*. for a list of copper sulfide references) but the authors are not aware of any reports of this particular

digenite phase being synthesized as a nanocrystal. For the purposes of this publication, we will make the assumption that copper sulfide phases can be distinguished using X-ray diffraction.

Tin sulfides are another potential impurity phase that can be readily identified via XRD. There are a wide variety of crystalline phases that can be present, but none exhibit clear overlap with CZTS. Structural characterization of these materials can be found elsewhere[207-210] but it is reasonable to assume that if there are no extra peaks in the diffraction pattern, tin sulfides are not present. For the purpose of this paper, tin and copper sulfides will not be discussed in terms of further characterization because XRD is a sufficient tool for ruling out these impurities. One other drawback to using XRD to demonstrate purity is that it does not give any useful information about amorphous phases that may be present. At the temperatures at which these reactions are performed, amorphous phases are uncommon, but they are possible. Therefore, XRD can be useful for ruling out copper and tin sulfides as impurity phases, but even with a clean XRD pattern that corresponds well to the CZTS crystal structure, CTS, ZnS and amorphous phases could still be present.

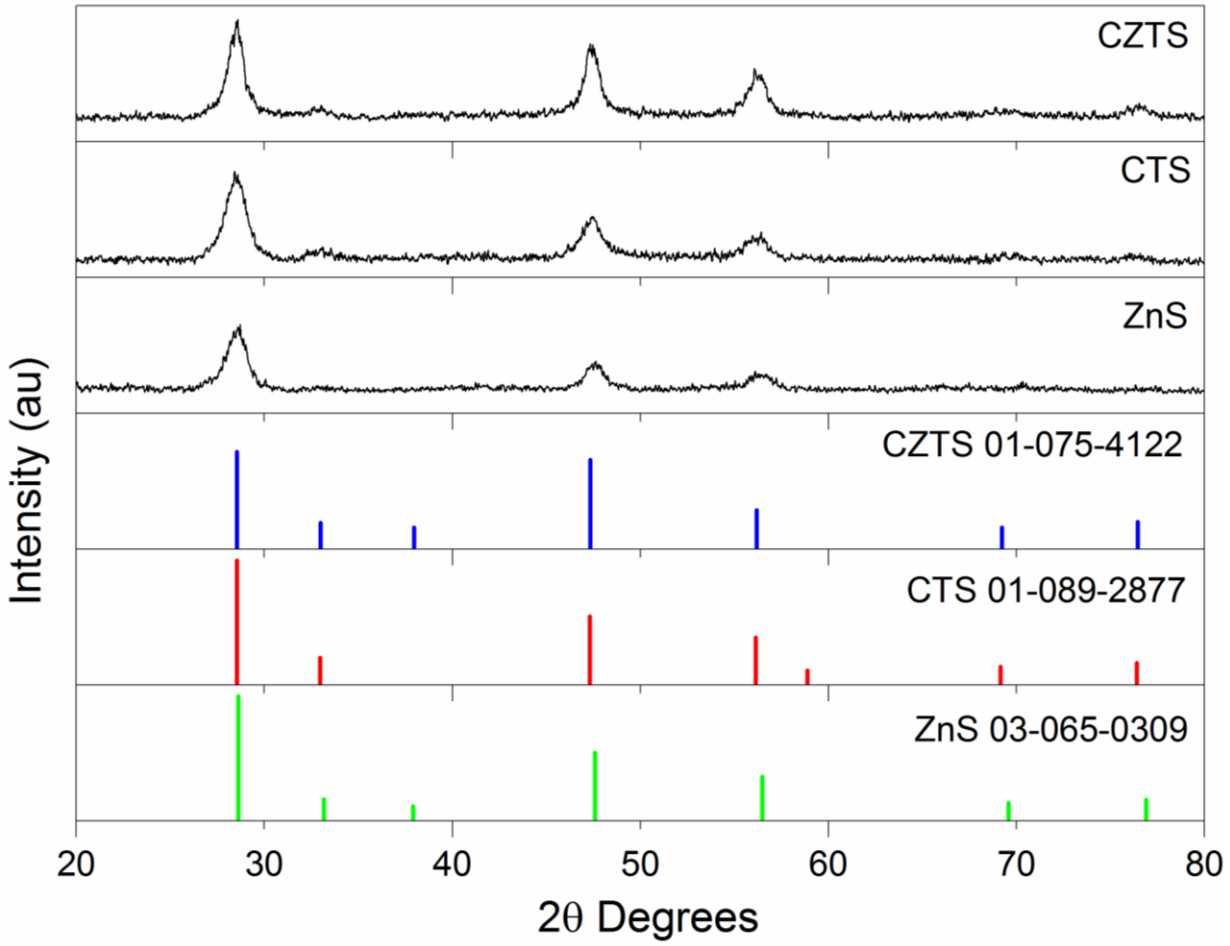

Figure 5.1: X-ray diffraction patterns for (from top to bottom) CZTS CTS, and ZnS. References for ZnS, CTS and CZTS are plotted for comparison with corresponding PDF values from the ICSD (reference 205).

To demonstrate the difficulty in discerning these phases via XRD, three separate samples were analyzed: CZTS, CTS and ZnS. As can be noted in Figure 5.1, the diffraction patterns of all samples look nearly identical. In samples such as these where the nanocrystals are quite small, peak broadening occurs in XRD and can make peaks more difficult to resolve. However, this peak broadening can be a useful measure of the crystallite size using the Scherrer or Williamson-Hall methods. So although XRD is an incredibly useful for determining if the kesterite phase may be present, it cannot be used on its own as definitive evidence that it is a phase-pure sample.

Scanning Electron Microscopy with Energy Dispersive X-Ray Spectroscopy: When characterizing CZTS nanocrystals, scanning electron microscopy (SEM) can be used to determine the morphology of thin films fabricated from nanocrystal suspensions, but is more commonly used in conjunction with energy dispersive X-ray spectroscopy (EDS) to investigate elemental composition. EDS can be used to determine average elemental composition over a given area and is reported in terms of atomic percentages. An average stoichiometry can then be calculated and reported. When using standards for each element of interest during each analysis, an accuracy of 1 – 2 % can be achieved,[211] however standardless analysis is now common. The authors are not aware of any CZTS nanocrystal publications in which standards are used for EDS analysis. This is not surprising considering analysis with standards would be tedious for CZTS, requiring all four elements to be standardized. For standardless analysis, the error can be as high as 20 %,[211] so this should not be used in a quantitative manner (see the following section on other methods for elemental analysis). Many reports also do not state that the data were taken from many spots on a given sample, but rather report one value for elemental composition, which is likely not representative of the entire sample. Since EDS is only an average composition at one small portion of a sample (the area being analyzed at a given time via SEM), many different areas should be analyzed to obtain precise, representative results. There have been reports of chemical inhomogeneities in both bulk CZTS films and nanocrystals,[155,189,212] indicating that thorough analysis requires many areas of a sample to be analyzed via EDS.

Analysis of multiple spots on a sample is one useful way to get information from SEM analysis. If there are glaring discrepancies in the data from one spot to another, it can point to these possible inhomogeneities. It could also point to a mixture of phases being present in one sample.

However, it is still true that the error in these analyses can be up to 20 %, so the data can be taken only to suggest certain qualities in the material, but not be concrete evidence for them.

One major absence in the discussion of CZTS composition as reported by EDS is that there has been no mention of what the appropriate range of elemental composition should be for CZTS. In order to determine these values, one must consult calculated phase diagrams for the CuS-ZnS-SnS system.[152] There is a very limited range of compositions that are classified as pure CZTS without any binary or ternary phases included. Considering the high error associated with EDS measurements it is difficult to draw specific conclusions. EDS should be used as a tool to look for glaring problems in a sample (e.g. extremely low or high elemental ratios), but not as a quantitative method for determining composition.

SEM/EDS analysis was performed on all samples in order to estimate the elemental composition. Samples were analyzed on at least six different locations in order to look for chemical inhomogeneities. To demonstrate the importance of obtaining data from multiple spots on a sample, a mixture of phases was analyzed using EDS. Table 5.1 shows the results from

Spot #	**1**	**2**	**3**	**4**	**5**	**6**
Cu at%	25.9	15.6	36.3	22.1	24.5	20.8
Zn at%	23.2	33.8	32.8	24.2	17.2	28.0
Sn at%	10.1	6.3	6.2	9.6	11.5	8.3
S at%	40.7	44.3	24.3	11.5	46.7	42.9

Table 5.1: EDS values of atomic percentages of each element at ten different spots on a sample composed of a mixture of CZTS, ZnS and CTS.

a sample containing an arbitrary mixture of CZTS, CTS and ZnS. These values vary greatly, which is not unexpected with a mixture of phases. However, we have seen similar results at times for stoichiometric CZTS samples. We have observed that a recurring problem with our EDS spectrometer is low values for sulfur content. This is common when using spectrometers

that are not regularly calibrated. We have therefore concluded that this cannot be an accurate measure of composition. If accurate compositional data is required, one should analyze samples by ICP techniques. SEM/EDS can, however, be quite useful for determining if samples are close to the expected range for elemental composition.

Other Techniques for Compositional Analysis: In addition to EDS, compositional analysis can be performed by inductively coupled plasma paired with either absorption or emission spectroscopy or mass spectrometry (ICP-AES, ICP-OES or ICP-MS). ICP techniques are more accurate than EDS and do not require the use of standards for analysis. Although this is a commonly used method for quantitative analysis of many different types of samples, the use of this technique has rarely been demonstrated with CZTS nanocrystals, likely due to difficulty in digesting the samples in acid. Other methods such as neutron activation analysis (NAA), X-ray fluorescence (XRF), and proton induced X-ray emission (PIXE) can be used for elemental analysis, but are specialized techniques that are not typically available for routine analyses.

TEM (with EDS and/or EELS): The third characterization method that is present in nearly all publications on the synthesis of CZTS nanocrystals is transmission electron microscopy (TEM). This method is useful for analyzing the size and morphology of synthesized nanocrystals. It can be paired with energy EDS or electron energy loss spectroscopy (EELS). EDS can be used for compositional analysis in a TEM similar to being used in a SEM instrument. When attempting to use this data in a quantitative manner, the same considerations regarding careful analysis with standards must be taken (see SEM/EDS section). Careful calculations may be performed in order to make quantitative comparisons in terms of elemental ratios, but parameters such as sample thickness and collection efficiency must be

known.[213] A standard can also be used, like in SEM, but without these requirements being met, quantitative data is unreliable.

EELS has been used to perform elemental mapping on individual nanocrystals to demonstrate that all elements are evenly distributed within a nanocrystals.[190] While this information can be useful, demonstrating the spatial presence of all elements in a nanocrystal does not suggest that the nanocrystals are of a single phase. EELS suffers from the same quantitation difficulties as EDS. It requires careful data analysis and elemental standards.[214] It can be useful for obtaining rough elemental ratios without great accuracy and spatial distribution of elements in nanocrystals can be estimated, but conclusions about phase purity should not be drawn from routine TEM analysis.

Optical Spectroscopy (UV-Vis): The final technique that almost all reports of CZTS nanocrystals include is optical spectroscopy, generally UV-Vis. This is used to estimate the band gap of the material. A trivial calculation using a Tauc plot can be done to determine if the material of interest has a direct or indirect band gap.[73] If $(\alpha h\nu)^2$ (α is the absorption coefficient and $h\nu$ is the photon energy) versus the photon energy ($h\nu$) gives a linear portion of the graph, then the band gap is direct and the linear portion indicates the onset of absorption. Extrapolating the linear portion of the graph back to the x-axis will give an estimate of the band gap. If the band gap is indirect, then $(\alpha h\nu)^{1/2}$ should give two separate portions of the graph that are linear and the average of those two lines extrapolated back to the x-axis will give the indirect band gap estimate. This is a very useful tool to indicate the onset of absorption, and thus the estimated band gap. CZTS has an estimated band gap of ~ 1.5 eV[122] and CZTSe is around 1.0 eV although reports on the CZTSe band gap vary, reporting band gaps from 1.0 eV to 1.5 eV.[188] Although UV-Vis is a quick, non-destructive method that utilizes simple instrumentation for estimating the

band gap of a material, it does not rule out higher band gap materials. There has been one report that the authors know of in which multiple band gaps were suggested in the CZTS system via UV-Vis analysis. Two different photon energy ranges were graphed to obtain two different linear portions of a direct band gap plot. Babu and coworkers investigated different Cu:Zn ratios in bulk CZTS films and discovered band gaps that were near that of Cu_2S for the copper-rich samples and near ZnS for the Zn-rich samples.[139] These band gaps were higher than that of CZTS, but their onset can be seen at different energy ranges than the onset of CZTS at ~ 1.4 eV. Although the band gap of CZTS is almost always reported via UV-Vis, further analysis at higher band gap energies is rarely done, so these impurity phases are not generally ruled out.

Another perhaps more important issue regarding the analysis of UV-Vis data for estimates of the band gap is the nature and quality of the samples that are being analyzed. As previously discussed, CZTS nanomaterials made by low temperature, solution routes tend to be very disordered materials. The defects present due to this disorder in addition to a sometimes broad particle size distribution can cause a gradual onset of absorption. This can make accurately estimating the band gap very difficult.

We performed UV-Vis on four samples: CZTS, CTS, ZnS and a mixture of all three samples together. Figure 5.2 shows all four samples plotted without band gap estimates. The ZnS sample (green) has a clear and direct onset of absorption at around 350 nm (~3.5 eV). However, the other three samples have very gradual onsets of absorption, which is expected for these more complex, disordered systems. While band gap estimates were attempted on these samples using the aforementioned calculation, it was unclear where the linear portion of the graph was, and thus where the band gap should be estimated. Also of interest for the current analysis is the fact that the ZnS absorption onset cannot be observed in this particular sample.

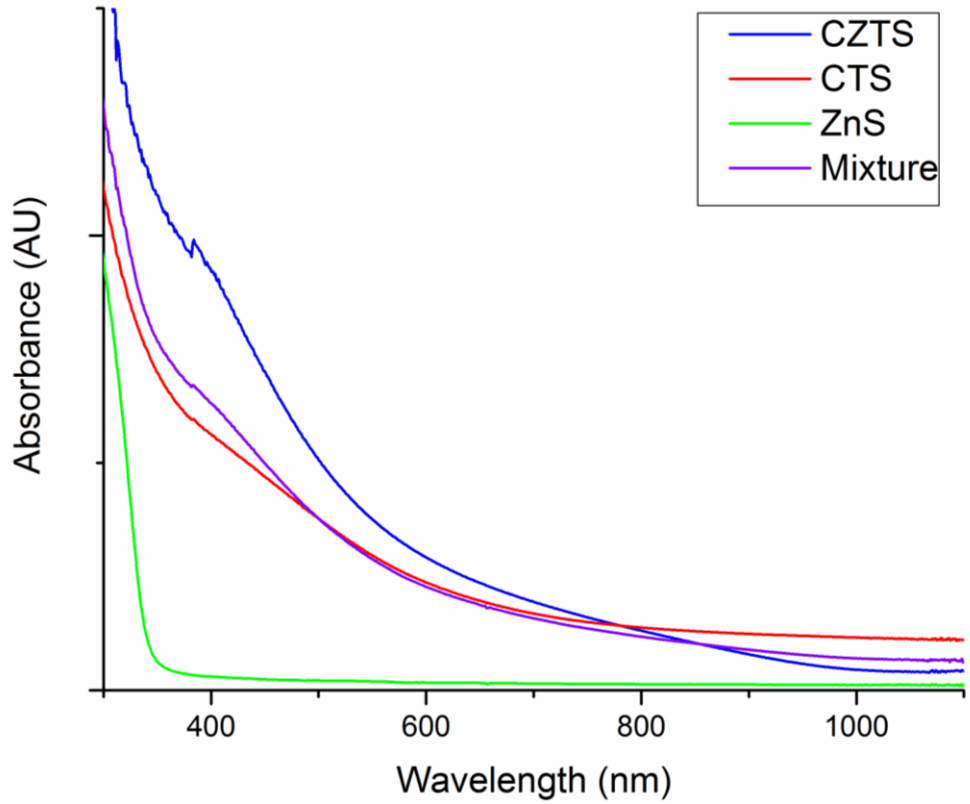

Figure 5.2: UV-Vis spectra for CZTS, CTS and ZnS, in addition to a mixture of all three samples.

While we encourage the use of absorption spectroscopy to confirm that the nanocrystals absorb radiation in the visible region, we do not believe it provides an accurate measure of the band gap of the material, nor does it assist in the ruling out of impurity phases.

Raman Spectroscopy: Another optical method that is occasionally used for characterizing CZTS nanocrystals is Raman scattering. Kesterite CZTS exhibits 15 Raman active modes.[215] Of these, the A symmetry modes (due to symmetric vibration of sulfur) are the strongest, and give rise to peaks at 287 cm^{-1} and 337 cm^{-1}.[216] Also present are weaker bands due to E and B symmetry modes (from transverse and longitudinal optical phonon interactions). Problems with Raman scattering analysis in assessing the purity of a CZTS sample come in attributing the cause of the peak found at 352 cm^{-1}. A CZTS vibrational mode has been reported at this frequency; but some binary and ternary sulfides share this peak. Both

CTS and ZnS display this same peak.[217,218] The peak at 352 cm^{-1} can point to the presence of Cu_3SnS_4, but it also has a vibrational mode at 317 cm^{-1} [217] that is not present in CZTS, and can therefore positively identify this species. Similarly, ZnS displays a wavenumber shift at 700 cm^{-1}.[219] Theoretically both impurities should be able to be identified by the presence of these other modes that do not exist for CZTS. However, despite the existence of these modes, the peaks exhibit a weak signal that can often be lost in the noise level. A method of addressing this is to utilize an ultraviolet excitation source. A 325 nm laser has demonstrated the ability to exercise resonant conditions for ZnS, but obtaining this data is not trivial.[220] While these publications have demonstrated the ability to use Raman scattering to detect impurity phases, it is not a practical solution without advanced Raman spectroscopy equipment and analysis.

X-Ray Photoelectron Spectroscopy: X-ray photoelectron spectroscopy is a useful tool for determining the oxidation state of each element in the CZTS system. It would be trivial, for example, to distinguish between a Cu^{+2} precursor and the appropriate Cu^{+1} oxidation state required for CZTS. If Cu^{+2} impurities exist in the sample, so called "shake up" peaks will be present in the spectrum.[221] Additionally, peaks can be shifted if they are in different bonding environments (e.g. the binding energy of the Zn^{+2} ions in CZTS will be shifted from those of ZnS due to slight differences in bonding environment).[176] However, this shift in binding energy is small and quite subtle. If impurities were present in the sample in small quantities, it would bevery difficult to distinguish between those different bonding environments. Typical literature reports utilizing high resolution XPS report the peak splitting values (if any quantitative data is reported at all). While there are characteristic peak splitting values for the metals, they are not necessarily sufficient to rule out impurities (as is demonstrated in Table

5.2). Therefore, although XPS can be useful for demonstrating that all the correct oxidation states are present, it does not directly aid in ruling out ZnS or CTS as impurity phases.

Binding Environment	Cu 2p	Zn 2p	Sn 3d
CZTS	19.75	23.05	8.45
CTS	19.83		8.44
ZnS		23.05	

Table 5.2 Peak splitting values for relevant metals in CZTS, CTS and ZnS samples. Values reported in eV.

High resolution XPS spectra were obtained for CZTS, CTS and ZnS phases and peak splitting values were calculated for the metals. The difference in the binding energy between the $p_{1/2}$ and $p_{3/2}$ peaks for Cu and Zn and the $d_{3/2}$ and $d_{5/2}$ peaks for Sn were calculated and are reported in Table 5.2. The peak splitting values are nearly identical for all three phases, indicating that distinguishing these phases, in practice, is not possible via XPS.

Thermal Analysis: Thermal analysis, in the form of either differential thermal analysis or differential scanning calorimetry, is a technique rarely utilized to determine nanocrystal purity, although some have included it in their analysis.[164,174,181] It can be useful if a sufficiently high temperature range is used because it detects any phase transitions that occur in a material. One can observe both melting and crystallization of substances using thermal methods. If more than one phase is present, (e.g. ZnS in addition to CZTS) two phase transitions for two different phases melting will be seen in the thermogram (in the case of DTA). The three important phases that we are concerned with are CZTS, ZnS and CTS. Their bulk melting temperatures are 990 °C,[222] 1700 °C[223] and 856 °C[224] respectively. However, they generally have transitions at lower temperatures due to the melting point depression effect seen in nanocrystals .[225] In the synthesis

of CZTS by Riha *et al*, the ZnS, CTS and CZTS melting temperatures were all observed below 1000 °C, demonstrating the feasibility for use in this quaternary system.

Although this technique should be able to determine if there is more than one phase present, it does have its drawbacks. It is a destructive technique so the sample used cannot be recovered. For nanocrystal syntheses, the thermograms also tend to be quite complicated in the lower temperature range due to the remaining capping ligands on the nanocrystals. Finally, a specific material cannot be identified solely by its phase transition. One can make standards to test versus an actual sample, but a melting point cannot necessarily be characterized as a specific phase. DTA can only determine *if* there are multiple phases present, not specifically *what* those phases are. Even with these drawbacks, it is the only routinely available method that the authors know of that can conclusively determine that the product of a synthesis has one or more phases. Used in conjunction with other techniques such as XRD and compositional analysis (via EDS or ICP), DTA can be a definitive technique for determining phase purity.

General Discussion/Conclusion:

The recent improvements in reported efficiencies in CZTS solar cells are exciting advances for the field of earth-abundant photovoltaics. These high efficiencies have encouraged a great deal of research on the materials and it has ultimately led to an overwhelming amount of literature on CZTS in general, but also on CZTS nanocrystals. This can be highly beneficial for the field, but also has its drawbacks. Many times, new papers are published without thorough analysis of the material. When these reports claim new and exciting advances, but no fundamental understanding of *why* the advance was made possible, it hinders future research from building upon these findings.

The field of nanocrystal research on CZTS is especially problematic in this respect. Many interesting publications are reported with minimal characterization on the material to support or explain the claims reported. With a complex quaternary (or quinary) system, it is imperative that thorough characterization is done in order to confirm that the synthesized material is, in fact, CZTS and that there are no impurity phases. And in some cases where impurity phases are present, it is helpful to understand how they affect the properties as a solar cell material.

Herein we have presented an overview of commonly used characterization techniques for analyzing CZTS nanocrystals. The advantages and drawbacks of each technique have been summarized with emphasis on the usefulness in determining phase purity. The authors hope that this report will be a guide for future research in the field, leading to more comprehensive studies on CZTS materials and ultimately improving the quality of published research.

Acknowledgements:

We would like to acknowledge the staff at the Colorado School of Mines electron microscopy facility for use of the instrumentation for SED/EDS analysis and specifically Gary Zito for instrumentation assistance.

REFERENCES

(1) NCADAC; US Government: 2014; Vol. 2014.

(2) Vincent, H.; Bertaut, E. F.; Baur, W. H.; Shannon, R. D. *Acta Crystallographica Section B-Structural Science* **1976**, *32*, 1749.

(3) Karl, T. R.; Melillo, J. T.; Peterson, T. C. *Global Climate Change Impacts in the United States*, 2009.

(4) MacKay, D. J. *Sustainable Energy - Without the Hot Air*; UIT Cambridge Ltd: Cambridge, 2009.

(5) Ginley, D.; Green, M. A.; Collins, R. *MRS Bull.* **2008**, *33*, 355.

(6) Administration, U. S. E. I.; U.S. Energy Information Administration: 2012; Vol. 2013.

(7) Administration, U. S. E. I.; U.S. Energy Information Administration 2014; Vol. 2014.

(8) Powell, D. M.; Winkler, M. T.; Goodrich, A.; Buonassisi, T. *Ieee Journal of Photovoltaics* **2013**, *3*, 662.

(9) Goetzberger, A.; Hebling, C.; Schock, H. W. *Materials Science & Engineering R-Reports* **2003**, *40*, 1.

(10) Tao, M. *Interface* **2008**, *17*, 30

(11) Chopra, K. L.; Paulson, P. D.; Dutta, V. *Progress in Photovoltaics: Research and Applications* **2004**, *12*, 69.

(12) Vasekar, P. S.; Dhakal, T. P.; InTech: 2013, p 145.

(13) Wadia, C.; Alivisatos, A. P.; Kammen, D. M. *Environ Sci Technol* **2009**, *43*, 2072.

(14) Yu, L. P.; Lany, S.; Kykyneshi, R.; Jieratum, V.; Ravichandran, R.; Pelatt, B.; Altschul, E.; Platt, H. A. S.; Wager, J. F.; Keszler, D. A.; Zunger, A. *Advanced Energy Materials* **2011**, *1*, 748.

(15) Foster, D. H.; Jieratum, V.; Kykyneshi, R.; Keszler, D. A.; Schneider, G. *Appl. Phys. Lett.* **2011**, *99*, 181903/1.

(16) Zakutayev, A.; McIntyre, D. H.; Schneider, G.; Kykyneshi, R.; Keszler, D. A.; Park, C. H.; Tate, J. *Thin Solid Films* **2010**, *518*, 5494.

(17) Hibberd, C. J.; Chassaing, E.; Liu, W.; Mitzi, D. B.; Lincot, D.; Tiwari, A. N. *Progress in Photovoltaics: Research and Applications* **2010**, *18*, 434.

(18) Ramasamy, K.; Malik, M. A.; Revaprasadu, N.; O'Brien, P. *Chem. Mater.* **2013**, *25*, 3551.

(19) Habas, S. E.; Platt, H. A. S.; van Hest, M. F. A. M.; Ginley, D. S. *Chemical Reviews* **2010**, *110*, 6571.

(20) Hillhouse, H. W.; Beard, M. C. *Curr. Opin. Colloid Interface Sci.* **2009**, *14*, 245.

(21) Cushing, B. L.; Kolesnichenko, V. L.; O'Connor, C. J. *Chem. Rev. (Washington, DC, U. S.)* **2004**, *104*, 3893.

(22) Baghbanzadeh, M.; Carbone, L.; Cozzoli, P. D.; Kappe, C. O. *Angew. Chem., Int. Ed.* **2011**, *50*, 11312.

(23) Yin, Y.; Alivisatos, A. P. *Nature* **2005**, *437*, 664.

(24) Stuczynski, S. M.; Brennan, J. G.; Steigerwald, M. L. *Inorganic Chemistry* **1989**, *28*, 4431.

(25) Thomson, J. W.; Nagashima, K.; Macdonald, P. M.; Ozin, G. A. *Journal of the American Chemical Society* **2011**, *133*, 5036.

(26) Burda, C.; Chen, X.; Narayanan, R.; El-Sayed, M. A. *Chem. Rev. (Washington, DC, U. S.)* **2005**, *105*, 1025.

(27) Jun, Y. W.; Casula, M. F.; Sim, J. H.; Kim, S. Y.; Cheon, J.; Alivisatos, A. P. *Journal of the American Chemical Society* **2003**, *125*, 15981.

(28) Mourdikoudis, S.; Liz-Marzán, L. M. *Chemistry of Materials* **2013**.

(29) Lunt, R. R.; Osedach, T. P.; Brown, P. R.; Rowehl, J. A.; Bulovic, V. *Adv. Mater. (Weinheim, Ger.)* **2011**, *23*, 5712.

(30) Panthani, M. G.; Korgel, B. A. *Annu. Rev. Chem. Biomol. Eng.* **2012**, *3*, 287.

(31) Ip, A. H.; Thon, S. M.; Hoogland, S.; Voznyy, O.; Zhitomirsky, D.; Debnath, R.; Levina, L.; Rollny, L. R.; Carey, G. H.; Fischer, A.; Kemp, K. W.; Kramer, I. J.; Ning, Z.; Labelle, A. J.; Chou, K. W.; Amassian, A.; Sargent, E. H. *Nat. Nanotechnol.* **2012**, *7*, 577.

(32) Fischer, A.; Rollny, L.; Pan, J.; Carey, G. H.; Thon, S. M.; Hoogland, S.; Voznyy, O.; Zhitomirsky, D.; Kim, J. Y.; Bakr, O. M.; Sargent, E. H. *Advanced Materials* **2013**, *25*, 5742.

(33) Fafarman, A. T.; Koh, W. K.; Diroll, B. T.; Kim, D. K.; Ko, D. K.; Oh, S. J.; Ye, X. C.; Doan-Nguyen, V.; Crump, M. R.; Reifsnyder, D. C.; Murray, C. B.; Kagan, C. R. *J. Am. Chem. Soc.* **2011**, *133*, 15753.

(34) Nag, A.; Kovalenko, M. V.; Lee, J. S.; Liu, W. Y.; Spokoyny, B.; Talapin, D. V. *Journal of the American Chemical Society* **2011**, *133*, 10612.

(35) Kovalenko, M. V.; Scheele, M.; Talapin, D. V. *Science (Washington, DC, U. S.)* **2009**, *324*, 1417.

(36) Buckley, J. J.; Couderc, E.; Greaney, M. J.; Munteanu, J.; Riche, C. T.; Bradforth, S. E.; Brutchey, R. L. *ACS Nano* **2014**, *8*, 2512.

(37) Zhitomirsky, D.; Voznyy, O.; Levina, L.; Hoogland, S.; Kemp, K. W.; Ip, A. H.; Sargent, E. H.; Thon, S. M. *Nat Commun* **2014**, *5*, 3803.

(38) NREL 2013; Vol. 2013.

(39) Dasbach, R.; Willeke, G.; Blenk, O. *Mrs Bull* **1993**, *18*, 56.

(40) Ennaoui, A.; Fiechter, S.; Pettenkofer, C.; Alonsovante, N.; Buker, K.; Bronold, M.; Hopfner, C.; Tributsch, H. *Sol Energ Mat Sol C* **1993**, *29*, 289.

(41) Ellmer, K.; Höpfner, C. *Philosophical Magazine A* **1997**, *75*, 1129.

(42) Fiechter, S.; Birkholz, M.; Hartmann, A.; Dulski, P.; Giersig, M.; Tributsch, H.; Tilley, R. J. D. *J Mater Res* **1992**, *7*, 1829.

(43) U.S. Geological SUrvey; Vol. 2013.

(44) Ennaoui, A.; Fiechter, S.; Jaegermann, W.; Tributsch, H. *Journal of the Electrochemical Society* **1986**, *133*, 97.

(45) Ennaoui, A.; Tributsch, H. *Sol Cells* **1984**, *13*, 197.

(46) Rezig, B.; Dahman, H.; Kenzari, M. *Renewable Energy* **1992**, *2*, 125.

(47) Smestad, G.; Ennaoui, A.; Fiechter, S.; Tributsch, H.; Hofmann, W. K.; Birkholz, M.; Kautek, W. *Sol Energ Mater* **1990**, *20*, 149.

(48) Berry, N.; Cheng, M.; Perkins, C. L.; Limpinsel, M.; Hemminger, J. C.; Law, M. *Advanced Energy Materials* **2012**, *2*, 1124.

(49) Bi, Y.; Yuan, Y. B.; Exstrom, C. L.; Darveau, S. A.; Huang, J. S. *Nano Lett* **2011**, *11*, 4953.

(50) Puthussery, J.; Seefeld, S.; Berry, N.; Gibbs, M.; Law, M. *J Am Chem Soc* **2011**, *133*, 716.

(51) Zhang, X.; Manno, M.; Baruth, A.; Johnson, M.; Aydil, E. S.; Leighton, C. *ACS Nano* **2013**, *7*, 2781.

(52) Wadia, C.; Wu, Y.; Gul, S.; Volkman, S. K.; Guo, J. H.; Alivisatos, A. P. *Chem Mater* **2009**, *21*, 2568.

(53) Kirkeminde, A.; Scott, R.; Ren, S. *Nanoscale* **2012**, *4*, 7649.

(54) Ferrer, I. J.; Nevskaia, D. M.; Delasheras, C.; Sanchez, C. *Solid State Communications* **1990**, *74*, 913.

(55) Ennaoui, A.; Fiechter, S.; Tributsch, H.; Giersig, M.; Vogel, R.; Weller, H. *Journal of the Electrochemical Society* **1992**, *139*, 2514.

(56) Bronold, M.; Pettenkofer, C.; Jaegermann, W. *Journal of Applied Physics* **1994**, *76*, 5800.

(57) Nesbitt, H. W.; Muir, I. J. *Geochimica et Cosmochimica Acta* **1994**, *58*, 4667.

(58) Andersson, K.; Nyberg, M.; Ogasawara, H.; Nordlund, D.; Kendelewicz, T.; Doyle, C. S.; Brown, G. E.; Pettersson, L. G. M.; Nilsson, A. *Physical Review B* **2004**, *70*.

(59) Buckley, A. N.; Woods, R. *Applied Surface Science* **1987**, *27*, 437.

(60) Eggleston, C. M.; Ehrhardt, J. J.; Stumm, W. *Am. Miner.* **1996**, *81*, 1036.

(61) Murphy, R.; Strongin, D. R. *Surf Sci Rep* **2009**, *64*, 1.

(62) Bronold, M.; Tomm, Y.; Jaegermann, W. *Surface Science* **1994**, *314*, L931.

(63) Dong, Y. Z.; Zheng, Y.; Duan, H.; Sun, Y.; Chen, Y. *Mater Lett* **2005**, *59*, 2398.

(64) Xuefeng, Q.; Yi, X.; Yitai, Q. *Mater Lett* **2001**, *48*, 109.

(65) Lin, Y. Y.; Wang, D. Y.; Yen, H. C.; Chen, H. L.; Chen, C. C.; Chen, C. M.; Tang, C. Y.; Chen, C. W. *Nanotechnology* **2009**, *20*.

(66) Wu, Y.; Wadia, C. N.; (University of California, USA). Application: WO WO, 2010, p 23pp.

(67) Wan, D. Y.; Wang, Y. T.; Zhou, Z. P.; Yang, G. Q.; Wang, B. Y.; Wei, L. *Mat Sci Eng B-Solid* **2005**, *122*, 156.

(68) Webber, T. E.; Neville, C. R.; Slaymaker, L. E.; Olejnicek, J.; Darveau, S. A.; Exstrom, C. L.; Soukup, R. J.; Ianno, N. J.; Amitabha, S.; Kamler, C. A. *Abstracts, 45th Midwest Regional Meeting of the American Chemical Society, Wichita, KS, United States, October 27-30* **2010**, MWRM.

(69) Rath, T.; Haas, W.; Pein, A.; Saf, R.; Maier, E.; Kunert, B.; Hofer, F.; Resel, R.; Trimmel, G. *Solar Energy Materials and Solar Cells* **2012**, *101*, 87.

(70) Ford, G. M.; Guo, Q. J.; Agrawal, R.; Hillhouse, H. W. *Thin Solid Films* **2011**, *520*, 523.

(71) Ruberu, T. P. A.; Albright, H. R.; Callis, B.; Ward, B.; Cisneros, J.; Fan, H.-J.; Vela, J. *ACS Nano* **2012**, *6*, 5348.

(72) Smith, D. K.; Luther, J. M.; Semonin, O. E.; Nozik, A. J.; Beard, M. C. *ACS Nano* **2010**, *5*, 183.

(73) Tauc, J. *Materials Research Bulletin* **1968**, *3*, 37.

(74) Kirkeminde, A.; Ren, S. *J. Mater. Chem. A* **2013**, *1*, 49.

(75) Lucas, J. M.; Tuan, C. C.; Lounis, S. D.; Britt, D. K.; Qiao, R. M.; Yang, W.; Lanzara, A.; Alivisatos, A. P. *Chem Mater* **2013**, *25*, 1615.

(76) Bai, Y.; Yeom, J.; Yang, M.; Cha, S.-H.; Sun, K.; Kotov, N. A. *J. Phys. Chem. C* **2013**, *117*, 2567.

(77) Li, W.; Doeblinger, M.; Vaneski, A.; Rogach, A. L.; Jaeckel, F.; Feldmann, J. *J. Mater. Chem.* **2011**, *21*, 17946.

(78) MacPherson, H. A.; Stoldt, C. R. *ACS Nano* **2012**, *6*, 8940.

(79) Gong, M.; Kirkeminde, A.; Ren, S. *Sci Rep* **2013**, *3*, 2092.

(80) Steinhagen, C.; Harvey, T. B.; Stolle, C. J.; Harris, J.; Korgel, B. A. *J Phys Chem Lett* **2012**, *3*, 2352.

(81) Brion, D. *Applications of Surface Science* **1980**, *5*, 133.

(82) Panzner, G.; Egert, B. *Surface Science* **1984**, *144*, 651.

(83) Biesinger, M. C.; Payne, B. P.; Grosvenor, A. P.; Lau, L. W. M.; Gerson, A. R.; Smart, R. S. C. *Applied Surface Science* **2011**, *257*, 2717.

(84) Mullet, M.; Boursiquot, S.; Abdelmoula, M.; Genin, J. M.; Ehrhardt, J. J. *Geochimica Et Cosmochimica Acta* **2002**, *66*, 829.

(85) Hawn, D. D.; DeKoven, B. M. *Surface and Interface Analysis* **1987**, *10*, 63.

(86) Birkholz, M.; Fiechter, S.; Hartmann, A.; Tributsch, H. *Physical Review B* **1991**, *43*, 11926.

(87) Seefeld, S.; Limpinsel, M.; Liu, Y.; Farhi, N.; Weber, A.; Zhang, Y.; Berry, N.; Kwon, Y. J.; Perkins, C. L.; Hemminger, J. C.; Wu, R.; Law, M. *J Am Chem Soc* **2013**, *135*, 4412.

(88) Ouertani, B.; Ouerfelli, J.; Saadoun, M.; Bessais, B.; Ezzaouia, H.; Bernede, J. C. *Mater. Charact.* **2005**, *54*, 431.

(89) Limpinsel, M.; Farhi, N.; Berry, N.; Lindemuth, J.; Perkins, C. L.; Lin, Q.; Law, M. *Energy & Environmental Science* **2014**.

(90) Ge, H.; Hai, L.; Prabhakar, R. R.; Ming, L. Y.; Sritharan, T. *RSC Adv.* **2014**, *4*, 16489.

(91) Zhu, L.; Richardson, B. J.; Yu, Q. *Nanoscale* **2014**, *6*, 1029.

(92) Wills, A. W.; Kang, M. S.; Khare, A.; Gladfelter, W. L.; Norris, D. J. *ACS Nano* **2010**, *4*, 4523.

(93) Yoffe, A. D. *Adv. Phys.* **2001**, *50*, 1.

(94) Puthussery, J.; Seefeld, S.; Berry, N.; Gibbs, M.; Law, M. *J. Am. Chem. Soc.* **2011**, *133*, 716.

(95) Riha, S. C.; Fredrick, S. J.; Sambur, J. B.; Liu, Y. J.; Prieto, A. L.; Parkinson, B. A. *Acs Applied Materials & Interfaces* **2011**, *3*, 58.

(96) Luther, J. M.; Law, M.; Song, Q.; Perkins, C. L.; Beard, M. C.; Nozik, A. J. *ACS Nano* **2008**, *2*, 271.

(97) Panzner, G.; Egert, B. *Surf. Sci.* **1984**, *144*, 651.

(98) Brion, D. *Appl. Surf. Sci.* **1980**, *5*, 133.

(99) Caban-Acevedo, M.; Liang, D.; Chew, K. S.; DeGrave, J. P.; Kaiser, N. S.; Jin, S. *ACS Nano* **2013**, *7*, 1731.

(100) Zhang, X.; Manno, M.; Baruth, A.; Johnson, M.; Aydil, E. S.; Leighton, C. *ACS Nano* **2013**, *7*, 2781.

(101) Yu, L.; Lany, S.; Kykyneshi, R.; Jieratum, V.; Ravichandran, R.; Pelatt, B.; Altschul, E.; Platt, H. A. S.; Wager, J. F.; Keszler, D. A.; Zunger, A. *Adv. Energy Mater.* **2011**, *1*, 748.

(102) Puthussery, J.; Seefeld, S.; Berry, N.; Gibbs, M.; Law, M. *Journal of the American Chemical Society* **2010**, *133*, 716.

(103) Seefeld, S.; Limpinsel, M.; Liu, Y.; Farhi, N.; Weber, A.; Zhang, Y.; Berry, N.; Kwon, Y. J.; Perkins, C. L.; Hemminger, J. C.; Wu, R.; Law, M. *J. Am. Chem. Soc.* **2013**, *135*, 4412.

(104) Bai, Y.; Yeom, J.; Yang, M.; Cha, S.-H.; Sun, K.; Kotov, N. A. *J. Phys. Chem. C* **2013**, *117*, 2567.

(105) Gong, M.; Kirkeminde, A.; Ren, S. *Sci Rep* **2013**, *3*, 2092.

(106) MacPherson, H. A.; Stoldt, C. R. *ACS Nano* **2012**, *6*, 8940.

(107) Kirkeminde, A.; Ruzicka, B. A.; Wang, R.; Puna, S.; Zhao, H.; Ren, S. *ACS Appl. Mater. Interfaces* **2012**, *4*, 1174.

(108) Ip, A. H.; Thon, S. M.; Hoogland, S.; Voznyy, O.; Zhitomirsky, D.; Debnath, R.; Levina, L.; Rollny, L. R.; Carey, G. H.; Fischer, A.; Kemp, K. W.; Kramer, I. J.; Ning, Z.; Labelle, A. J.; Chou, K. W.; Amassian, A.; Sargent, E. H. *Nature nanotechnology* **2012**, *7*, 577.

(109) Junod, A.; Wang, K. Q.; Triscone, G.; Lamarche, G. *Journal of Magnetism and Magnetic Materials* **1995**, *146*, 21.

(110) Ohgushi, K.; Ueda, Y. *Physical Review Letters* **2005**, *95*.

(111) Mourdikoudis, S.; Liz-Marzán, L. M. *Chemistry of Materials* **2013**, *25*, 1465.

(112) Antunez, P. D.; Buckley, J. J.; Brutchey, R. L. *Nanoscale* **2011**, *3*, 2399.

(113) Vaughn, D. D.; Patel, R. J.; Hickner, M. A.; Schaak, R. E. *Journal of the American Chemical Society* **2010**, *132*, 15170.

(114) Biesinger, M. C.; Payne, B. P.; Grosvenor, A. P.; Lau, L. W. M.; Gerson, A. R.; Smart, R. S. C. *Appl. Surf. Sci.* **2011**, *257*, 2717.

(115) Mullet, M.; Boursiquot, S.; Abdelmoula, M.; Genin, J.-M.; Ehrhardt, J.-J. *Geochim. Cosmochim. Acta* **2002**, *66*, 829.

(116) Nesbitt, H. W.; Scaini, M.; Hochst, H.; Bancroft, G. M.; Schaufuss, A. G.; Szargan, R. *Am. Mineral.* **2000**, *85*, 850.

(117) Hollinger, G.; Kumurdjian, P.; Mackowski, J. M.; Pertosa, P.; Porte, L.; Duc, T. M. *Journal of Electron Spectroscopy and Related Phenomena* **1974**, *5*, 237.

(118) Pratt, A. R.; Muir, I. J.; Nesbitt, H. W. *Geochim. Cosmochim. Acta* **1994**, *58*, 827.

(119) Kovalenko, M. V.; Scheele, M.; Talapin, D. V. *Science* **2009**, *324*, 1417.

(120) Fafarman, A. T.; Koh, W.-k.; Diroll, B. T.; Kim, D. K.; Ko, D.-K.; Oh, S. J.; Ye, X.; Doan-Nguyen, V.; Crump, M. R.; Reifsnyder, D. C.; Murray, C. B.; Kagan, C. R. *Journal of the American Chemical Society* **2011**, *133*, 15753.

(121) Administration, U. S. E. I.; U.S. Energy Information Administration: http://www.eia.gov/totalenergy/data/annual/perspectives.cfm, 2012; Vol. 2013.

(122) Scragg, J. J.; Dale, P. J.; Peter, L. M.; Zoppi, G.; Forbes, I. *physica status solidi (b)* **2008**, *245*, 1772.

(123) Fthenakis, V. M.; Moskowitz, P. D. *Prog. Photovoltaics* **1995**, *3*, 295.

(124) Chen, S.; Walsh, A.; Yang, J.-H.; Gong, X. G.; Sun, L.; Yang, P.-X.; Chu, J.-H.; Wei, S.-H. *Physical Review B* **2011**, *83*, 125201.

(125) Jimbo, K.; Kimura, R.; Kamimura, T.; Yamada, S.; Maw, W. S.; Araki, H.; Oishi, K.; Katagiri, H. *Thin Solid Films* **2007**, *515*, 5997.

(126) Katagiri, H. *Thin Solid Films* **2005**, *480–481*, 426.

(127) Todorov, T. K.; Tang, J.; Bag, S.; Gunawan, O.; Gokmen, T.; Zhu, Y.; Mitzi, D. B. *Advanced Energy Materials* **2013**, *3*, 34.

(128) Steinhagen, C.; Panthani, M. G.; Akhavan, V.; Goodfellow, B.; Koo, B.; Korgel, B. A. *Journal of the American Chemical Society* **2009**, *131*, 12554.

(129) Guo, Q.; Hillhouse, H. W.; Agrawal, R. *Journal of the American Chemical Society* **2009**, *131*, 11672.

(130) Chen, S.; Wang, L.-W.; Walsh, A.; Gong, X. G.; Wei, S.-H. *Appl. Phys. Lett.* **2012**, *101*, 223901/1.

(131) Chen, S.; Yang, J.-H.; Gong, X. G.; Walsh, A.; Wei, S.-H. *Physical Review B* **2010**, *81*, 245204.

(132) Chen, S.; Walsh, A.; Gong, X.-G.; Wei, S.-H. *Adv. Mater. (Weinheim, Ger.)* **2013**, *25*, 1522.

(133) Chen, S.; Gong, X. G.; Walsh, A.; Wei, S.-H. *Appl. Phys. Lett.* **2010**, *96*, 021902/1.

(134) Biswas, K.; Lany, S.; Zunger, A. *Appl. Phys. Lett.* **2010**, *96*, 201902/1.

(135) Tsega, M.; Kuo, D.-H. *Solid State Communications* **2013**, *164*, 42.

(136) Han, D.; Sun, Y. Y.; Bang, J.; Zhang, Y. Y.; Sun, H.-B.; Li, X.-B.; Zhang, S. B. *Physical Review B* **2013**, *87*, 155206.

(137) Maeda, T.; Nakamura, S.; Wada, T. *Japanese Journal of Applied Physics* **2011**, *50*.

(138) Ruan, C.-H.; Huang, C.-C.; Lin, Y.-J.; He, G.-R.; Chang, H.-C.; Chen, Y.-H. *Thin Solid Films* **2014**, *550*, 525.

(139) Suresh Babu, G.; Kishore Kumar, Y. B.; Uday Bhaskar, P.; Raja Vanjari, S. *Solar Energy Materials and Solar Cells* **2010**, *94*, 221.

(140) Mitzi, D. B.; Gunawan, O.; Todorov, T. K.; Wang, K.; Guha, S. *Solar Energy Materials and Solar Cells* **2011**, *95*, 1421.

(141) Todorov, T. K.; Reuter, K. B.; Mitzi, D. B. *Advanced Materials* **2010**, *22*, E156.

(142) Wang, W.; Winkler, M. T.; Gunawan, O.; Gokmen, T.; Todorov, T. K.; Zhu, Y.; Mitzi, D. B. *Adv. Energy Mater.* **2014**, *4*, 1301465/1.

(143) Kuo, D.-H.; Tsega, M. *Materials Research Bulletin* **2014**, *49*, 608.

(144) Schorr, S. *Solar Energy Materials and Solar Cells* **2011**, *95*, 1482.

(145) Schorr, S.; Mainz, R.; Moenig, H.; Lauermann, I.; Baer, M. *Prog. Photovoltaics* **2012**, *20*, 557.

(146) Schorr, S.; Hoebler, H.-J.; Tovar, M. *Eur. J. Mineral.* **2007**, *19*, 65.

(147) Johnson, M.; Baryshev, S. V.; Thimsen, E.; Manno, M.; Zhang, X.; Veryovkin, I. V.; Leighton, C.; Aydil, E. S. *Energy Environ. Sci.* **2014**, *7*, 1931.

(148) Nagaoka, A.; Miyake, H.; Taniyama, T.; Kakimoto, K.; Nose, Y.; Scarpulla, M. A.; Yoshino, K. *Appl. Phys. Lett.* **2014**, *104*, 152101/1.

(149) Sutter-Fella, C. M.; Stückelberger, J. A.; Hagendorfer, H.; La Mattina, F.; Kranz, L.; Nishiwaki, S.; Uhl, A. R.; Romanyuk, Y. E.; Tiwari, A. N. *Chemistry of Materials* **2014**.

(150) Zhou, H.; Song, T.-B.; Hsu, W.-C.; Luo, S.; Ye, S.; Duan, H.-S.; Hsu, C.-J.; Yang, W.; Yang, Y. *Journal of the American Chemical Society* **2013**, *135*, 15998.

(151) Wang, C.; Chen, S.; Yang, J.-H.; Lang, L.; Xiang, H.-J.; Gong, X.-G.; Walsh, A.; Wei, S.-H. *Chem. Mater.* **2014**, *26*, 3411.

(152) Olekseyuk, I. D.; Dudchak, I. V.; Piskach, L. V. *J. Alloy. Compd.* **2004**, *368*, 135.

(153) Colombara, D.; Robert, E. V. C.; Crossay, A.; Taylor, A.; Guennou, M.; Arasimowicz, M.; Malaquias, J. C. B.; Djemour, R.; Dale, P. J. *Sol. Energy Mater. Sol. Cells* **2014**, Ahead of Print.

(154) Redinger, A.; Hones, K.; Fontane, X.; Izquierdo-Roca, V.; Saucedo, E.; Valle, N.; Perez-Rodriguez, A.; Siebentritt, S. *Applied Physics Letters* **2011**, *98*.

(155) Schwarz, T.; Cojocaru-Miredin, O.; Choi, P.; Mousel, M.; Redinger, A.; Siebentritt, S.; Raabe, D. *Applied Physics Letters* **2013**, *102*, 042101.

(156) Mendis, B. G.; Goodman, M. C. J.; Major, J. D.; Taylor, A. A.; Durose, K.; Halliday, D. P. *Journal of Applied Physics* **2012**, *112*, 124508.

(157) Guan, Z.; Luo, W.; Zou, Z. *Crystengcomm* **2014**, *16*, 2929.

(158) Just, J.; Luetzenkirchen-Hecht, D.; Frahm, R.; Schorr, S.; Unold, T. *Appl. Phys. Lett.* **2011**, *99*, 262105/1.

(159) Zhitomirsky, D.; Voznyy, O.; Levina, L.; Hoogland, S.; Kemp, K. W.; Ip, A. H.; Thon, S. M.; Sargent, E. H. *Nature communications* **2014**, *5*, 3803.

(160) Suryawanshi, M. P.; Agawane, G. L.; Bhosale, S. M.; Shin, S. W.; Patil, P. S.; Kim, J. H.; Moholkar, A. V. *Mater. Technol. (London, U. K.)* **2013**, *28*, 98.

(161) Delbos, S. *EPJ Photovoltaics* **2012**, *3*, 35004.

(162) Aldakov, D.; Lefrancois, A.; Reiss, P. *J. Mater. Chem. C* **2013**, *1*, 3756.

(163) Ramasamy, K.; Malik, M. A.; O'Brien, P. *Chem. Commun. (Cambridge, U. K.)* **2012**, *48*, 5703.

(164) Riha, S. C.; Parkinson, B. A.; Prieto, A. L. *Journal of the American Chemical Society* **2009**, *131*, 12054.

(165) Kar, M.; Agrawal, R.; Hillhouse, H. W. *Journal of the American Chemical Society* **2011**, *133*, 17239.

(166) Chiang, M. Y.; Chang, S. H.; Chen, C. Y.; Yuan, F. W.; Tuan, H. Y. *J. Phys. Chem. C* **2011**, *115*, 1592.

(167) Belman, N.; Israelachvili, J. N.; Li, Y. L.; Safinya, C. R.; Bernstein, J.; Golan, Y. *Nano Letters* **2009**, *9*, 2088.

(168) Ahmadi, M.; Pramana, S. S.; Xi, L.; Boothroyd, C.; Lam, Y. M.; Mhaisalkar, S. *The Journal of Physical Chemistry C* **2012**, *116*, 8202.

(169) Wang, Y. H. A.; Zhang, X. Y.; Bao, N. Z.; Lin, B. P.; Gupta, A. *Journal of the American Chemical Society* **2011**, *133*, 11072.

(170) Panthani, M. G.; Akhavan, V.; Goodfellow, B.; Schmidtke, J. P.; Dunn, L.; Dodabalapur, A.; Barbara, P. F.; Korgel, B. A. *Journal of the American Chemical Society* **2008**, *130*, 16770.

(171) Guo, Q.; Ford, G. M.; Yang, W.-C.; Walker, B. C.; Stach, E. A.; Hillhouse, H. W.; Agrawal, R. *Journal of the American Chemical Society* **2010**, *132*, 17384.

(172) Li, L.; Zhang, B. L.; Cao, M.; Sun, Y.; Jiang, J. C.; Hu, P. F.; Shen, Y.; Wang, L. J. *J. Alloys Compd.* **2013**, *551*, Ahead of Print.

(173) Chesman, A. S. R.; Duffy, N. W.; Peacock, S.; Waddington, L.; Webster, N. A. S.; Jasieniak, J. J. *RSC Advances* **2013**, *3*, 1017.

(174) Chesman, A. S. R.; van, E. J.; Duffy, N. W.; Webster, N. A. S.; Jasieniak, J. J. *Cryst. Growth Des.* **2013**, Ahead of Print.

(175) Li, J.; Shen, J.; Li, Z.; Li, X.; Sun, Z.; Hu, Z.; Huang, S. *Mater. Lett.* **2013**, *92*, 330.

(176) Edler, M.; Rath, T.; Schenk, A.; Fischereder, A.; Haas, W.; Edler, M.; Chernev, B.; Kunert, B.; Hofer, F.; Resel, R.; Trimmel, G. *Materials Chemistry and Physics* **2012**, *136*, 582.

(177) Zou, C.; Zhang, L.; Lin, D.; Yang, Y.; Li, Q.; Xu, X.; Chen, X. a.; Huang, S. *Crystengcomm* **2011**, *13*, 3310.

(178) Liu, W.; Guo, B.; Mak, C.; Li, A.; Wu, X.; Zhang, F. *Thin Solid Films* **2012**, Ahead of Print.

(179) Liu, W. C.; Guo, B. L.; Wu, X. S.; Zhang, F. M.; Mak, C. L.; Wong, K. H. *J. Mater. Chem. A* **2013**, *1*, 3182.

(180) Zhou, Y.-L.; Zhou, W.-H.; Li, M.; Du, Y.-F.; Wu, S.-X. *J. Phys. Chem. C* **2011**, *115*, 19632.

(181) Shin, S. W.; Han, J. H.; Park, C. Y.; Kim, S. R.; Park, Y. C.; Agawane, G. L.; Moholkar, A. V.; Yun, J. H.; Jeong, C. H.; Lee, J. Y.; Kim, J. H. *J. Alloy. Compd.* **2012**, *541*, 192.

(182) Shin, S. W.; Han, J. H.; Park, C. Y.; Moholkar, A. V.; Lee, J. Y.; Kim, J. H. *J. Alloys Compd.* **2012**, *516*, 96.

(183) Khare, A.; Wills, A. W.; Ammerman, L. M.; Norris, D. J.; Aydil, E. S. *Chem. Commun.* **2011**, *47*, 11721.

(184) Zhao, Y.; Zhou, W.-H.; Jiao, J.; Zhou, Z.-J.; Wu, S.-X. *Materials Letters* **2013**, *96*, 174.

(185) Li, Z. Q.; Shi, J. H.; Liu, Q. Q.; Chen, Y. W.; Sun, Z.; Yang, Z.; Huang, S. M. *Nanotechnology* **2011**, *22*, 265615/1.

(186) Shi, L.; Pei, C.; Xu, Y.; Li, Q. *J. Am. Chem. Soc.* **2011**, *133*, 10328.

(187) Su, Z.; Yan, C.; Tang, D.; Sun, K.; Han, Z.; Liu, F.; Lai, Y.; Li, J.; Liu, Y. *Crystengcomm* **2012**, *14*, 782.

(188) Ahn, S.; Jung, S.; Gwak, J.; Cho, A.; Shin, K.; Yoon, K.; Park, D.; Cheong, H.; Yun, J. H. *Applied Physics Letters* **2010**, *97*, 021905.

(189) Haas, W.; Rath, T.; Pein, A.; Rattenberger, J.; Trimmel, G.; Hofer, F. *Chem. Commun.* **2011**, *47*, 2050.

(190) Shavel, A.; Arbiol, J.; Cabot, A. *Journal of the American Chemical Society* **2010**, *132*, 4514.

(191) Wei, H.; Guo, W.; Sun, Y. J.; Yang, Z.; Zhang, Y. F. *Materials Letters* **2010**, *64*, 1424.

(192) Riha, S. C.; Parkinson, B. A.; Prieto, A. L. *Journal of the American Chemical Society* **2011**, *133*, 15272.

(193) Ou, K.-L.; Fan, J.-C.; Chen, J.-K.; Huang, C.-C.; Chen, L.-Y.; Ho, J.-H.; Chang, J.-Y. *Journal of Materials Chemistry* **2012**, *22*, 14667.

(194) Fan, F.-J.; Wu, L.; Gong, M.; Liu, G.; Wang, Y.-X.; Yu, S.-H.; Chen, S.; Wang, L.-W.; Gong, X.-G. *ACS Nano* **2013**.

(195) Fan, F.-J.; Wu, L.; Gong, M.; Chen, S. Y.; Liu, G. Y.; Yao, H.-B.; Liang, H.-W.; Wang, Y.-X.; Yu, S.-H. *Sci Rep* **2012**, *2*, 952.

(196) Kang, C.-C.; Chen, H.-F.; Yu, T.-C.; Lin, T.-C. *Materials Letters* **2013**, *96*, 24.

(197) Li, C.; Ha, E.; Wong, W.-L.; Li, C.; Ho, K.-P.; Wong, K.-Y. *Materials Research Bulletin* **2012**, *47*, 3201.

(198) Li, M.; Zhou, W.-H.; Guo, J.; Zhou, Y.-L.; Hou, Z.-L.; Jiao, J.; Zhou, Z.-J.; Du, Z.-L.; Wu, S.-X. *The Journal of Physical Chemistry C* **2012**.

(199) Liao, H.-C.; Jao, M.-H.; Shyue, J.-J.; Chen, Y.-F.; Su, W.-F. *J. Mater. Chem. A* **2013**, *1*, 337.

(200) Lu, X.; Zhuang, Z.; Peng, Q.; Li, Y. *Chem. Commun.* **2011**, *47*, 3141.

(201) Regulacio, M. D.; Ye, C.; Lim, S. H.; Bosman, M.; Ye, E.; Chen, S.; Xu, Q.-H.; Han, M.-Y. *Chem.--Eur. J.* **2012**, *18*, 3127.

(202) Singh, A.; Geaney, H.; Laffir, F.; Ryan, K. M. *J. Am. Chem. Soc.* **2012**, *134*, 2910.

(203) Cattley, C. A.; Cheng, C.; Fairclough, S. M.; Droessler, L. M.; Young, N. P.; Warner, J. H.; Smith, J. M.; Assender, H. E.; Watt, A. A. R. *Chem Commun (Camb)* **2013**.

(204) Cao, Y.; Denny, M. S.; Caspar, J. V.; Farneth, W. E.; Guo, Q.; Ionkin, A. S.; Johnson, L. K.; Lu, M.; Malajovich, I.; Radu, D.; Rosenfeld, H. D.; Choudhury, K. R.; Wu, W. *Journal of the American Chemical Society* **2012**, *134*, 15644.

(205) ICSD 2012.

(206) Lotfipour, M.; Machani, T.; Rossi, D. P.; Plass, K. E. *Chemistry of Materials* **2011**, *23*, 3032.

(207) Burton, L. A.; Walsh, A. *J. Phys. Chem. C* **2012**, *116*, 24262.

(208) Bilenkii, B. F.; Mikolaic.Ag; Freik, D. M. *Physica Status Solidi* **1968**, *28*, K5.

(209) Chattopadhyay, T.; Pannetier, J.; Vonschnering, H. G. *Journal of Physics and Chemistry of Solids* **1986**, *47*, 879.

(210) Greyson, E. C.; Barton, J. E.; Odom, T. W. *Small* **2006**, *2*, 368.

(211) Goldstein, J.; Newbury, D.; Joy, D.; Lyman, C.; Echlin, P.; Lifshin, E.; Sawyer, L.; Michael, J. *Scanning Electron Microscopy and X-Ray Microanalysis*; 3 ed.; Kluwer Academic / Plenum Publishers: New York, New York, 2003.

(212) Fairbrother, A.; Fontané, X.; Izquierdo-Roca, V.; Espíndola-Rodríguez, M.; López-Marino, S.; Placidi, M.; Calvo-Barrio, L.; Pérez-Rodríguez, A.; Saucedo, E. *Solar Energy Materials and Solar Cells* **2013**, *112*, 97.

(213) Egerton, R. F. *Physical principles of electron microscopy an introduction to TEM, SEM, and AEM*; Springer Science+Business Media: New York, 2005.

(214) Egerton, R. F. *Electron energy-loss spectroscopy in the electron microscope*; Springer: New York, 2011.

(215) Dumcenco, D.; Huang, Y. S. *Optical Materials* **2013**, *35*, 419.

(216) Fontane, X.; Izquierdo-Roca, V.; Saucedo, E.; Schorr, S.; Yukhymchuk, V. O.; Valakh, M. Y.; Perez-Rodriguez, A.; Morante, J. R. *J. Alloy. Compd.* **2012**, *539*, 190.

(217) Fernandes, P. A.; Salomé, P. M. P.; Cunha, A. F. d. *Journal of Physics D: Applied Physics* **2010**, *43*, 215403.

(218) Serrano, J.; Cantarero, A.; Cardona, M.; Garro, N.; Lauck, R.; Tallman, R. E.; Ritter, T. M.; Weinstein, B. A. *Physical Review B* **2004**, *69*, 014301.

(219) Yu, Y.-M.; Nam, S.; O, B.; Lee, K.-S.; Choi, Y. D.; Yoon, M.-Y.; Yu, P. Y. *Materials Chemistry and Physics* **2003**, *78*, 149.

(220) Fontane, X.; Calvo-Barrio, L.; Izquierdo-Roca, V.; Saucedo, E.; Perez-Rodriguez, A.; Morante, J. R.; Berg, D. M.; Dale, P. J.; Siebentritt, S. *Applied Physics Letters* **2011**, *98*.

(221) Biesinger, M. C.; Hart, B. R.; Polack, R.; Kobe, B. A.; Smart, R. S. C. *Minerals Engineering* **2007**, *20*, 152.

(222) Valdes, M.; Modibedi, M.; Mathe, M.; Hillie, T.; Vazquez, M. *Electrochimica Acta*.

(223) Su, Z.; Sun, K.; Han, Z.; Cui, H.; Liu, F.; Lai, Y.; Li, J.; Hao, X.; Liu, Y.; Green, M. A. *Journal of Materials Chemistry A* **2014**, *2*, 500.

(224) Zou, Y.; Su, X.; Jiang, J. *J. Am. Chem. Soc.* **2013**, *135*, 18377.

(225) Alivisatos, A. P. *J. Phys. Chem.* **1996**, *100*, 13226.